Charged particle multiplicity measurement in Au-Au collisions using the Pad Chambers of the PHENIX detector at RHIC.

Thesis for the degree of Ph.D. in Physics
presented to the Feinberg Graduate School
of the Weizmann Institute of Science,
Rehovot, Israel

by

Alexander Milov

Supervisor: Prof. Itzhak Tserruya

May 27, 2002.

Abstract

This thesis is devoted to the measurement of the charged particle pseudorapidity density $dN_{ch}/d\eta$ at midrapidity in Au-Au collisions at RHIC at 130 and 200 GeV using the Pad Chamber subsystem of the PHENIX detector.

The charged particle multiplicity is an important observable to characterize Relativistic Heavy Ion collisions. These collisions are used as an experimental tool for the search of the phase transition from ordinary matter to the Quark-Gluon Plasma (QGP), a new state of matter predicted by Quantum Chromodynamics lattice calculations. The charged particle multiplicity carries information about the geometry of the collision and the initial energy density in the system. It helps to understand the mechanisms of particle production and is a powerful tool to constrain theories.

The $dN_{ch}/d\eta$ in PHENIX was measured using the two layers of Pad Chamber (PC) detectors, which are part of the detector tracking system. The PCs are large (scale total area of 88m^2) multiwire proportional chambers with a newly developed type of cathode readout, and provide a good spatial resolution (less than 2 mm in the first layer, PC1). The PC1 design, construction and performance are described in this thesis.

The analysis procedure to determine the charged particle multiplicity using the Pad Chambers was developed and supported by extensive Monte Carlo simulations. At the full RHIC design energy of $\sqrt{s_{NN}}$ =200 GeV, the charged particle pseudorapidity density, for the 5% most central collisions is found to be $dN_{ch}/d\eta_{|\eta=0} = 709 \pm 41$. This is $\sim 110\%$ larger than the SPS results for Pb-Pb collisions at $\sqrt{s_{NN}} = 17.2$ GeV.

The value of $dN_{ch}/d\eta_{|\eta=0}$ per pair of participating nucleons analyzed shows a steady rise as a function of centrality. In the framework of a variety of models this rise implies a large contribution of hard processes to particle production.

The ratio of $\langle E_T \rangle / \langle N_{ch} \rangle$ remains constant at 0.8 GeV, as a function of centrality and as function of $\sqrt{s_{NN}}$ as also observed at the SPS at CERN and at the AGS at BNL.

Contents

List of Figures

List of Tables

Chapter 1

Introduction

1.1   Quark Gluon Plasma.

The quantum chromodynamics (QCD) theory is a component of the Standard Model. It describes the strong interactions of matter using the formalism of quarks and gluons. Quarks are fundamental particles characterized by their flavor, a new degree of freedom. Six different flavors of quarks are known to exist, however only the two lightest quarks ($m_q < 10$ MeV) called "up" and "down" are abundantly present in nuclei.

The coupling constant of the strong interactions α_s depends on the momentum transfer in the interaction. At high distances (low momentum transfer) the coupling constant is strong leading to the phenomenon of quark confinement. This phenomenon is well known in nature reflected in the fact that quarks can be observed only in bound states (confined) as constituents of composite particles called hadrons. The quarks inside hadrons possess dynamically generated masses in the range of hundreds MeV, therefore leading to the breaking of the chiral symmetry.

In contrast to that, at short distances (high momentum transfer), the coupling constant α_s decreases logarithmically leading to the effect of "asymptotic freedom" of quarks. For this regime a perturbative treatment of QCD (pQCD), based on an expansion in powers of the coupling constant, is a good approach.

Numerical calculations of QCD on the lattice predict a phase transition from ordinary matter to a new state called the quark-gluon plasma (QGP) under conditions of high temperature and/or density in the system. In the QGP state, in which the interactions among the quarks occur mainly at short distances where the coupling is weak, matter would not exhibit neither confinement nor chiral symmetry breaking. Recent calculations [1] set the critical temperature T_c of the phase transition to be around ~175 MeV at vanishing baryon density ρ, see fig. 1.1. At zero temperature the critical

density for the phase transition is expected to be in the range $5\rho_0 \quad < \quad \rho_c \quad < \quad 10\rho_0$, where ρ_o denotes the ground state density of nuclear matter (~ 0.15 GeV/fm^3). The two extreme cases of high-T and high-ρ phase transitions are connected to each other, forming a continuous phase boundary $T_c(\rho)$. For $T(\rho) < T_c(\rho)$ strongly interacting matter is effectively described in terms of hadronic degrees of freedom (baryons and mesons), whereas for $T(\rho) > T_c(\rho)$ the effective degrees of freedom are the quarks and gluons.
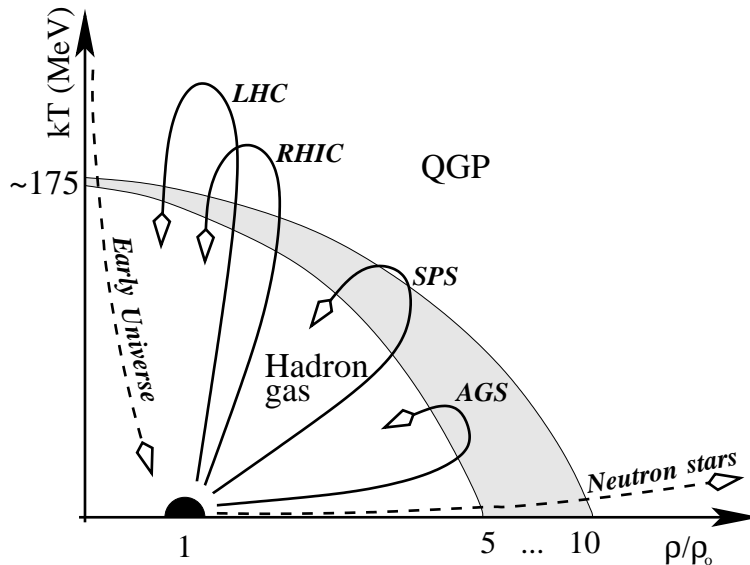
Figure 1.1: Phase diagram of the nuclear matter.

The order of the phase transitions is not firmly established. There are good reasons to expect, that the transition between the low-temperature and high-temperature QCD is of first order. The order of the phase transition is believed to be quite sensitive to the number of light, dynamical quark flavors. A second-order phase transition is predicted for two massless flavors and a first-order phase transition for three massless flavors. The phase transitions leading to deconfinement and to the restoration of chiral symmetry occur at similar conditions of temperature and density or may even coincide with each other.

The predicted phase transition from hadronic matter to the QGP can be studied in laboratory conditions. The existing tool for that study is the Relativistic Heavy Ion (RHI) collisions. The RHI programme started about 15 years ago at the AGS facility at BNL and at the SPS at CERN. Heavy ion beams accelerated to relativistic energies were directed onto fixed targets, with center of mass energy per nucleon of $\sqrt{s_{NN}} = 4$ GeV and 17 GeV at AGS and SPS, respectively. With the advent of the Relativistic Heavy Ion Collider (RHIC) at BNL in 2000 the first colliding RHI beams have become available for experimental studies, substantially increasing the energy deposited in the collisions. In year 2001 RHIC was operated at the full designed energy of $\sqrt{s_{NN}} = 200$ GeV. RHIC is

briefly discussed in sec. 1.3.

The most recent results of the AGS and SPS programmes and the current status of the research in the field of RHI collisions were reported at the last Quark Matter Conference that took place in January 2001 [2] and are reviewed in many other publications (e.g.: [3, 4, 5]).

1.2   Search for the QGP

Due to the complexity of RHI collisions, the very short lifetime of the QGP (a few fm/c) and the abundant hadron production after the QGP phase is dissolved, the study of the phase transition requires the investigation of as many signatures of the QGP as possible, using different observables produced in the collisions.

Obviously, a comprehensive review of the current QGP status and its signatures falls out of the scope of this thesis. In this section the discussion is focussed on Global observables which are closely related to the topic of this work, and Electromagnetic probes which are the main research interest of the Heavy Ion group at the Weizmann Institute.

Global observables

The global observables of RHI collisions, such as charged particle and transverse energy densities characterize the collision and in particular define the geometry or impact parameter of the collision (see Appendix A.1). They can be related to the initial energy density ε_{Bj} using the Bjorken formula [6] (see A.3) and carry information about the mechanisms of the particle production. Various models aiming at describing the physics of RHI collisions (e.g. those summarized in [7]) have to comply with the global observables measured in the experiment.

One of the basic requirements for the phase transition is that the energy density in the system ε must be sufficiently high. Different calculations established that the transition to the QGP phase may occur at $\varepsilon \sim 1$ GeV/fm^3. Already at the AGS, the energy density ε_{Bj} was measured [8] to be above 1 GeV/fm^3. At SPS energies ε_{Bj} was found to be close to 3 GeV/fm^3 [10, 11], thus suggesting that the system might have enough energy to pass the phase transition. It will be shown in this work (sec. 4.4) that at RHIC energies the Bjorken energy density ε_{Bj} is larger than 5 GeV/fm^3 [12] well above the energy required for the phase transition.

An important question is if the particle production in RHI collisions is different from a simple superposition of $p\bar{p}$ collisions. The centrality dependence of the charged particle pseudorapidity density $dN_{ch}/d\eta$ and of the transverse energy pseudorapidity density

$dE_T/d\eta$ divided by the number of participants N_p can provide an answer to it (see Appendix A.2 and A.3 for definitions). For low number of participants, the particle yield per participant is expected to be the same as in $p\bar{p}$ collisions. For the most central events (large number of participants) one expects new mechanisms to play a significant role. At the SPS energy of $\sqrt{s_{NN}}$ =17 GeV the centrality dependence of the $dN_{ch}/d\eta/(0.5 \times N_p)$ was found to be weak [10]. It will be shown in the thesis (sec. 4.2 and 4.3) that the situation is very different at RHIC energies.

Many models like [13, 14, 16] distinguish two components in the particle production, a "soft" component proportional to the number of participants N_p, and a "hard" component proportional to the number of binary collisions N_c between participants. Hard processes play an important role in RHI reactions because they occur in the initial stages of the collision and can be used to diagnostic the matter produced. In particular, J/Ψ suppression [17] and energy loss through gluon radiation of high partons (jet quenching) [18] are predicted as signatures of deconfined matter. Hard processes are characterized by a large momentum transfer and consequently pQCD calculations become applicable providing a reliable theoretical framework for comparison with experimental results. At the SPS energy the contribution of hard processes is rather small, reflected in the weak dependence of the $dN_{ch}/d\eta/(0.5N_p)$ on centrality. The contribution of hard processes to the particle production and comparison of model calculations to the measured data at RHIC energies is discussed in sec. 4.5.

Electromagnetic probes

Dileptons and photons produced in RHI collisions are unique probes of the QGP. The mean free path of leptons and photons is large compared to the size of the system because they are not affected by the strong force. Therefore they can leave the fireball practically without interactions. This unique property of the electromagnetic probes allows to study the processes taking place at the very earliest stage of the collision, when the QGP is believed to be formed.

Of particular interest are the low mass dileptons, which can provide evidence of the chiral symmetry restoration. The ρ-meson with a lifetime of 1.3 fm/c is a short-living particle compared to the lifetime of the fireball ($\sim$10 fm/c). The ρ-meson produced within the fireball would also decay inside it, where its properties (mass and/or width) can be different from its vacuum properties. The spectral shape of the ρ-meson invariant mass distribution can be measured through the dilepton channel ($\rho \rightarrow e^+e^-$) which has a branching ratio of 4.5×10^{-5}. A possible modification of the ρ-meson properties can be compared to the "reference" masses of ω- and ϕ-mesons, which have longer lifetime

(23 fm/c and 44 fm/c respectively) and, therefore decay mostly outside the fireball when the hottest and the densest phase of matter is already dissolved.

The CERES experiment at SPS is a dedicated experiment to study dielectron production in the low mass region $m_{ee} < 1.4$ GeV/c^2. During the last 10 years the CERES experiment has studied various systems from p-Be to Pb-Au at different energies available at SPS. The latest results of the CERES experiment can be found in [19, 20]. The CERES experiment has found that the dielectron yield in p-Be and p-Au collisions at 450 A GeV[1] is in a very good agreement with the expectations from the known decays of light vector mesons. However, a significant enhancement is observed in the heavy nuclei reactions of S-Au at 200 A GeV and Pb-Au at 158 A GeV and 40 A GeV of the projectile particles. The enhancement was measured to be as high as 2.9±0.9 at 158 A GeV and even 5.1±1.3 for 40 A GeV Pb-Au collisions.

In order to explain these results additional mechanisms of dielectron production have to be invoked. The excess is partially attributed to the $\pi^+\pi^-$ annihilation channel ($\pi^+\pi^- \to \rho \to e^+e^-$). However, this mechanism alone does not explain the measurements in the mass region $0.2 < m_{ee} < 0.6$ GeV/c^2.

A very successful attempt to reproduce the CERES results is based on the in-medium modification of the ρ-meson properties. The drop of the ρ-meson mass [21], due to the high baryon density in the medium as a step towards chiral symmetry restoration quantitatively reproduces the data. The same agreement was achieved by broadening the ρ-meson mass peak [22] due to rescattering of the ρ-meson from baryons in the hadron gas. More precise studies of dilelectron production in the low mass region may allow to discriminate between these two scenarios.

The extension of CERES measurements at SPS by the PHENIX experiment at RHIC should be very interesting. The first results on single electron production at RHIC have already been published [23] from the year 2000 physics run. The second physics run of PHENIX will provide the first measurements of the ϕ-meson using $\phi \to K^+K^-$ and $\phi \to e^+e^-$ channels. However, mass region below the ϕ-meson is difficult to access in the present PHENIX configuration due to a very high combinatorial background. An upgrade, which significantly increases the dielectron capabilities of the detector is currently considered by PHENIX [24].

---

[1]The energies denoted with "A GeV" refer to the projectile in the laboratory system.

1.3 Relativistic Heavy Ion Collider

The Relativistic Heavy Ion Collider at Brookhaven National Laboratory is a new dedicated machine to study RHI and polarized p-p collisions. RHIC is a very flexible machine capable of colliding various species from p-p to d-Au and to Au-Au over a very broad energy range from $\sqrt{s_{NN}}$ =19 GeV to $\sqrt{s_{NN}}$ =200 GeV. The main parameters of the RHIC are presented in Table 1.1 below.

Table 1.1: RHIC main parameters.

Parameter	Value	
Circumference (m)	3843	
Number of interaction regions	6	
Bunch spacing in one ring (ns)	213	
	Au-Au	**p-p**
Number of particles per bunch	10^9	10^{11}
Top energy $\sqrt{s_{NN}}$ (GeV)	200	500
Luminosity, average $(cm^{-2}s^{-1})$	2×10^{26}	1×10^{31}
Beam lifetime (h)	~ 10	> 10

The first physics run conducted in year 2000 provided a first look at the Au-Au collisions at $\sqrt{s_{NN}}$ =130 GeV. In spite of a very short and low luminosity run (total integrated luminosity $\sim$0.2 μb^{-1}) a large amount of new and interesting data were reported at the last Quark Matter Conference [2] from all RHIC experiments, BRAHMS[25], PHOBOS[26], PHENIX[27] and STAR[28] taking data simultaneously at four collision points of RHIC.

1.4 Goals of the PHENIX experiment.

PHENIX is one of the two "large" experiments running at RHIC. The experiment is mainly focussed on the measurement of electromagnetic observables (electrons pairs, muon pairs and photons) but also has enhanced hadron measurement capabilities. Its strategy is to measure as many potential signatures of the quark-gluon plasma as possible in order to determine if any or all of them simultaneously show some anomaly due to the phase transition.

Electron pairs can be measured at midrapidity over a very broad range of invariant masses from low masses ($m_{ee} \lesssim$ 1 GeV/c^2, where the vector mesons ρ, ω and ϕ are the dominant sources), up to J/Ψ mass. Thermal radiation, chiral symmetry restoration and J/Ψ suppression are the main topics of interest associated with these observables.

Special emphasis will be put on the measurement of the ϕ-meson as an indicator of chiral symmetry restoration and of strangeness enhancement. The ϕ-meson can be measured using both the electron and hadron decay channels.

The thermal radiation from the quark-gluon plasma is addressed in the PHENIX experiment using its photon and dilepton measurement capabilities.

At forward rapidities, the J/Ψ, $\Psi\prime$ and Υ can be measured in the PHENIX experiment by their dimuon decay channels.

In addition to that, the PHENIX experiment measures identified hadron spectra in the mid-rapidity region and a variety of other important physics issues, such as strangeness and charm production, jet quenching, and particle correlations.

To accomplish these tasks the PHENIX detector has superb mass resolution (0.5% for $\phi \rightarrow e^+e^-$) good particle identification and precise tracking. PHENIX is capable to measure high p_T hadrons, one of the new diagnostic tools opening up at RHIC energies. Since some of the potential signatures involve rare processes, the detector is designed to take data at the highest luminosities expected at RHIC.

1.5 The PHENIX detector.

Fig. 1.2 shows a three-dimensional cutaway view of the PHENIX detector, showing the location of the various detector subsystems. The detector consists of four spectrometers, two central arms with an axial field magnet, each one covering the pseudorapidity range $\Delta\eta = \pm 0.35$, and subtending $\Delta\phi = 90^o$ in azimuth and two forward arms covering the pseudorapidity intervals $\Delta\eta = \pm(1.15 - 2.35)$ with 2π azimuthal coverage. The detector subsystems are summarized in Table 1.2. The last column explains the function of each subsystem. A complete description of the detector PHENIX can be found in [27] and on the Web [29]. Only a short description is given here.

Close to the interaction vertex the set-up includes a Multiplicity Vertex Detector (MVD), which provides event characterization, centrality trigger and determines the collision vertex with high precision[2].

The central arms identify the type of particle and measure its momentum as well as separate electrons from pions. For that purpose each arm includes particle identification and tracking devices: drift chambers (DC), 3 sets of pad chambers (PC) at radii 2.5 m, 4.2 m and 5.0 m, Ring Imaging Cherenkov (RICH) detector, time expansion chamber (TEC), time of flight (TOF) detector and electromagnetic calorimeter (EMCal).

---

[2]The MVD was not installed in the year-1 run.
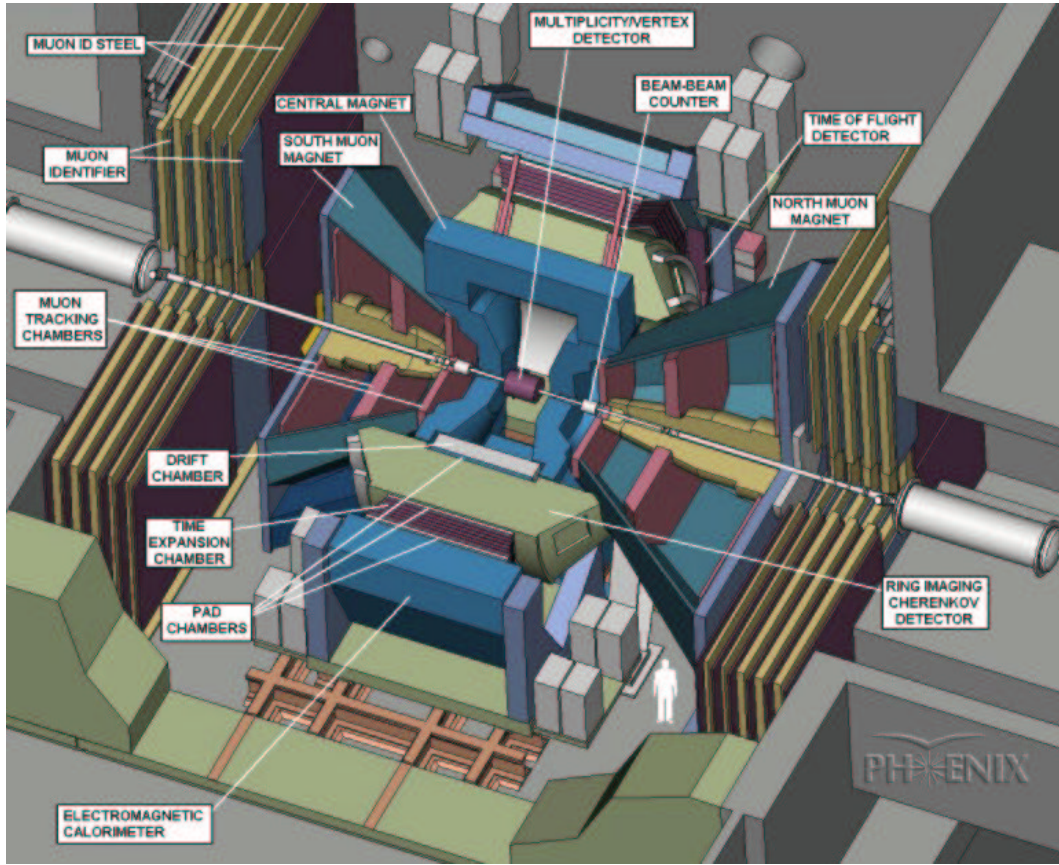
Figure 1.2: PHENIX detector set up.

The forward arms are devoted to muon physics. They consist of muon tracking chambers and a muon identification system.

Two additional subsystems play an important role in PHENIX. They are two Beam-Beam Counters (BBC) [30] and two Zero Degree Calorimeters (ZDC) [31]. These detectors are described in more details since they play a special role in the analysis.

The BBC Cherenkov detectors are located on both sides (South and North) of the PHENIX detector at 1.5 m from the center the interaction region. Each BBC has 64 channels on each side consisting of a quartz Cherenkov radiator and a PMT. The BBC covers 2π azimuthal angle in the pseudorapidity range from 3 to 4 units. The signal from the PMTs is measured for timing and amplitude. The difference in time between North and South parts of the BBC determines the event vertex position with an accuracy of $\lesssim 1$ cm and defines the time when the event occurred. The amplitude of the signal is proportional to the number of charged particles in the BBC rapidity range since practically all particles emit the same amount of Cherenkov light in the radiator.

The ZDCs are located 18 m from the center of the interaction region behind the separation magnet. The ZDC is a small area hadron calorimeter with alternating lead

Table 1.2: Summary of PHENIX Detector Subsystems.

Element	$\Delta\eta$	$\Delta\phi$	Purpose and Special Features
Magnet: central	± 0.5	360°	Up to 1.0 $T \cdot m$.
muon	$\pm 1.1 - 2.5$	360°	$0.72 T \cdot m$ for $\eta = 2$ $0.36 T \cdot m$ for $\eta = 1.3$
BBC	$\pm(3.1 - 4)$	360°	Start timing and fast vertex.
Drift chamber	± 0.35	$90^o + 90^o$	Tracking, good mass and momentum resolution, $\Delta m/m = 0.4\%$ at $m = 1 GeV/c^2$.
Pad chambers	± 0.35	$90^o + 90^o$	Pattern recognition and tracking for nonbend direction.
TEC	± 0.35	$90^o + 90^o$	Pattern recognition and tracking after RICH and dE/dx.
RICH	± 0.35	$90^o + 90^o$	Electron identification.
TOF	± 0.35	30°	Good hadron identification, $\sigma < 100 ps$.
PbSc	± 0.35	$90^o + 45^o$	Good e/π separation at $p > 1 GeV/c$ by EM shower and $p < 0.35 GeV/c$ by TOF. K/e separation at $1 GeV/c$ by TOF for dE/dx.
PbGl	± 0.35	45°	Good e/π. Photon detection
Muon chambers	$1.15 - 2.35$	360°	Tracking for muons.
Muon identifier	$1.15 - 2.35$	360°	Steel absorber and chambers for μ/hadron sep.

and scintillation plates. It covers the initial beam rapidity range and detects the free spectator neutrons left after collision. Since every neutron carries the same amount of energy (beam energy per nucleon) the signal in the ZDCs is proportional to the number of spectator neutrons. The collision vertex can also be reconstructed by reading the timing of the signals of the ZDCs, but with an accuracy $\sim$2.5 cm due to its worse timing properties compared to the BBC.

1.6 The tracking and particle identification system.

The tracking system of the central arms measures the p_T and p of charged particles and photons from RHIC collisions. Three tracking subsystems are optimized for different functions. 1) Low mass, multiwire focusing drift chambers provide high resolution p_T measurements. 2) Three interpolating pad chambers provide three dimensional space points for the charged tracks, determine p_z/p_T, and provide space points for the trigger. 3) A time expansion chamber tracks charged particles between RICH and EMCal, identifies tracks originating from outside the fiducial volume, and provides e/π separation in the momentum range of 250 MeV/c to 2.5 GeV/c using dE/dx information. All three subsystems work together to perform the tracking pattern recognition in the high multiplicity RHIC environment.

The main principle of the particle tracking in PHENIX is based on measuring the angle of the charged particle straight track outside the magnetic field. The angle of the track, determined by the integral of the magnetic field produced by the central magnet, provides the information about p_T of the particles originating from the event vertex. The measurement of the track angle is done by the DC which reconstructs several close hits per track each with an accuracy of 160 μm. The tracking resolution achieved in year-1 was $\sigma_p/p = 1\% \oplus 3.5\%p$ which is worse than initially planned. This was due to the fact that the DC in the year-1 run had inactive wire layers affecting the resolution and the incomplete alignment of the detector subsystems.

The reconstruction of the total particle momentum p requires the measurement of the event vertex and the z-coordinate of the particle track at some point in space to define the angle θ. The vertex information is obtained from the time difference in signals from the two BBCs and the z-coordinate of the particle track from the PC1 with resolution < 2 mm.

Using the three layers of PCs one can trace the particle track through RICH, TOF and TEC subsystems of PHENIX. These three detectors are primarily used for particle identification. The RICH detector identifies electrons by the Cherenkov radiation of the particles in $\sim$1 m of CO_2. The light reflected from mirrors on the back side of RICH is collected by the UV sensitive PMTs with 1.5" quartz windows and Winston cones. Each electron produces $\sim$10 photoelectrons in RICH.

The TOF detector is an array of 1000 scintillating plastic counters read by PMTs on both sides. The TOF provides a timing resolution of $\sigma \approx 80$ ps and uses the BBC signal as time zero t_0.

The TEC measures the particle track angle adding additional capabilities to the momentum reconstruction especially for particles with high momentum.

The outmost PHENIX detector, the EMCal, detects photons and has significant e/π separation capabilities. Comparing the hit energy to the momentum measured in the tracking system helps to identify electrons. The PC3 layer in front of the EMCal is used as a veto to suppress hits coming from charged particles. More details about the PHENIX tracking system can be found in [27]

1.7   Organization of the thesis.

This thesis contains two parts, a hardware part related to the PHENIX pad chambers, and a data analysis and physics part related to the determination of the charged particle pseudorapidity density $dN_{ch}/d\eta$ using the pad chambers.

The Heavy-Ion Group of the Weizmann Institute joined the PHENIX collaboration in 1997. The group took upon itself the responsibility for the design, construction and commissioning of the PC1 subsystem of the PHENIX detector. It was a very challenging project due to the special requirements of the PC1 and the very tight time schedule. The project was completed and PC1 detectors in both arms were installed on the PHENIX detector central arms in the late 1999, ahead of schedule, after passing all planned tests. The PC1 performed well in both PHENIX physics runs and is considered to be a very stable and reliable subsystem. The author of the thesis took a significant part in the design, construction and commissioning of the PC1 detectors. Chapter 2 of this thesis describes the PC1 project in great detail.

On-time commissioning of the PCs and their relative simplicity (in the sense that they do not require any special calibrations) made it possible to use them for physics analysis from the very first collisions in PHENIX. The very high efficiency of the PCs made them a suitable system to measure the charge particle multiplicity $dN_{ch}/d\eta$ in Au-Au at $\sqrt{s_{NN}}$ =130 GeV. The author of this thesis developed an analysis procedure, backed by extensive and detailed Monte Carlo simulation studies to determine the charged particle multiplicity using the PC subsystem of PHENIX. This is described in chapter 3.

The analysis of $dN_{ch}/d\eta$ showed new interesting results, discussed in Chapter 4. The results lead to the first physics paper of the PHENIX collaboration [32] and were reported by the author at the Quark Matter conference of January 2001 at Stony Brook University, NY, USA [33].

Chapter 2

Pad Chamber subsystem of the PHENIX detector

2.1   Role and requirements of the Pad Chambers

The Pad Chamber (PC) subsystem is a part of the PHENIX [27] Central arm tracking system. A detailed description of the PC subsystem can be found in [34]. Two layers of PC in the East arm and three layers in the West arm are shown in fig. 2.1. (The PC2 layer in the East arm is currently descoped.) Each layer consists of eight sectors. The PC1 sector is a Multiwire Proportional Chamber (MWPC) 1.97 m long (1.79 m active) and 0.5 m wide with a segmented cathode readout located at a radius of 2.5 m from the
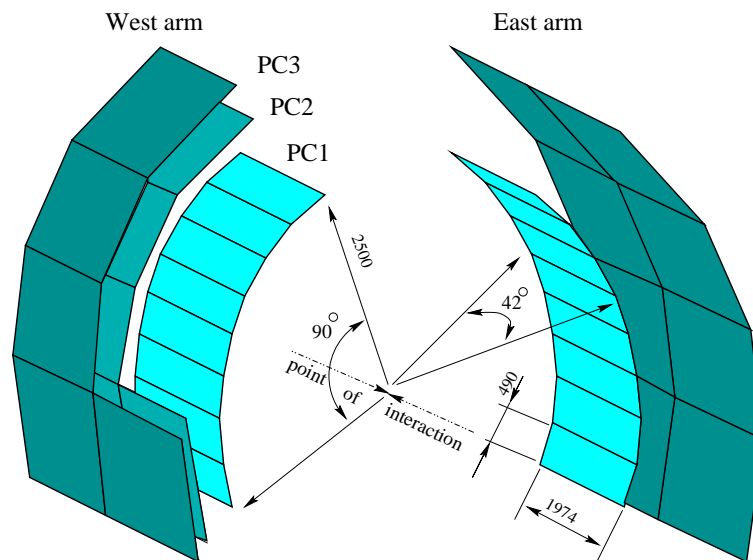
Figure 2.1: The Pad chamber subsystem of the PHENIX detector. Several sectors of PC3 and PC2 in the West arm are removed for clarity of the picture.

interaction point. Each PC1 sector covers the full acceptance of one arm ($|\eta| < 0.35$) in the polar coordinate and 1/8 of the single arm acceptance in azimuthal angle. PC2 and PC3 sectors located at radii of 4.2 m and 5.0 m respectively, have a square shape for better mechanical rigidity and cover each 1/2 of the arm acceptance in η and 1/4 of the acceptance in ϕ.

All PCs are operated in Ar/Ethane mixture (50:50) at an overpressure of 1 Torr above atmospheric pressure and at a gas gain of $\sim 10^4$. Many features are very similar for all three layers, like the pad structure, electronics, readout, mechanical design concept and operational parameters. The differences are due to their location and area.

The Pad Chambers were designed and built to fulfill the following role and have the following specifications:

- Provide reliable track reconstruction in space.
- Provide coordinate measurements of the track position in all three coordinates.
- Have very high efficiency, and minimum dead area.
- Have low channel occupancy in the environment of the most central heavy-ion collisions.
- Have low radiation thickness to minimize conversions (especially PC1).
- Provide fast position information to be used as an input to the second-level trigger

The Drift chamber (DC) and the Time Expansion Chamber (TEC) determine the track coordinates in the plane perpendicular to the beam (r-ϕ) with high resolution by measuring several close points. However, this information alone would lead to combinatorial ambiguities when the multiplicity is high. The three layers of PCs solve the problem of pattern recognition of the spectrometer by defining the straight-line particle tracks in the field-free region above the DC radius. For this purpose the r-ϕ coordinates measurement do not need to be very precise, since the transverse momentum is determined by the DC, but the highest possible detection efficiency is crucial. This also means that the dead areas should be minimized, and the PCs should have high enough granularity to operate at low occupancy for the most central events.

Based on physics simulations, a position resolution of ± 4 mm both parallel and perpendicular to the wires running along the beam direction was judged to be sufficient at the radial position of PC1. Maintaining the same angular accuracy throughout the spectrometer sets the required resolution of PC3, located at double the distance with respect to PC1, to ± 8 mm. The actual resolution achieved by the PCs is better than that and is discussed below.

A major requirement was to minimize the radiation thickness of the chambers, in particular the PC1 preceding the RICH detector along the particle track, in order to

reduce the number of electron-positron pairs from conversion of high energy photons. Although the conversions in PC1 can be eliminated in the offline analysis since these electrons cannot be followed from the DC such electrons can be a complication for the online electron trigger and significantly increase the occupancy of the RICH detector.

2.2   The pad structure of the PC

Two dimensional readout of wire chambers is done by using a cathode segmented into readout pads. A variety of cathode segmentations have been used in different MWPCs optimized for different purposes (position resolution, amplitude analysis of the hits, working in high density environment) [35]. Since the PCs have to provide space resolution it is important to consider general limiting factors affecting the MWPC spatial resolution.

The resolution across the wires of a MWPC $\sigma_\perp$ is limited by the wire pitch d, since avalanches always occur on wires. Assuming that the hit is sensed by a single wire and hits have a uniform distribution one can show that $\sigma_\perp \approx d/\sqrt{12}$. Along the wire a center of gravity technique is used to determine the hit position. In practice (e.g. [36]) with three pads of the size of the avalanche[1] and a signal amplitude analysis are enough to achieve the resolution limit determined by the primary electron statistics and the fluctuations of the gas gain.

The center of gravity technique measures the hit position more precisely when the hit occurs on the edge of two adjacent pads than when it occurs in the middle of a pad. The use of interpolating (chevron) pads reduces that difference because the charge is shared between pads more uniformly. Use of chevron pads can provide a very good position resolution, but as in other center of gravity techniques the signal amplitudes must be measured.

A completely new scheme for two dimensional readout of wire chambers was developed [37], based on a very large number of readout cells. The size of the cell and the size of the avalanche (governed by the anode-to-cathode distance) are made approximately equal to the required position resolution. The simplest possible readout, i.e. just comparing the signal with a discriminator threshold, would then be adequate to meet the requirements on position resolution and one would have a system with very low occupancy, even at the high multiplicities expected at RHIC.

A straightforward segmentation of the cathode into square pads of a size[2] $d \times d$, where

---

[1] By the size of avalanche one means the size of the charge distribution at the cathode induced by the avalanche.

[2] here and in the following dimensions are given for PC1 unless specified otherwise

d=8.4 mm with an individual electronic readout channel connected to each pad, leads to so low occupancy in the PCs which is not economically justified. The hit position resolution $\sigma_\perp$=2.4 mm is better than required, however one must account for inclined tracks hitting more than a single wire. The adopted pad geometry described here effectively saves a factor of three in the number of electronic channels while maintaining the original cell size as the basic building block. The concept is described in fig. 2.2.
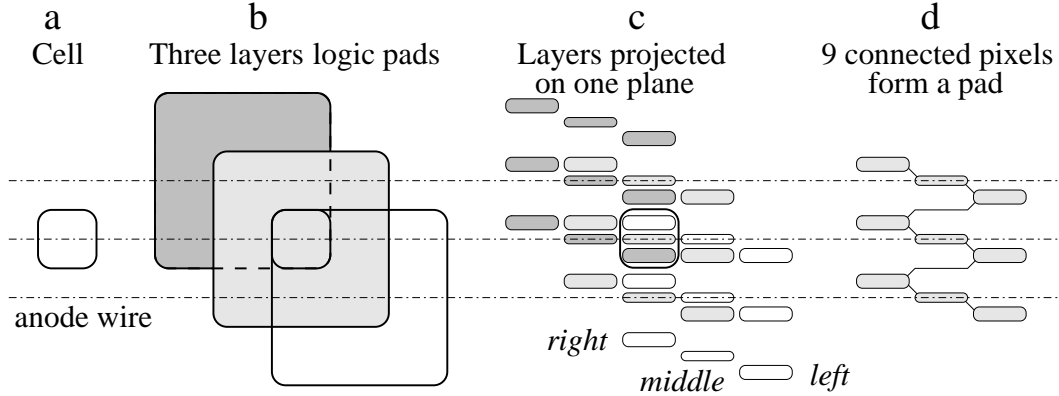
Figure 2.2: Principles of the pad geometry. **(a)** Cell of the size of an avalanche ($d \times d$). **(b)** Overlap of three larger pads defining a cell of the same size. **(c)** Three layers projected onto the same plane. **(d)** Connections between pixels on the same plane.

The size of the cell is shown to the left **(a)**. Assume that there are three separate layers of pad chambers (individual wire chambers) each with the pad size equal to 3×3 cells. By shifting the three layers by one cell relative to each other in both dimensions, one would be able to reconstruct in which cell a hit occurred, since each cell means a unique combination of pads from each of the three layers. This is illustrated in part **(b)**. In part **(c)**, each pad has been cut up in nine parts, called pixels, one in each cell covered by the pad.

The three planes of pixels can be projected onto one plane without any geometrical overlap. Since the avalanche is located on a wire, the sharing of the charge between the three pixels in the cell is only governed by the pixel geometry. The area of a pixel is chosen so that the same amount of charge is sensed, irrespective of the location of the pixel (*right, middle* or *left*) relative to the wire. That is why the pixel in the *middle* position, the one closest to the wire, is narrower than the pixels in positions *right* and *left* having equal areas. In panel **(d)**, the electrical connections between the nine pixels of a pad have been added showing that the three layers of pads can be printed on one plane. The pad structure implemented in the PCs can be understood as a chevron pad, optimized for binary readout of the channels. A small area of the cathode printed circuit is shown in fig. 2.3.
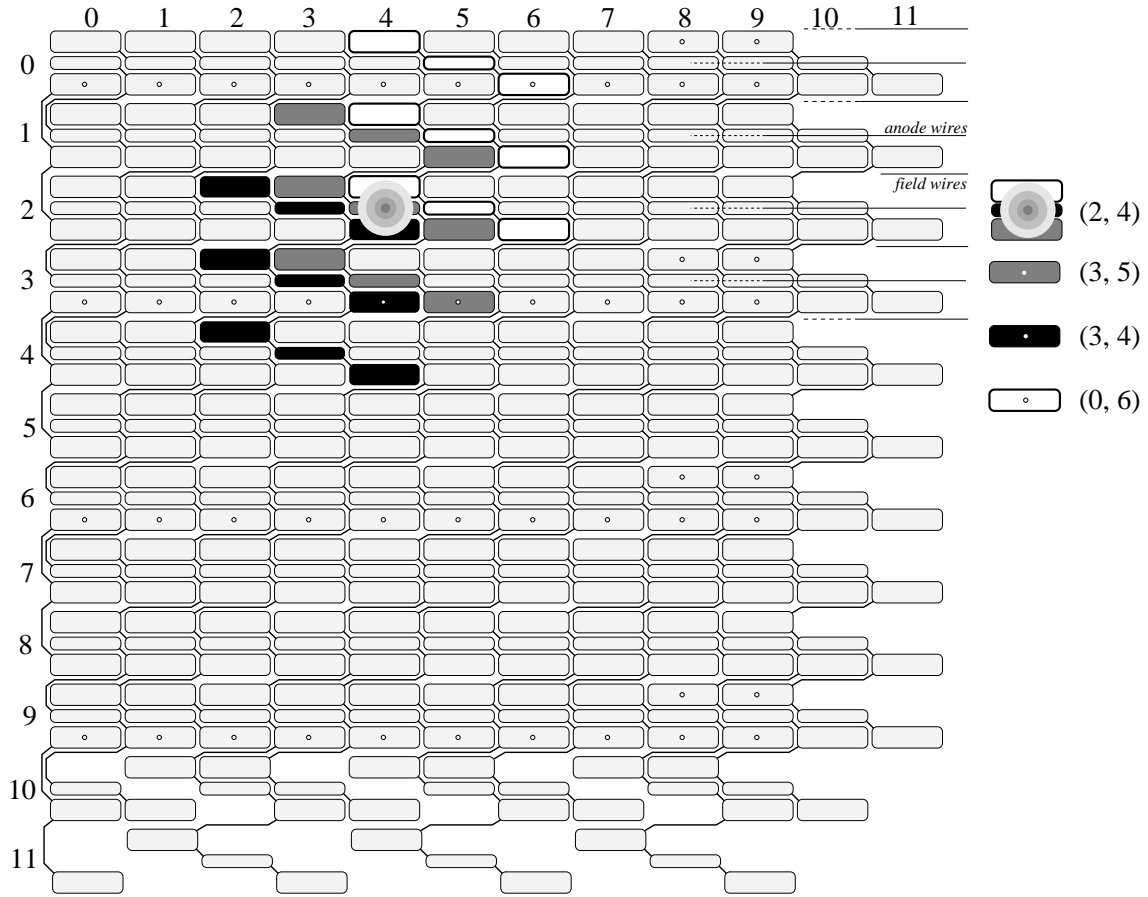
Figure 2.3: The printed circuit pattern of a PC cathode corresponding to one read-out card. Pixels at the edge of the chamber are truncated and interconnected as shown. An avalanche at the second wire in the fourth column (2,4) fires the three highlited pads. The three fired pads form one complete cell only in the position (2,4) where the real hit occurred.

The pad structure brings about some other very advantageous features. The most important one is that a valid hit will always be sensed by three adjacent pads. Since the charge sharing between the three pads is ruled by geometry and pixel areas are chosen to collect equal fractions of the charge, one can expect the requirement of triple registration to be fulfilled every time. Channels firing on electronics noise should thus be very unlikely to form false hits. Conventional discriminator-based systems have to operate at increased thresholds to avoid this situation. A drawback is the double hit resolution of the chamber since the effective size of the pad is increased to 3 cells. However, even for the most central events the occupancy of the PCs does not exceed 8% and hence causes no significant effect on particle tracking in PHENIX.

2.3   Mechanical design

As indicated in section 2.1, the amount of material in the chamber construction is essential in order to minimize γ-conversions. In order to achieve the highest possible efficiency, dead areas due to frames etc. must be avoided. Both requirements are particularly important for PC1. Thus a frameless construction was chosen for PC1, where the wire tension is counteracted by the rigidity of honeycomb sandwich structures, supporting the cathode planes.
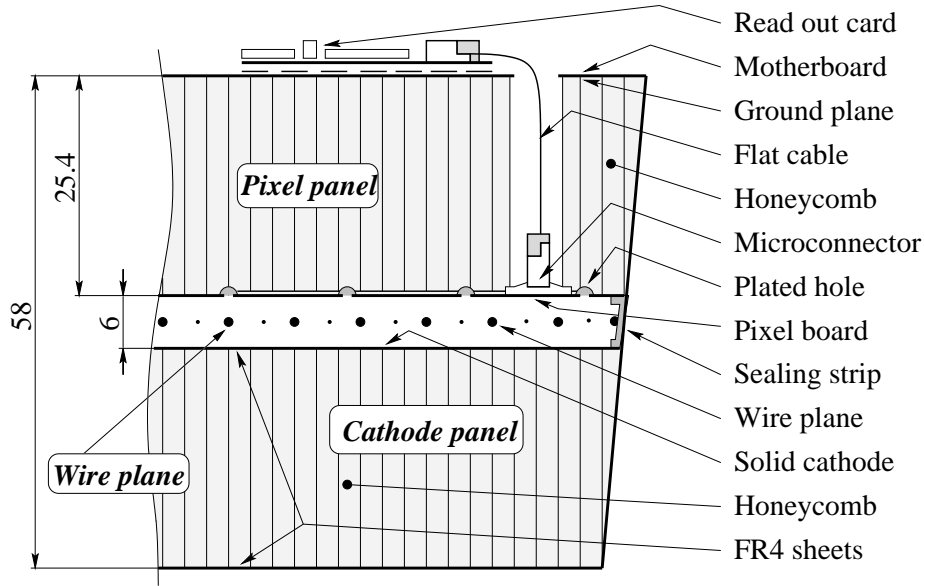
Figure 2.4: PC1 cut view.

Figure 2.4 shows the basic construction of the chambers. The PC1 is subdivided into 2×8 sectors to fit the shape of the two PHENIX central arms. The sectors have a trapezoidal shape in cross section with only 1 mm gap between two adjacent sectors to minimize the amount of dead area. Each sector is an independent chamber 1974 mm long, 495 mm wide and 58 mm thick. It is made out of two flat panels, the pixel panel and the cathode panel, and an anode wire electrode, as shown in fig. 2.5.

Both panels are almost equal in size and consist each of two 0.25 mm thick FR4 facesheets glued to a 25.4 mm thick honeycomb core. The cathode panel has a copper layer on its inner side, which serves as ground electrode. Gas is fed through recesses made in the panel heads, the honeycomb, and the facesheet to provide gas flow from one side of the detector to the other.

ROCs

Kapton cables

Pixel panel

26

Spacer

495

Sealing strip

Wire plane

HV terminals

Gas inlets

Cathode panel

Mounting supports

1974
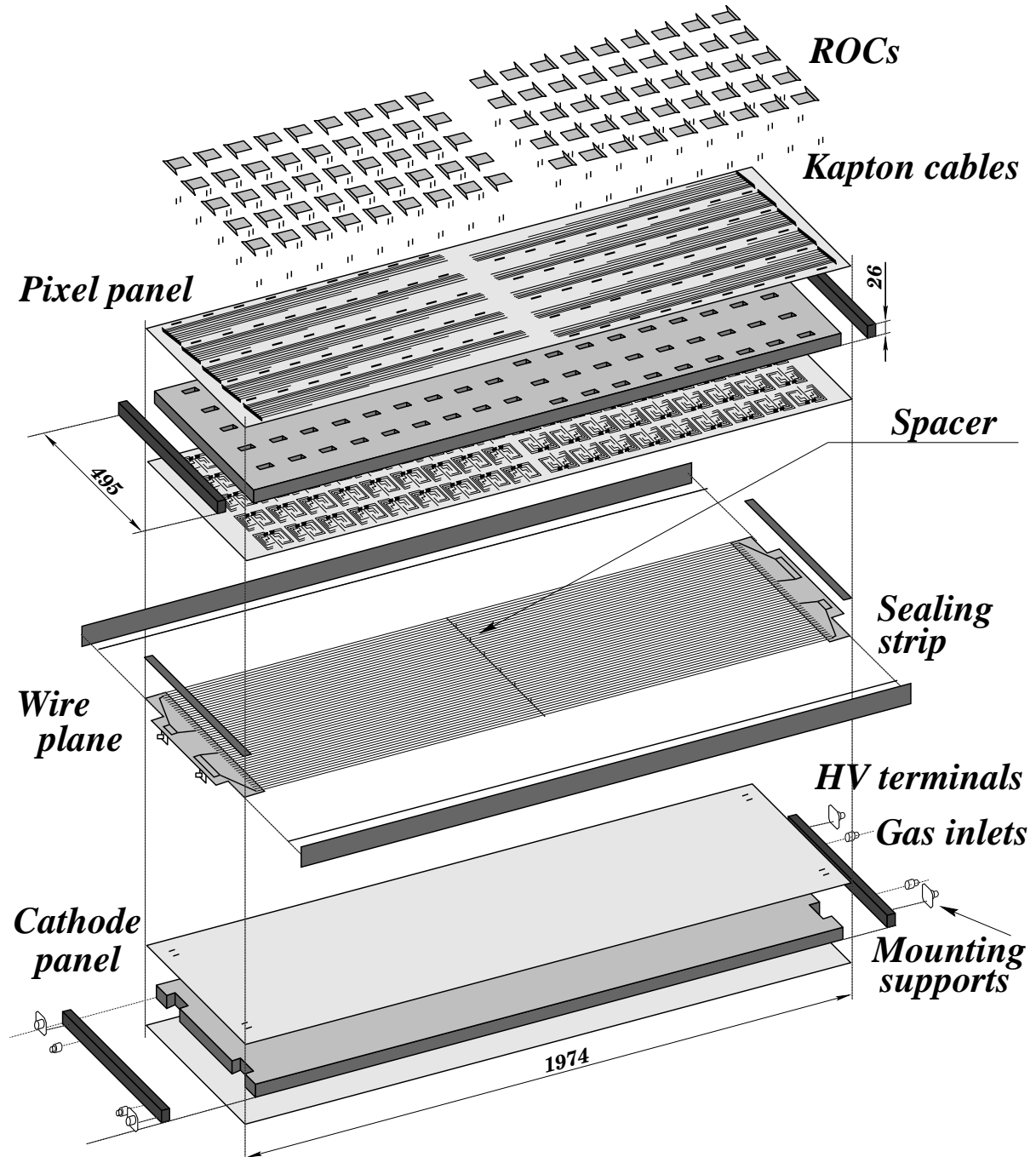
Figure 2.5: PC1 exploded view. All dimensions are in mm.

The two facesheets of the pixel panel are the pixel board and the motherboard. The pixel board is a double sided printed circuit board with the pixel pattern described in 2.2 on its inner side (not visible in fig. 2.5) and the signal traces on the other side. Approximately 4.5 thousand plated-through holes in each pixel board connect the pads to the traces. The traces are bunched into groups of 24 to a total of 180 microconnectors soldered to the ends of the traces. The signals are taken through the panel by flexible kapton cables plugged into the microconnectors and the readout cards (ROCs) on the motherboard. 48 channels are connected to one single ROC, so that there are 90 ROCs per sector.

The motherboard has 2×5 signal busses on the outer side bringing the digital signals from the ROCs to the front-end electronic module connected to the PHENIX DAQ by optical links. The inner side of the motherboard is copper clad to screen the signal traces from the noise originating from the communications in the busses. Power lines on the motherboard were reinforced with wires to avoid the voltage drop along 90 cm long traces.

The anode electrode has two types of gold plated wires running in the middle of the gas gap volume between two panels, 58 25 μm diameter W/Re anode wires, and 59 75 μm diameter Cu/Be field wires. The tension on the wires is 60 g and 120 g respectively, which is below 2/3 of their elastic limit. The basic parameters of all PCs are given in Table 2.1.

Table 2.1: Mechanical parameters of one PC sector.

Parameter	PC1	PC2	PC3
Gas gap (mm)	6.0	10.0	12.0
Number of wires	58	116	116
Wire pitch (mm)	8.4	13.5	16.0
Number of cell rows	212	106	106
Cell step (mm)	8.45	13.8	16.7
Dimensions L×W×H (cm)	197×50×6	151×157×7.2	177×185×9.0
Overall weight (kg)	7	60	80
Maximal gravitational sag (mm)	~ 1.0	< 1	< 1
FR4 thickness (mm)	0.25	0.5	0.75
Honeycomb thickness (mm)	24.5	36	49
Copper thickness (μm)	5	10	10
Radiation length (% $X_\circ$)	1.25	1.9	1.9
Dead area by design %	<0.7	6	6

The wires are glued and then soldered to two terminal boards located at the edges of the chambers. The terminal boards distribute the high voltage through individual *RC* filters to each anode wire. The wires are grouped into four independent HV sectors

limiting the loss to only 1/4 of a chamber in case of a broken wire. The wires are also glued on a 1 mm wide bar located in the center of the chamber (Spacer in fig. 2.5). The height of the bar is equal to half of the gas gap. It was introduced in order to hold the wires in the middle of the gas gap when the chamber sags due to its own weight. The gravitational sag of the wires themselves is less than 80 μm. Another purpose of this bar is to avoid possible electrostatic repulsion between the wires. The electrostatic staggering stability limit is marginally close to the total wire length.

The PC1 sectors are closed and sealed by gluing. This has the advantage of considerably reducing both the dead area and the amount of material in PC1 where it is most critical. However, the disadvantage is that repairing a chamber, once sealed, is practically impossible and thus two additional sectors of PC1 were produced as spares chambers[3]. The sealing of the chamber is ensured by gluing two 3 mm thick end beams to the two panels along the short sides. Along the long sides it is sealed with a 6 mm C-shape gas sealing strip. In addition, this element plays an important role in holding the two panels together making them as a single mechanical unit. There is an additional 0.2 mm thick sealing strip running on both sides of the chamber covering the gap and the sides of the panels. Finally, there are 6 small stands of 6 mm in height equally spaced along the wire support in PC1 glued to both panels. They hold the panels together and also help maintaining the gas gap against the gas overpressure force, which is $\sim$110 N/Torr over the full detector area.

This design gives the chamber considerable mechanical rigidity while minimizing the thickness of materials used for the construction. The PC1 sector freely suspended at the 4 corners in the horizontal position sags at the middle by less than 1 mm. This sagitta proved to cause no effect on the chamber operation.

The radiation budget of the chamber is shown in Table 2.2. It does not exceed 1.25% of a radiation length including the electronics. In part, this is achieved by moving the more massive parts of the chamber such as mechanical supports, gas fitting, and high voltage connections to the edges of the detector, outside of the PHENIX acceptance.

---

[3]After 2 years of PHENIX operation the spare chambers were not used.

Table 2.2: The PC1 radiation budget listing elements from top to bottom according to the figs. 2.4 and 2.5

PC1 element	Construction material	X_0 (cm)	Material thickness	Area (% of tot.)	Radiation length (%)
ROCs	Kapton and components	from estimation		$\sim$30	0.110
Reinforcement	Copper wire	1.43	0.2mm	0.6	0.010
Solder joints	Pb/Sn/Flux	$\sim$1	0.2mm	0.8	0.015
Traces	Copper	1.43	5μm	$\sim$40	0.015
Facesheet	FR4	17.1	0.25mm	100	0.145
Ground Screen	Copper	1.43	5μm	100	0.035
Glue joint	Epoxy	25	$\sim$50μm	100	0.020
Panel core	Honeycomb	8170	25.4mm	100	0.030
Kapton cables	Kapton+copper	$\sim$15	$\sim$100μm	10	0.005
Connectors	Nylon+copper	$\sim$20	5mm	2	0.050
Solder joints	Pb/Sn/Flux	$\sim$1	0.2mm	0.6	0.010
Glue joint	Epoxy	25	$\sim$50μm	100	0.020
Hole sealing	Epoxy	25	$\sim$10μm	100	0.005
Traces	Copper	1.43	5μm	$\sim$10	0.005
Facesheet	FR4	17.1	0.25mm	100	0.145
Pads	Copper	1.43	5μm	$\sim$90	0.030
Wires	W/Au Cu/Be	0.35,1.4	25,75μm	0.3,0.8	0.005
Gas	Air Ar/Ethane	30400,16500	51,6mm	100	0.020
Gap sealing	FR4	17.1	6mm	0.4	0.015
Sealing strip	FR4	17.1	56mm	0.08	0.025
Edge finish	Epoxy	25	$\sim$40μm	100	0.015
Cathode	Copper	1.43	5μm	100	0.035
Facesheet	FR4	17.1	0.25mm	100	0.145
Glue joint	Epoxy	25	$\sim$50μm	100	0.020
Panel core	Honeycomb	8170	25.4mm	100	0.030
Glue joint	Epoxy	25	$\sim$50μm	100	0.020
Facesheet	FR4	17.1	0.25mm	100	0.145
Total					1.25

2.4   Construction

The most critical and challenging step in the production of the chambers was soldering and testing of the pixel boards. The pixel electrode and signal transport connections to the ROCs form a very complex structure: on the detector side it consists of 36888 pixels connected into groups of 9 by tiny 150 μm wide copper traces forming 4320 pads connected to the other side of the board by the same number of plated-through holes and bunched together in groups of 24 channels where 180 microconnectors are soldered. Finally 36 mm long flexible kapton cables transport the signals to the ROCs.

The whole assembly of the pixel board, microconnectors and kapton cables has to be checked for electrical conductivity from the pixel to the end of the kapton cable and for discontinuities and shorts between neighboring traces. Clearly, standard tools are inadequate for this task. A highly reliable, efficient and very fast method to test the pixel structure was developed for this purpose [38]. The device and the various tests are described in the next subsection.

The first step of the chamber construction is soldering of the microconnectors. A procedure based on a surface-mount technology was developed to achieve a very high quality of soldering, minimize the amount of soldering material, and speed up the process. A solder paste was applied exactly at the soldering places through a 0.2 mm thick stainless steel mask. The connectors were then installed in place and the joints were heated with hot air using a surface-mount rework station HAKKO 850.

Special care was taken to minimize the amount of epoxy used for the gluing of large surfaces. The average epoxy layer thickness of approximately 50 μm, was controlled by weighting the amount of glue prepared before and remaining after each gluing operation. The gluing was done in a vacuum bag on a flat granite table to insure high quality and flatness of the surface.

The openings for the gas inlets made in the honeycomb as well as each one of the 4.5 thousand plated-through holes in the pixel board of PC1 were sealed with epoxy. Every PC1 panel was controlled for its deformation due to gravity and to intrinsic tensions in the structure of the panels. Cathode and pixel panels with similar intrinsic deformations were selected to make one detector such that the deformations would cancel each other.

Before the assembly of the anode plane the terminal boards were equipped with the electronics components and tested for HV. Terminal boards and wire support were glued to the pixel panels. The PC1 wire planes with the two types of wires were prepared on a winding machine in advance and transfered to the detector using transfer frames. The wires were aligned to the pixel pattern using an optical system, glued to the terminal boards and then soldered. Position and tension of the wires were controlled to stay within

allowed limits.

Before the permanent sealing of PC1 a preliminary test (see sec. 2.6) was performed to demonstrate that the chamber operates properly. The chamber was closed in a gas box filled with CO_2 and then with Ar/Methane (90:10). Only chambers which showed no current in the carbon dioxide atmosphere and clear anode signals in Ar/CH_4 from cosmic rays in all four sectors were approved for final sealing. The sealed chambers then underwent a more detailed test with cosmic rays. Finally the ROCs were soldered on the motherboards ($\sim$2500 contacts per chamber) using the same technique which was developed for soldering of microconnectors.

After sealing, the PC1 chambers were measured for deformation. The chambers, when suspended at the four corners have less than 1 mm sag due to their own weight, and intrinsic deformations smaller than that. It was demonstrated during the tests that even a 3 mm deformation does not significantly affect the chamber performance. The total gas leak rate of all the chambers together was found to be two orders of magnitude below the target value allowed by the RHIC safety regulations of 6 cm^3/min.

2.5   Pixel board test

As mentioned above, one of the challenges in the construction of the chambers was the pixel board testing. A procedure together with the necessary tooling including mechanics and a dedicated electronic unit was developed for this purpose. The testing procedure worked very well resulting in a high quality of the detectors [38].

General principle.

The test has two main goals: (i) check electrical continuity from the pixels up to the end of the kapton cable and (ii) find all shorts between channels. The work with a prototype chamber allowed to identify the main causes of problems in the pixel boards. It was found that the best way to detect all shorts or broken traces is by checking electric conductivity between the pads and from the pad to the end of the kapton cables. However, the complexity of the pad structure, the number of channels, and the size of the boards made it impossible to use conventional tools to solve this problem.

Using the experience accumulated with prototypes, the procedure was divided in three different tests as shown in fig. 2.6, each one intended to check for a potential class of problems.
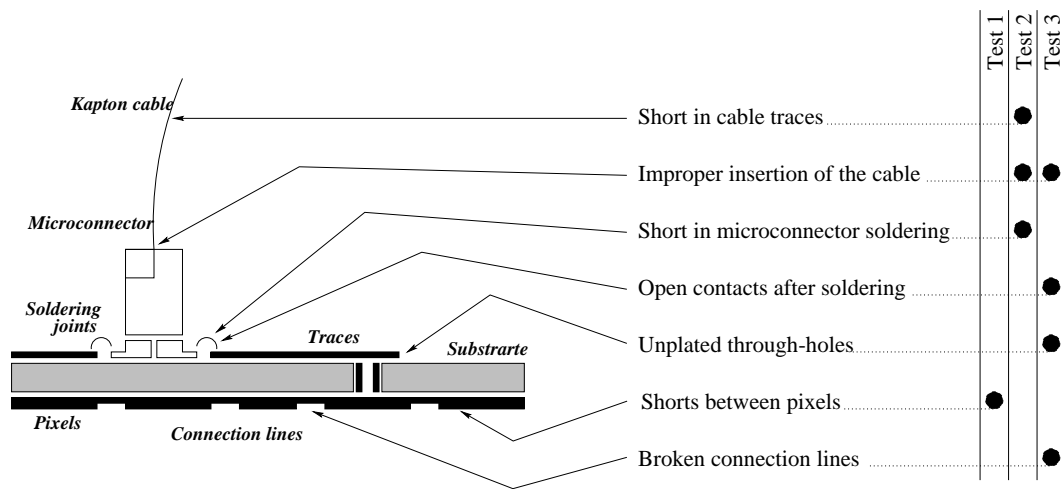
Figure 2.6: Test scheme. Potential problems in the PC are shown together with tests intended to identify the problem.

Test 1. Pixel board quality check.

Test number 1 is intended to search for shorts between neighboring pixels due to mistakes in the board production by checking electrical conductivity between neighboring pads. Spring loaded test pins (INGUN GKS-422-0123) with round head were used to make a reliable electrical contact. This particular type of pins was proved not to destroy the 5 μm copper layer of the pads. The pins were set at different voltages in the range of 1-5V. A simple electronic circuit checks the contact between pins. In order to be able to scan the board quickly and efficiently, the contact pins and the electronic unit were attached to an $X - Y$ positioning system. A drawing board modified to accommodate the PC1 pixel board with microconnectors was used as supporting stand and its tracking mechanism as $X - Y$ positioning system. A section of a pixel board together with the pin pattern is shown in fig. 2.7.

The method can be explained in the following way: the pad shown in black in fig. 2.7 could be shorted to any of its 6 neighbors shown in grey in the panel "Step 0". During the test the pattern of pins is moved through the pad structure in steps, each step corresponding to one pad column. For the "Step 1" one pin is on the black pad, and simultaneously other three pins are on grey pads. If the electronic unit issues no signal all pads are insulated from each other. Once the pad is checked it appears stripped in fig. 2.7. By moving the pin pattern further one can check (redundantly) all neighboring pads "Steps 2 and 3".
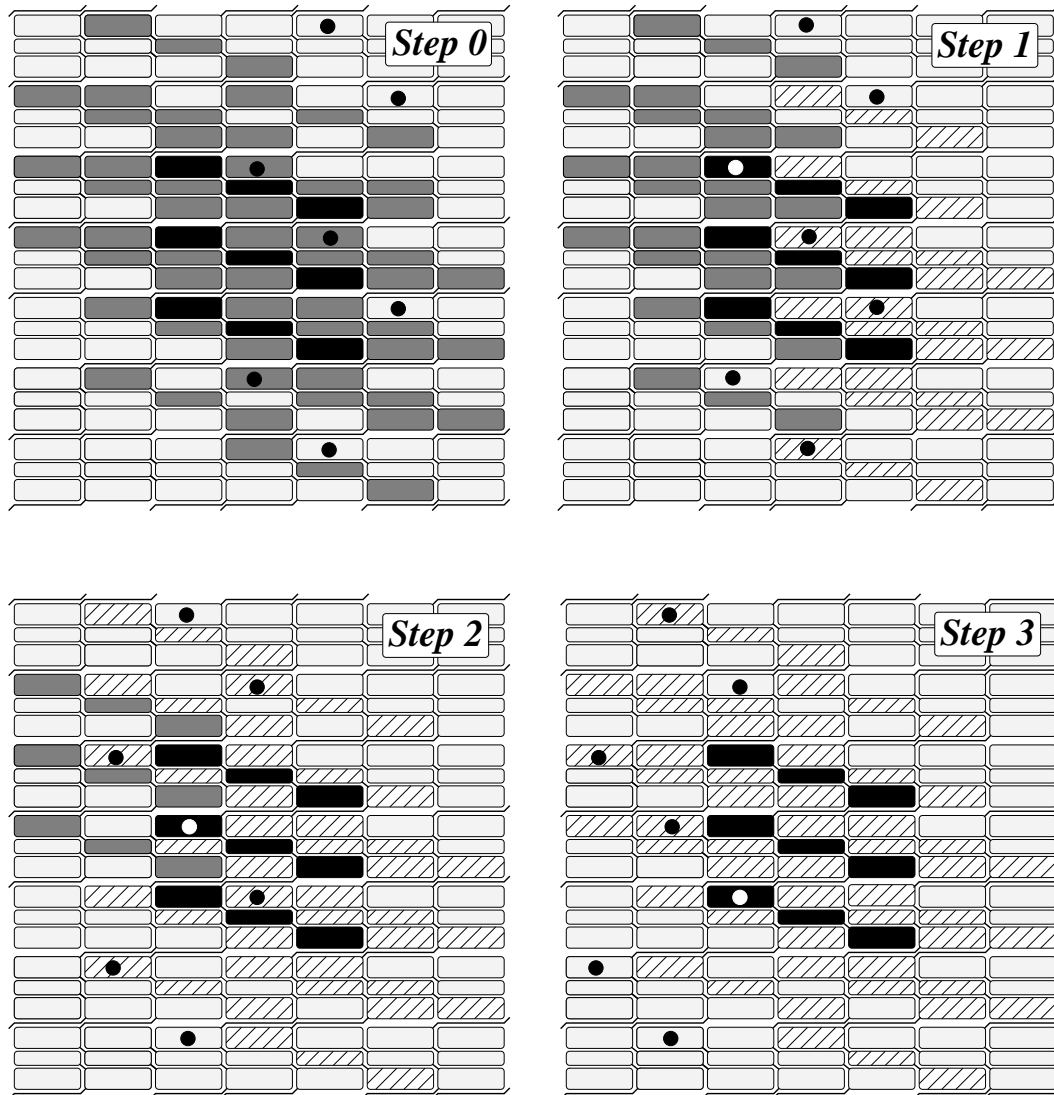
Figure 2.7: PC pad structure together with pattern of testing pins (circles). An arbitrary chosen pad is shown in black with its 6 neighbors in grey (Step 0). The pins are moved from right to left in steps. No electrical contact between pins indicates that the pads are disconnected. Pads already checked after each step (0-3) are stripped.

Test 2. Soldering quality check.

After soldering the microconnectors and inserting the kapton cables into them, the whole assembly was checked for shorts in the soldering and cables. It was learned from the prototype experience that the shorts occurred only between neighboring traces whereas all other possible shorts never appeared because of the strict dosage of the soldering material. A feature of the microconnector construction is that legs corresponding to neighboring electrical lines are on opposite sides. Thus, by shorting all the traces on one side of the microconnector with a conductive rubber one can make a reliable electrical connection of all even traces in the connector and the cable. Using a pin connected to a beeper one can scan the odd traces in the connector one by one.

Test 3. Discontinuity check.

This test intends to check the continuity of the whole chain. The pixel board was placed on the stand, pixel side up, and the open end of all kapton cables were shorted to ground on the back side of the board. If there are no broken connections in the channels each pixel must be connected to ground. A different pattern of pins checks the grounding of the outmost pixel in each pad in a way similar to what was done in test number 1.

2.6   Testing of the pad chambers

At the final stage of the production and during commissioning all PC1 chambers passed a series of tests with cosmic rays intended to demonstrate their degree of readiness and performance.

To perform these tests two cosmic ray triggers were assembled one at Weizmann Institute and one at BNL. They are shown in fig.2.8. They consist of two sets of plastic scintillation counters (Sc.1,2 and Sc.3,4 in the WIS setup and Sc.1,..5 and Sc.6,..10 in the BNL setup) located above and below the chamber together with NIM based fast logic electronics. Additional scintillators counters were used for the efficiency (Sc.11,12) and spatial resolution (Sc.13) measurements. The main parameters of the test facilities are summarized in Table 2.3 and more details of the measurements can be found in [34].

The first test was done during the production stage to ensure good electrostatic properties of the PC1 before they were permanently sealed. The purpose of the second test was to check that the chambers are fully operational before being shipped from the Weizmann Institute to BNL. In these two tests cosmic ray spectra were accumulated at
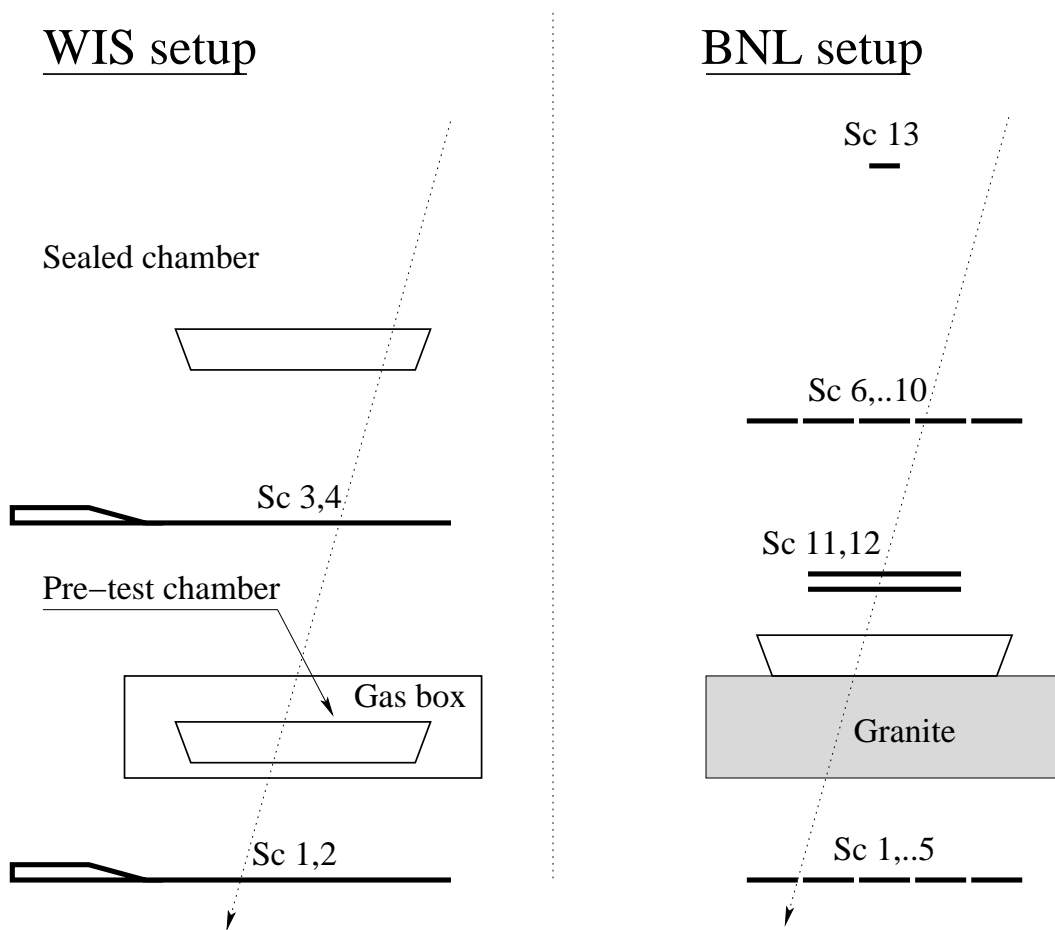
Figure 2.8: Cosmic triggers assembled at the WIS (left) and BNL (right) for the chamber testing.

16 different locations (4 points per one anode wire in each HV sector). The signals were measured using standard analog readout electronics (preamplifier, shaper and ADC). A sample of typical spectra are shown in fig. 2.9.

The final test for the commissioning of the chambers was done at BNL. Full mapping of the electronics channels was done for each chamber and the performance of one arbitrarily chosen chamber of each type was studied in great details (efficiency, resolution, gas gain, gas gain uniformity). The results of the PC performance studies are presented in the next section.

Table 2.3: Main parameters of the test facilities.

Parameter	at WIS	at BNL
Triggering area (cm^2)	2 sets of 10×50	170×50
Counting rate (s^{-1})	~ 1	~ 40
Signals taken from	4 anode wires	all ROCs
Fraction of useful trigger events (%)	$1 - 2$	~ 90
Gas for conditioning	CO_2	N_2
Gas for data taking	P10	Ar/C_2H_6
DAQ	LeCroy ADC2249A	PHENIX DAQ
Time to test one chamber (days)	3	1
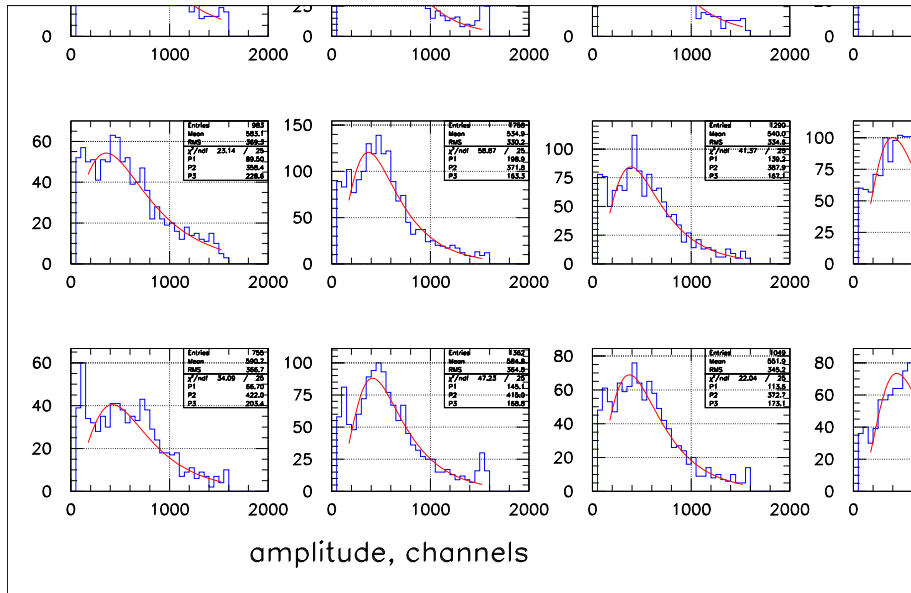
Figure 2.9: Wire signal from one PC1 chamber measured at 16 locations with the cosmic trigger. The fitted curves are the Landau fits given by eq. 2.3.

2.7   Understanding of the pad structure performance

2.7.1   Induced charge distribution

The readout of the PC pad structure is fairly easy to simulate since the image charge distribution on the cathode is well known [39]. These simulations were done in the design phase and were verified by studies of small prototype chambers [40, 41].

In this section an analytical approach [42] is used to explain the basic parameters of the concept. This approach is less accurate than the simulation, however it is more transparent for understanding several features of the pad structure.

The induced charge distribution in the cathode of a MWPC can be described by a semi-empirical expression [39] in terms of a single parameter. The charge $\Gamma(\lambda)$ collected by the cathode can be written as follows:

$$\Gamma(\lambda) = K_1 \frac{1 - tanh^2(K_2\lambda)}{1 + K_3 tanh^2(K_2\lambda)},$$

$$K_1 = \frac{K_2\sqrt{K_3}}{4 arctan(\sqrt{K_3})},$$

$$K_2 = \frac{\pi}{2}\left(1 - \frac{\sqrt{K_3}}{2}\right) \qquad (2.1)$$

where $\lambda = x/h$, x is the distance from the avalanche position (along an axis parallel or perpendicular to the wire direction) and h is the anode-to-cathode spacing[4]. Expression 2.1 assumes that the avalanche is symmetric around the wire. The distribution $\Gamma(\lambda)$ is normalized to $1/2$ of the anode charge since the readout is on one cathode only. The parameter K_3 depends on the chamber geometry and varies between 0 and 1 (see fig.2 in ref. [39]). The value of K_3 for PC was chosen to be 0.4 for the induced charge distribution in the direction normal to the anode wire. The choice was based on a comparison of the distributions obtained with expression 2.1 and GARFIELD [43]. For the longitudinal distribution $K_3 = 0.6$ was chosen according to the graph presented in [39].

Expression (2.1) can be integrated to obtain the induced cathode charge within defined boundaries. The (indefinite) integral of the expression 2.1 is given by:

$$I(\lambda) = \frac{-sign(\lambda)}{8 arctg(\sqrt{K_3})} arcsin\left(\frac{1 + \Delta cosh(2K_2, \lambda)}{\Delta + cosh(2K_2\lambda)}\right)$$

---

[4]This expression uses a reduced coordinate λ. The cell size in these coordinates is $-1.4 < \lambda < 1.4$. Because of the scaling of the PC dimensions the discussion is equally applicable to PC1, PC2 and PC3.

$$\Delta = \frac{1 - K_3}{1 + K_3} \tag{2.2}$$

Using the pad geometry described in section 2.2 and the formula 2.2 one can calculate the amount of charge induced on the pads as a function of the hit position λ along the wire. The results are shown in fig. 2.10.
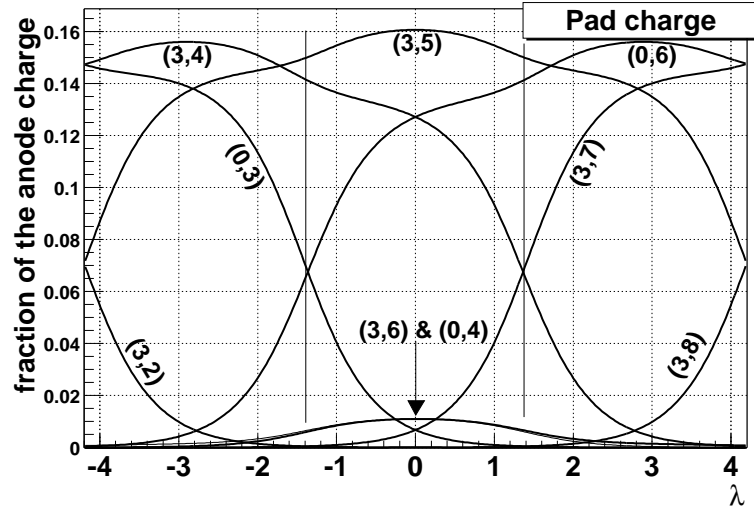
Figure 2.10: Charge induced on the pads as function of the hit position along the wire λ. Zero corresponds to the avalanche located in the middle of the cell (2,4) as shown in fig. 2.3. Pad notations are also taken from there. Vertical bars indicate cell boundaries.

2.7.2   Cluster shape

As mentioned in 2.2 the charge division between adjacent pads is governed only by the pad geometry. Therefore the charge division between pads at any avalanche position does not depend on the absolute charge in the avalanche. The charge distribution on the anode wire can be approximated by a Landau distribution $L(z)$:

$$L(z) = \frac{1}{\sqrt{2\pi}} e^{-\frac{1}{2}(z + e^{-z})}$$

$$z = \frac{q - q_{mp}}{\xi} \tag{2.3}$$

where q_{mp} is the most probable energy loss, and ξ is the difference between the average energy loss and the most probable energy loss. Assuming that the fluctuations of the gas multiplication factor M do not change the shape of the distribution 2.3 and that the noise in the electronic channels is low the charge seen on the pads has the shape described by 2.3 with q_{mp} and ξ scaled by $M \times c_i(\lambda)$, where $c_i(\lambda)$ are the curves shown in fig. 2.10.

The measured signal from the anode wires in PC1 [44] produced by cosmic particles was fitted by the Landau function and ξ/q_{mp} was found to be 1/3. The same value was measured in [40] under similar experimental conditions.

Integrating the Landau distribution above a given threshold t gives the probability $p(t, q_{mp}, \xi)$ to get a signal above the threshold:

$$p(t, q_{mp}, \xi) = \int_t^\infty L(z)dz = 1 - \int_0^t L(z)dz =$$
$$1 - \left[erf\left(\frac{e^{q_{mp}/2\xi}}{\sqrt{2}}\right) - erf\left(\frac{e^{(q_{mp}-t)/2\xi}}{\sqrt{2}}\right) \right] \approx$$
$$erf\left(\frac{e^{(q_{mp}-t)/2\xi}}{\sqrt{2}}\right);$$
$$p(t, q_{mp}, 1/3q_{mp}) \approx erf(3.17 e^{(-3/2)t/q_{mp}}) \tag{2.4}$$

From eq. 2.4 one can see that the most important parameter responsible for the PC performance is the ratio of the threshold in the pad to the total anode charge t/q_{mp}. In the following, a reduced threshold $t/q_{mp} \to t$ is used i.e. the threshold expressed in terms of the most probable anode wire charge. From the analytic studies shown below, the simulation and the prototype measurements it was found that $t \approx 0.025$ is the optimal value providing high efficiency and the best resolution.
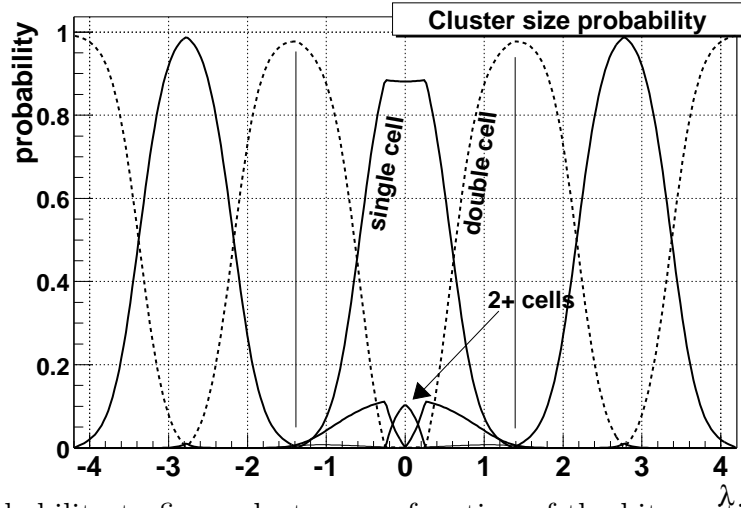
Figure 2.11: Probability to fire a cluster as a function of the hit position along the wire λ. Zero corresponds to the avalanche located in the middle of the cell (2,4) as shown in fig. 2.3. Vertical bars indicate cell boundaries.

A hit is detected in the PC when at least 3 adjacent pads, i.e. at least one cell, have a signal above threshold. Using this definition one can calculate the probability that the particle hit results in a cluster (a group of adjacent cells) of a given shape. The probability

to find a cluster with one or more adjacent cells as a function of λ is shown in fig. 2.11 for $t = 0.025$. At this threshold the majority of clusters have only one or two cells.

2.7.3 Efficiency and resolution

The sum of all curves shown in fig. 2.11 represents the PC efficiency as a function of the hit position. Figure 2.12 shows the average PC efficiency as a function of the reduced threshold t and compares calculations to the measured data. Figure 2.12 clearly demonstrates the validity of the t/q_{mp} scaling for all 3 layers of PCs. At the chosen threshold $t = 0.025$, all chambers operate above 99% efficiency as seen both from measurements and calculations. At higher thresholds, the measurements seem to have a larger efficiency than the calculation. However, the two are in good agreement within the systematic errors which are large in the data ($\sim 30\%$) due to uncertainties in the absolute gain determination related to the fact that the PCs do not have wire readout [34] foreseen in the design.

On a more basic level one can understand the behavior of the curve in the left panel of fig. 2.12 from the calculations shown in fig. 2.10. At the cell boundaries the charge is effectively shared between 4, not 3 pads, and the two pads get approximately twice less charge than the other two. The cell boundaries are therefore the weakest points for the chamber efficiency. The low efficiency region which develops there propagates along the wire as the threshold t increases.
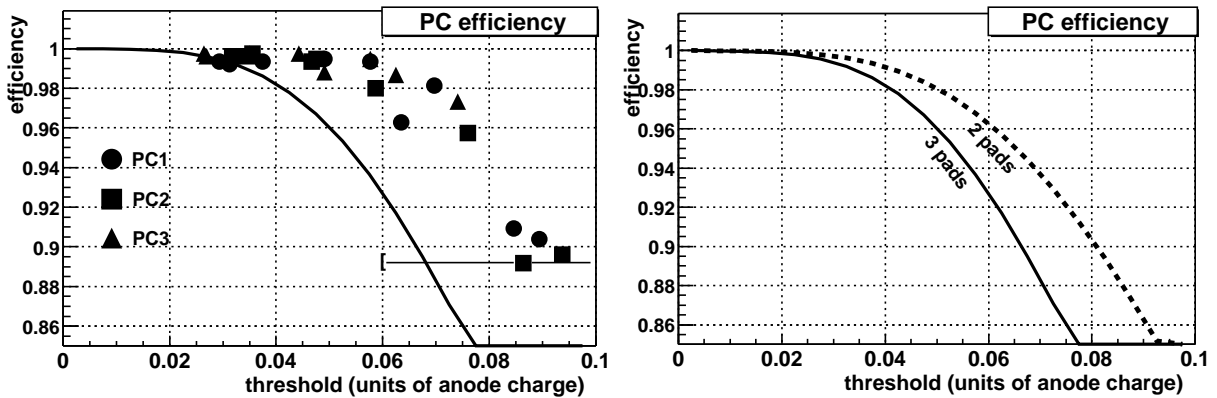
Figure 2.12: The PC efficiency as a function of the pad threshold. In the left panel the calculated efficiency curve is compared to measured values showing agreement within systematic errors (shown for one point). In the right panel the solid curve shows the efficiency calculated for minimum 3 fired pads and the dashed curve for the relaxed requirement of only 2 fired pads per hit.

The efficiency can be increased in the off-line reconstruction by relaxing the

requirement of minimum 3 pads fired per hit. Under that condition the fraction of fake hits in the chamber is still negligible. The dashed curve in fig 2.12 demonstrates that requiring only two fired pads per hits marginally improves the chamber efficiency at higher t. In addition, this relaxed hit definition results in a worse position resolution by a factor of 4, but only for the small fraction of hits having two pads hits (difference between dashed and solid curves).

The pad chamber resolution can also be calculated from the curves in fig. 2.11. It is seen that single cell clusters are centered at the middle of the cells and double cell clusters at the boundary of the cells. By measuring the width of the peaks in fig. 2.11 one can calculate the PC resolution along the wire. The result of the calculation as a function of the reduced threshold is shown in fig 2.13, compared to the rough estimate for $\sigma_\parallel = (d/2)/\sqrt{12} = 0.4\lambda$ where "d" is the cell size.
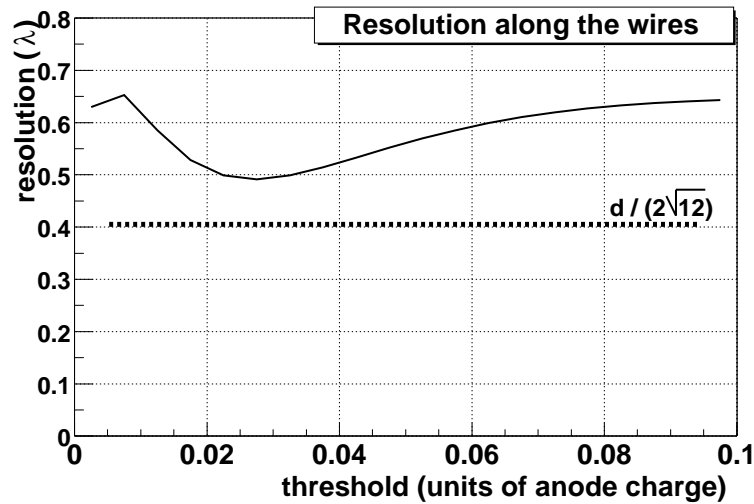
Figure 2.13: The PC resolution as a function of the pad threshold.

One can see from fig. 2.13 that the PC resolution has a rather weak dependence on the threshold and the PC performance should be robust for a broad range of threshold settings. The measured values of the PCs resolution [34] is 1.7 mm (0.57λ) for PC1 and 3.1 mm (0.62λ) for PC2 along the wires in very good agreement with the analytic calculations for an optimal threshold in the pads. The measured position resolution across the wires is consistent with the wire pitch of the PCs.

2.7.4   Cluster size ratio and PC efficiency monitoring

The cluster size probability as a function of the reduced threshold is shown in fig. 2.14. The probability of a single cell cluster grows with threshold and the probability of the

double cell cluster decreases.
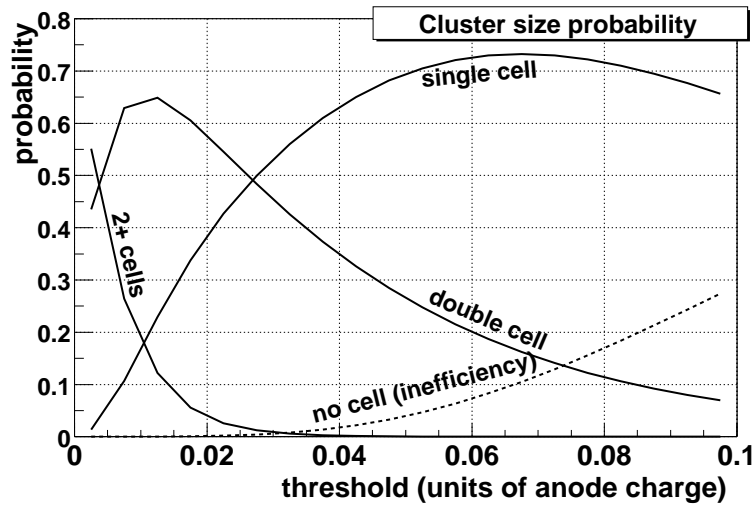
Figure 2.14: Cluster size probability as a function of threshold.

For the PC operation the threshold should be chosen such that the efficiency of the chambers is high (at least 99%), and the contribution of big clusters is low (low occupancy). A reduced threshold $t = 0.025$ fulfills these requirements.

For a fixed value of the threshold, the ratio of double to single cell clusters R(2:1) is sensitive to the value of the gas multiplication M in the PCs as follows from eq. 2.4. Thus, the R(2:1) can be used as a measure of the gain and as a monitoring parameter for the PC efficiency.
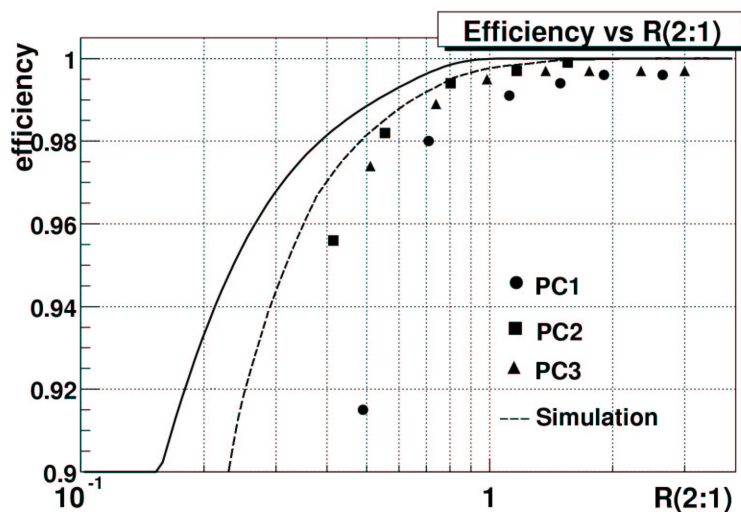
Figure 2.15: Efficiency vs double/single cluster ratio R(2:1). Analytical curve (solid line) is shown together with measured data (symbols). Dashed line is analystical calculation smeared to take into account noise, initial angles, etc...

Figure 2.15 shows the PC efficiency vs. the R(2:1) ratio. The calculation reproduces the data within ∼30% accuracy. Smearing the calculation by addind some simulation elements to account for noise in the pads, incident angles of the particles, etc... brings the calculations close to the data.

The R(2:1) is used for the PC on-line monitoring during experimental runs. The condition for full efficiency is that R(2:1) should be around 1 or higher. A snapshot of the PC online monitoring page is shown in fig. 2.16. All PCs have R(2:1) close to or above 1 corresponding to more than 99% efficient operation of all PCs.
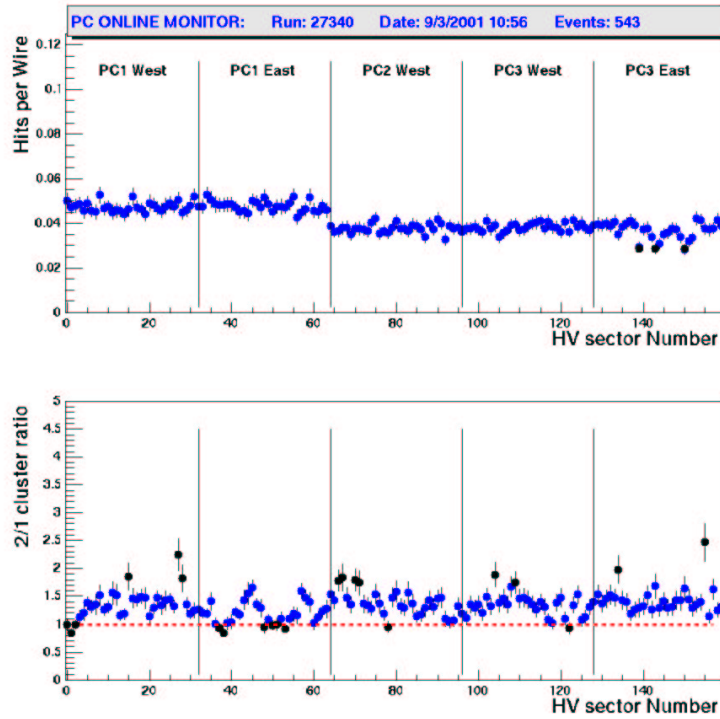
Figure 2.16: On-line monitoring page of the PC. The top graph shows the average number of hits per wire in PC high voltage sectors (4 per each module). The lower graph shows R(2:1) for the same sectors.

2.7.5   Double hit resolution

The pad structure implemented in the PCs uses 3 times less electronic channels compared to the straightforward segmentation of the readout cathode into pads of size d. It was mentioned in section 2.2 that this solution leads to an increase in the PC occupancy, although still keeping it at low level. A direct consequence of this pad structure is an impact on the double hit resolution (DHR).

The DHR itself is not the most important requirement for the PCs since the hit is not lost as in case of low efficiency, but is merged with a neighboring hit. The track reconstruction can be made insensitive to DHR by allowing 2 neighboring tracks to share the same PC hit. However, the DHR plays an important role in the charged multiplicity determination described below, and is discussed here in more detail.

As mentioned in section 2.2 the DHR of the segmented readout structure is approximately equal to the size of the segmentation element (the pad). For the PC pad structure this approximation gives a correct estimate. It can be explained using fig. 2.17.
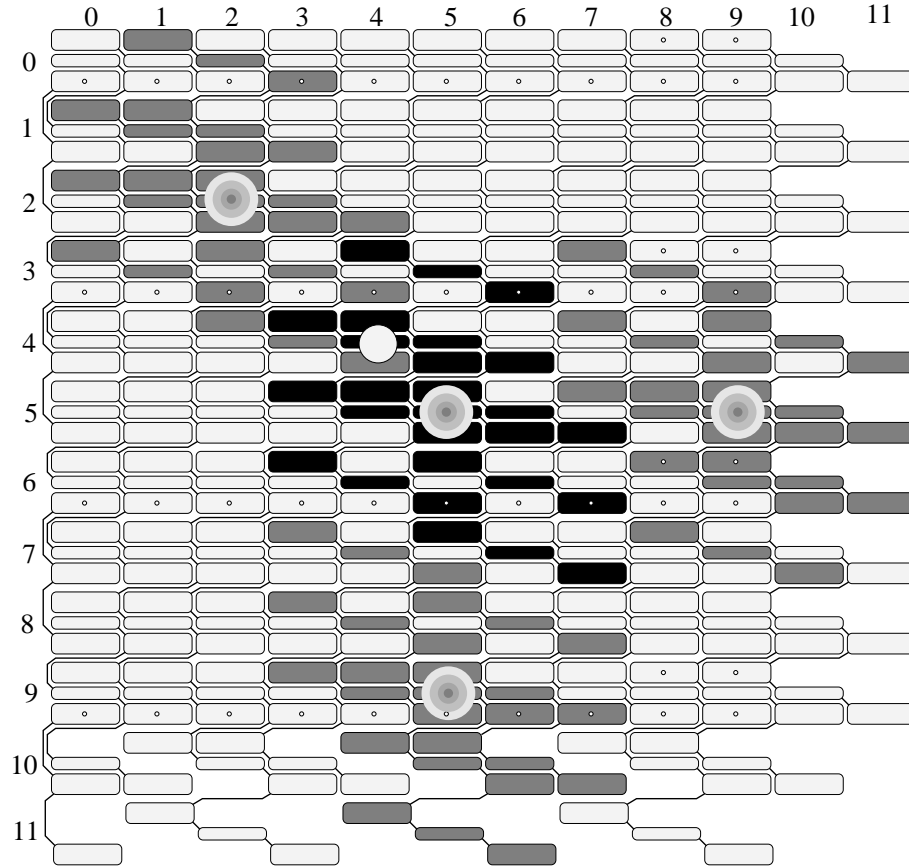
Figure 2.17: Several cases of hit location on the PC readout plane. Close hits (5,9) and (9,5) shown in grey require 4 cells to be resolved from the main hit at (5,5), shown in black. A close hit in the top left cell (2,2) is resolved from the main hit, however it produces a fake hit at (4,4).

Consider a particle hit in the center of fig. 2.17 at position (5,5). The pads fired are shown in black. A test hit is placed on the right side at position (5,9) and the pads fired are shown in grey. All cells between them are incomplete (have less than 3 fired pixels), and therefore the two hits are reconstructed as two separate ones. Moving the test hit one cell to the left would fire pad (6,8) and would result in the merging of the two hits in

one cluster. One can see that the separation of two single cell hits requires at least 4 full cells (distance $4d$) between their centers. The same is true for a test hit in the vertical direction, e.g. at position (9,5). Assuming that most of the hits in the PCs produce single or double hit clusters as shown in fig. 2.11, the PC DHR is $\sim 4.5d$ (12.6λ or 38 mm for PC1).

A different situation arises when the test hit is displaced both in horizontal and vertical directions with respect to the first hit, e.g. at position (2,2) in fig. 2.17. The distance between them is $> 4d$ and they are resolved, however there is a new complete cell (4,4) which will be treated as an additional hit, a fake one, in the reconstruction. Note that a real particle at an incidence angle close to 90° cannot produce a diagonal cluster (compare cluster probabilities shown in fig. 2.11) and all diagonal clusters are treated as two separate hits.
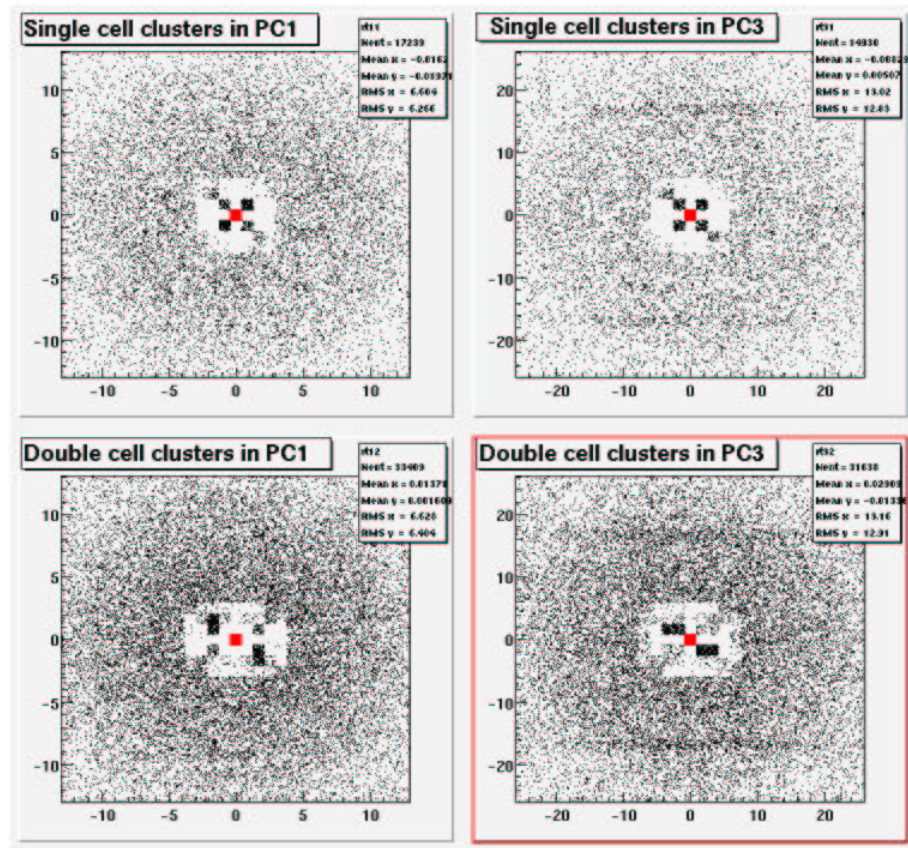
Figure 2.18: Two dimensional distribution of the closest hit for single (top) and double (bottom) cell clusters in PC1 (on the left) and PC3 (on the right). The main cluster is at the origin. There is a dead zone around it with fake clusters seen along the diagonal.

This effect is certainly small, because it requires a very special location of hits on the pad structure, and can be avoided in the reconstruction by special means. Figure 2.18

shows measured two dimensional distributions of the closest hits position for single and double cell clusters in PC1 and PC3. The first hit is always at the origin. One can see a dead zone around it, defining the DHR and four clusters fired on diagonals which are the fake hits.

2.8 PC1 in the two first PHENIX runs.

By the end of 1999 all 16 PC1 sectors were installed (fig. 2.19) on the Central tracking arm after a full cosmic test. That allowed to start the year-1 physics run of PHENIX with a tracking system in both arms. Out of 69120 channels in PC1 about 20 were found
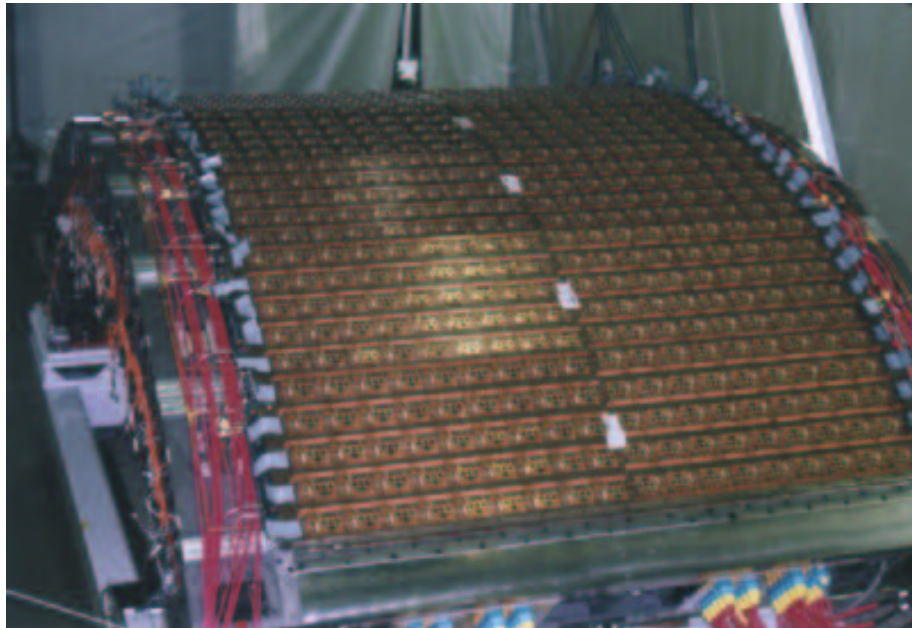
Figure 2.19: PC1 installed on the DC before going into carriage of the PHENIX West Central arm

nonfunctional due to failures in the production. This amount of nonfunctional channels is exceptionally good. Besides that, 10-25 ROCs (out of 1440 in both arms, shown in fig. 2.20) ceased operating due to various reasons, bringing the total count of dead areas in PC1 to $\sim$2.5% including the 0.7% foreseen by the design. This amount of inactive zones is acceptable and does not have any significant effect on the particle tracking.

All PC1 in PHENIX were operated during physics run with the parameters optimized from the results of the cosmic test. The HV was set to 1700 V ($M \approx 1.2 \times 10^4$), gas flow to $\sim$100 cc/min and the threshold in the electronics channels to 5-6 fC same in all PC1. Very little adjustment of these parameters was necessary during the data taking. At the beginning of the first run the trip frequency in the PC1 high voltage sectors was high. It
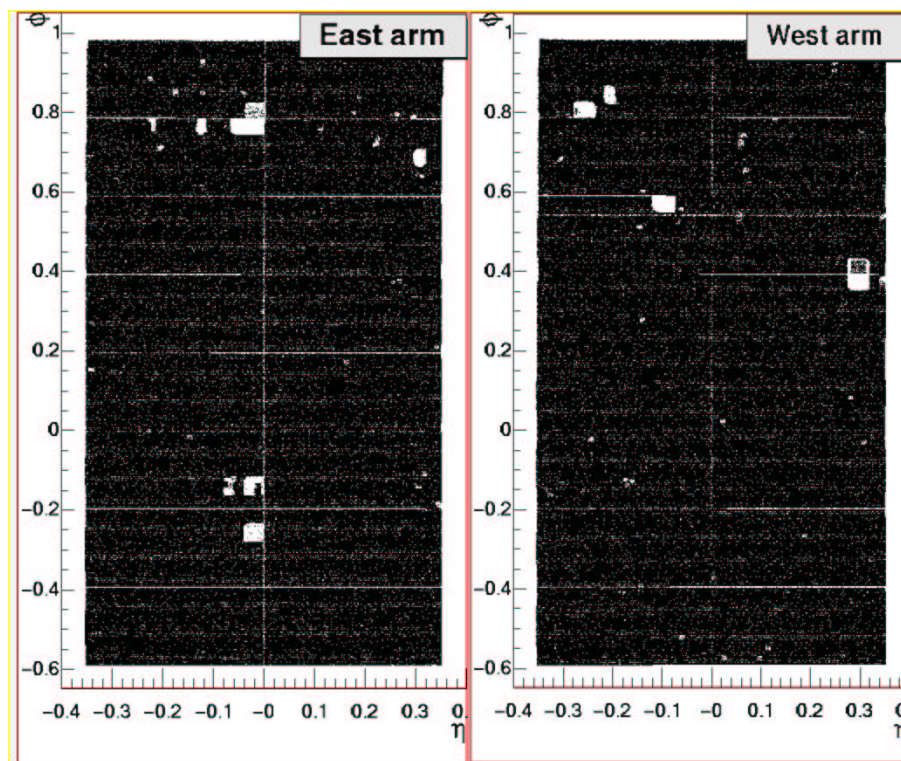
Figure 2.20: Hit distribution in PC1. The white lines are inactive zones at the chamber junctions (horizontal) and spacer (vertical at $\eta = 0$). Open rectangles are the inactive readout cards.

was later related to the extensive beam losses in the PHENIX interaction region during energy ramp up in RHIC. To avoid this problem the high voltage in PC was reduced during ramp up and before beam dump. With this precaution, the PC1 subsystem behaved very reliably. Its operation was maintained by non-expert shift personnel of the PHENIX detector and required minimum attention of the PC expert group.

Chapter 3

Charged particle multiplicity analysis

This chapter describes the charged particle multiplicity measurement done using the Pad Chamber subsystem of the PHENIX detector. $dN_{ch}/d\eta$ is an important characteristic of the heavy ion collision at high energy as mentioned in 1.2. It carries information about mechanisms of the particle production and helps to distinguish between several theoretical predictions [7].

The charged particle multiplicity was measured at $\sqrt{s_{NN}}$ =130 GeV in Au-Au collisions in the first physics run in year 2000 (year-1) and at full RHIC energy $\sqrt{s_{NN}}$ =200 GeV in the second run in year 2001 (year-2).

The two layers of PC installed in year-1 in the East arm provided an excellent opportunity to measure the charged particle multiplicity as soon as the first data became available. The PCs, pretested and installed on time did not require any additional calibrations to provide reliable data.

The number of primary charged particles in the event is determined on a statistical basis by correlating hits in PC1 and PC3, rather than by explicit track reconstruction. The analysis procedure was developed and corroborated by extensive Monte Carlo studies using the GEANT [45] response of PHENIX detector to the events generated with HIJING [13]. The year-2 data analysis uses the same approach as in year-1 with only minor refinements. The analysis is described in this chapter.

3.1   Event selection

File selection

The multiplicity analysis is based on data taken without magnetic field. Most of the files were obtained at the beginning of the run when the detector was operating in a "warming-up" mode. As a consequence some files taken in this period did not contain all the necessary information. To avoid this problem all major parameters involved in the analysis (PCs, BBCs and ZDCs) were surveyed prior to the analysis, and only files containing quality data were selected.

Figure 3.1 shows for each file an average per event[1] value of the major parameters of the detector performance plotted versus file number. The monitored parameters are the signal amplitudes in the BBC and ZDC and the number of hits per wire and ratio of clusters R(2:1) in the PCs (see sec. 2.7). The PC monitoring was done for each front end module (16 per each layer in one arm) while only one module is shown in fig. 3.1. The monitored parameters in all files stay around their average values, besides one file
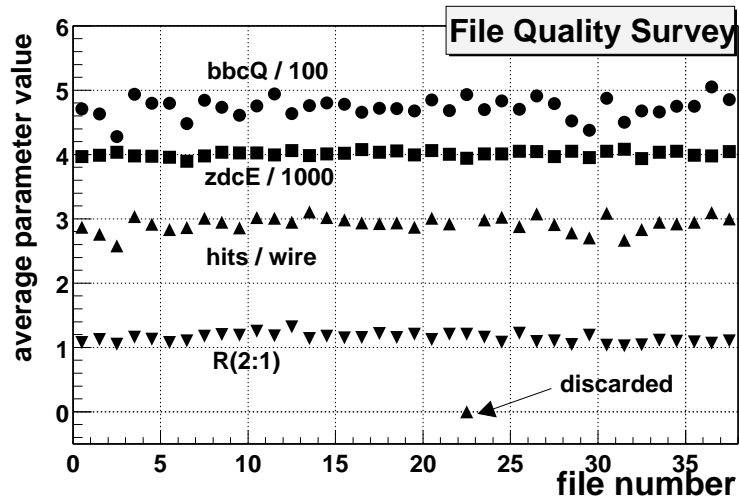
Figure 3.1: Average values of the major parameters in the data files. Top lines are BBC and ZDC average signals per event scaled to fit the range of histogram. The lower two parameters are the number of hits per wire and the R(2:1) cluster ratio (see 2.7) shown for 1/80 part of the PC subsystem.

(number 22) which has a very low number of hits per wire due to some problem during data taking. All files with such or similar problems were discarded in the analysis.

---

[1]more than a thousand events per file

Event vertex restriction

The collision vertices in the RHIC interaction regions have a wide distribution determined by the ion bunch length which is rather long (~ 2 m). As a result some collisions occur at the edges or even outside the PHENIX interaction region. Therefore the event vertex has to be restricted online using the BBC time signals in the level-one trigger (BBCLL1), and then offline with tighter cuts to avoid edge effects.

In year-1 the online vertex cut was set to $|z_{vert}| < 20$ cm and in year-2 $|z_{vert}| < 45$ cm from the center of the PHENIX interaction region. The offline vertex selection was 17 cm and 25 cm in the first and second run, respectively.

Trigger selection

The PHENIX experiment is designed to run with a variety of triggers simultaneously. The main trigger used in this analysis is the BBCLL1 inclusive trigger requiring a coincidence of the North and South sides of the BBC detector with a minimum of two channels fired on each side. The "inclusive" BBCLL1 trigger means that the BBCLL1 fires irrespective to any other trigger, and the "exclusive" where only this trigger fires. The BBCLL1 trigger was found to be almost free from any other events besides inelastic ion-ion collisions.

The second trigger in the data sample was the ZDC trigger, requiring a coincidence of the North and South sides of the ZDC with a minimum energy deposition of 10 GeV in each. Although the ZDC is a small-area hadron calorimeter with relatively low resolution each spectator neutron carries the energy of $\sqrt{s_{NN}}/2$, well above the threshold. About 97% of the BBCLL1 triggers coincide with the ZDC triggers.
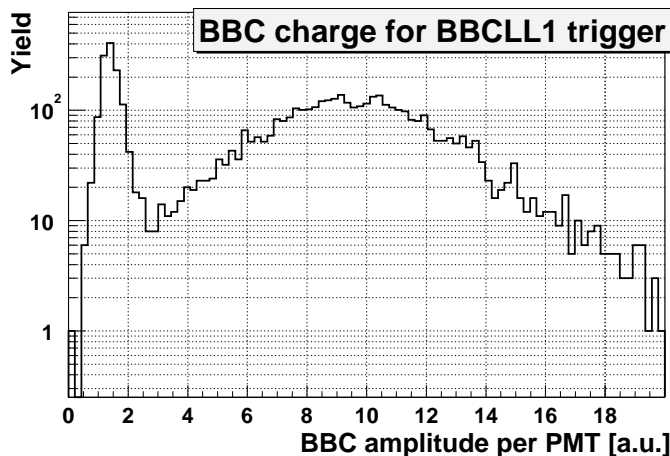
Figure 3.2: BBC charge divided by the number of fired channels. The lower peak is produced by the beam-gas collisions.

A fraction of $\sim 12\%$ of exclusive BBCLL1 triggers i.e. without ZDC trigger, in the

year-1 data sample originated from beam-gas interactions producing the lower peak shown in fig. 3.2. These events were discarded in the analysis.

The total number of events in the analysis were $\sim$135k and $\sim$60k in year-1 and year-2, respectively. Based on extensive simulations and on the BBC/ZDC trigger ratios the BBCLL1 trigger was associated with $92 \pm 2\%$ of the geometrical cross section at $\sqrt{s_{NN}}$ =130 GeV and $93 \pm 3\%$ at $\sqrt{s_{NN}}$ =200 GeV. An additional error of $1 \pm 1\%$ at $\sqrt{s_{NN}}$ =130 GeV accounts for contaminations in the trigger.

3.2   Raw distributions

The raw distributions of the variables playing an important role in the analysis are shown in this section. The BBC and ZDC signals from year-2 data are shown in fig. 3.3 for the BBCLL1 triggers. One finds that the exclusive BBCLL1 trigger contribution is in the
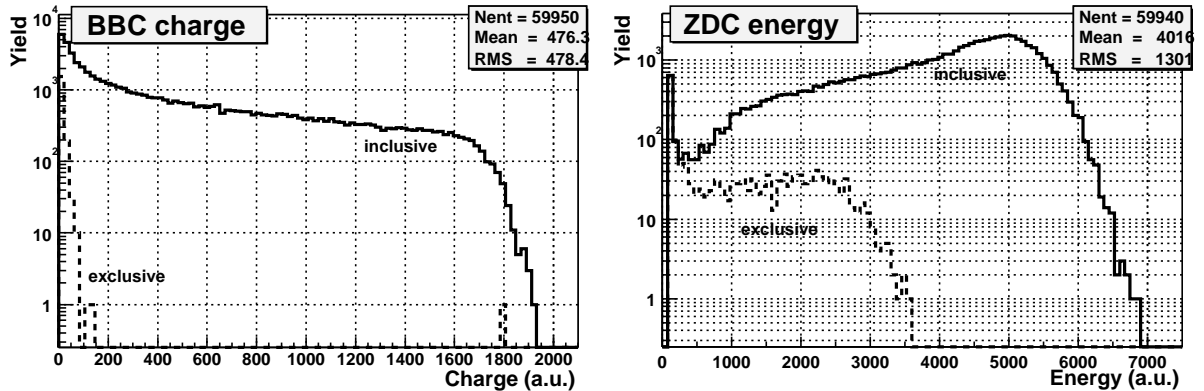
Figure 3.3: The BBC (left) and ZDC (right) signals distribution.

lowest part of the distributions, as expected (besides one central event at around 1800 in the left plot where ZDC did not produce a trigger). There is a finite probability that in the most central events in which N_p is close to $2A$ none of the spectator neutrons hits the ZDC. This effect was much more pronounced in the year-1 data due to different energy and emittance of the colliding beams.

One can also see in the right plot of fig. 3.3 that the ZDC may still have a signal in the case of an exclusive BBCLL1 trigger. This happens when the energy in one of the ZDC (North or South) is below the threshold of 10 GeV whereas the other ZDC detects a much larger energy.

The number of hits in the PC layers is shown in the left panel of fig 3.4. Both PC1 measure approximately the same number of hits. This number is higher than in PC3 due to the different location of the chambers and slightly different acceptances (see 2.1
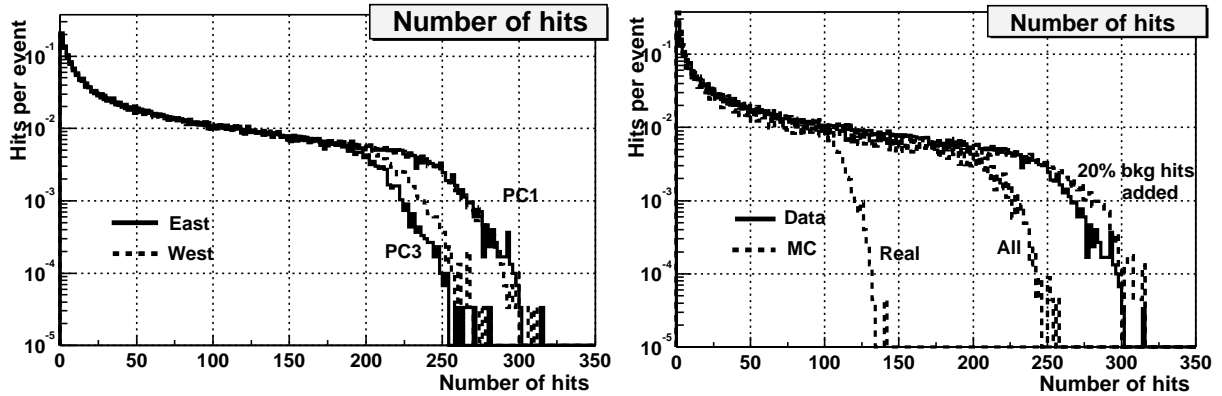
Figure 3.4: Number of hits in the various PC layers (left), comparison to simulation based on HIJING v.1.35 (right).

and section 2.3). The PC3 east also reconstructs less hits than PC3 West due to several inactive cards in the East arm. See sec. 3.5.1.

In the right panel of fig. 3.4 the number of hits in the East PC1 is compared to the number of hits obtained from the full detector simulation [45] using events produced by HIJING generator [13]. One should note that approximately half of the simulated hits are not originating from the event vertex but are scattered from the detector albedo. The total number of hits in the simulation is lower than in the data. In order to better match the Monte Carlo simulations to the data the number of background hits was increased by $\sim$20%. The added background hits are crucial to study multiplicity dependent effects under conditions similar to those in the data.

3.3 Event vertex reconstruction

The two layers of the PCs are used for the event vertex reconstruction in the following way: all hits in PC3 are combined with all hits in PC1 and the resulting lines are projected onto a plane through the beam line, perpendicular to the symmetry axis of the chambers as seen in fig. 3.5. For events with more than $\sim$5 tracks (about 60% of BBCLL1 trigger events), the distribution of these projections along the Z axis falling within 8 cm from the beam line produces a distinct peak which defines the vertex position as shown in fig. 3.6 (left).

The vertex reconstruction accuracy can be estimated by the width of the peak divided by the square root of the number of tracks under the peak. This distribution is shown in the right panel of fig. 3.6. The mean of the distribution is about 4 mm for all events for which the vertex is reconstructed. The tail of the distribution is mainly due to the
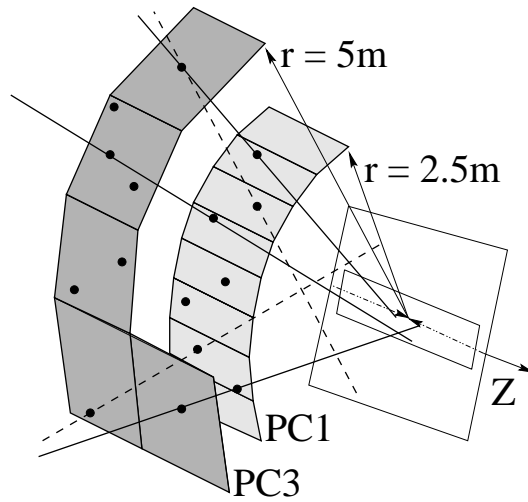
Figure 3.5: The pad chamber geometry of one central arm. Some PC3 sectors are removed for clarity. The track candidates (the straight lines through a pair of PC1 and PC3 hits) pointing to the window are accepted in the analysis.
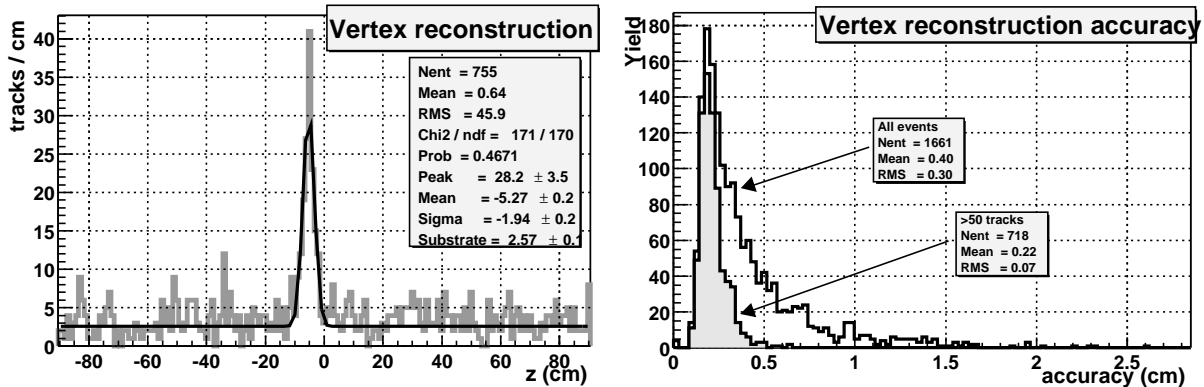
Figure 3.6: An example of vertex reconstruction using the PCs from an event with a total number of 755 tracks in both arms (left). Accuracy of the vertex reconstruction (right) for all events and for events with more than 50 tracks.

events with a low number of tracks. Selecting events with ∼50 or more valid tracks (filled histogram) makes the distribution much sharper and removes the tail. For such events the vertex is reconstructed with ∼2 mm accuracy.

The PC reconstructed vertex is in good agreement with the vertex reconstructed from the time difference between north and south BBC as shown in fig. 3.7. The small offset between PC and BBC is due to misalignment and can easily be corrected for. The width of the distribution has comparable contributions from the vertex finding accuracy of both PC (see fig. 3.6) and the BBC. For low multiplicity events where the number of tracks is too small to allow vertex determination by the PC, the vertex is taken from the BBC.
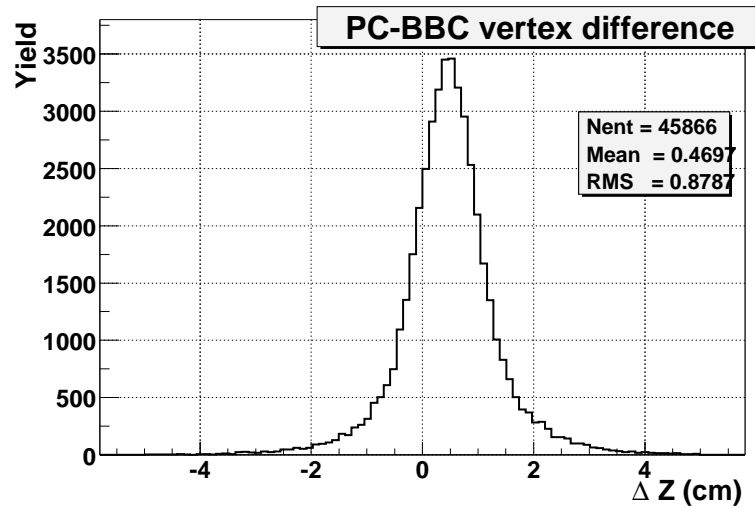
Figure 3.7: Difference of the vertex position reconstructed by the PC and the BBC.

3.4 Track projection distribution and background subtraction

Once the the vertex is known, all hits in PC3 are again combined to all hits in PC1 and the resulting tracks are projected onto the plane previously defined as shown in fig 3.5. The distribution of the distance R of the intersection points to the event vertex position is shown in fig. 3.8 for the data (left) and for the simulations (right). The vertical scale shows the absolute number of tracks per event and per cm. There is a good agreement between the two distributions. The figure also shows the two components of tracks con-
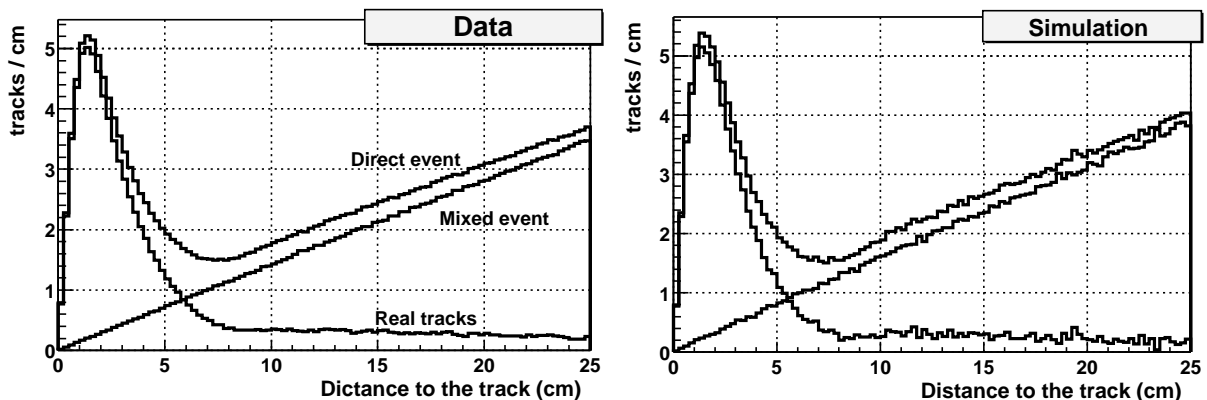
Figure 3.8: Distance from event vertex to the track intersection point. Data is in the left left panel and simulation in the right.

tributing to the total distribution:

– the combinatorial background contribution which is inherent to the algorithm used. It can be easily determined by an event mixing technique. In this analysis, the background was determined by exchanging each sector in PC1 with its neighbor. The yield of the background increases quadratically with R (leading to a linear dependence in the differential dN/dR vs. R presentation of fig. 3.8)[2].

– the real tracks contribution which can be readily obtained by subtracting the background from the total. One observes a sharp peak at small R – these are primary particles originating at the vertex – and a long tail due to decay products of primary particles decaying in flight.

The tail is very well described by an exponential function and therefore the extrapolation of the "Real" curve to $R = \infty$ is straightforward. In practice the track counting is performed up to a given R value. The fraction of counted tracks as a function of R is obtained from the extrapolation of the distribution to $R = \infty$. In the present analysis the track counting is done up to $R = 25$ cm, including 95.5% of all tracks.

The combinatorial background can be determined and subtracted event-by-event. However, this would introduce an unnecessary broadening of the real multiplicity distribution. In order to avoid that the average number of background tracks is determined (shown by the line in fig 3.9) for each number of direct tracks in the event, using a mixed
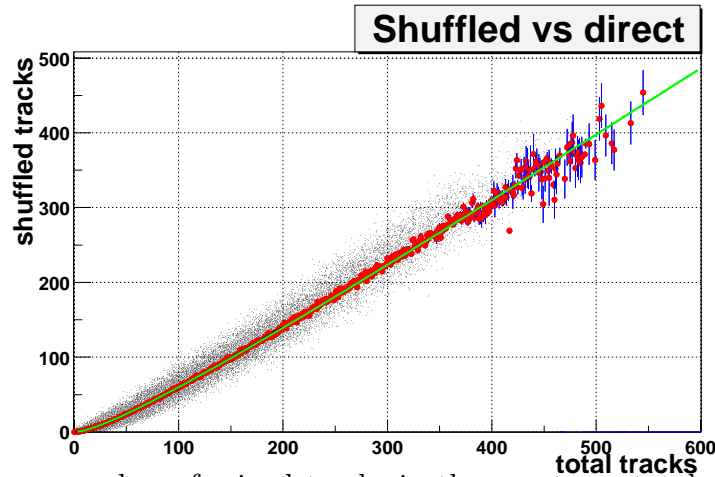
Figure 3.9: Average number of mixed tracks in the event vs. total number of tracks in the event.

event technique and then subtracted from the total. The subtraction of the average

---

[2]Other event mixing techniques were also used as cross check. The four top PC1 were interchanged with the four bottom PC1, and the two arm of PC1 were swapped. All methods give the same results. In the simulation the event mixing technique reproduces the combinatorial background with an accuracy better than 1%.

background gives a much better result that the direct subtraction of the background in a given event because it eliminates the fluctuations.

3.5 Corrections

After subtracting the background several corrections need to be implemented in order to derive the distribution of the primary charged particles.

3.5.1 Scaling factor corrections

Several scaling factor corrections have to be applied: inactive gaps between the chambers, inactive electronic readout cards and dead pads in PC1 and PC3 detectors, tracks falling outside the acceptance (discussed in sec. 3.4) and chamber inefficiency. These factors are easily obtained and are given in Table. 3.1.

Table 3.1: Scaling correction factors

Layer	PC1 East	PC1 West	PC3 East	PC3 West
Inactive ROCs	0.9%±0.2%	0.5%±0.2%	6%±1.0%	0.7%±0.2%
Inactive TGLs	0.6%±0.2%		0.3%±0.2%	
Dead area by construction	0.7%±0.2%		6.6%±0.5%	
Inefficiency	0.6%±0.5%		0.3%±0.5%	
Tracks outside R acceptance	4.1% ±1.5%			

The track acceptance of PC1/3 is not exactly given by the solid angle coverage of the chambers because some tracks entering or leaving PC1 or PC3 at the edges of the acceptance can miss the other PC. It was determined from the data that the track acceptance of PC1/3 of one arm is $\eta = \pm 0.35$ and $\Delta\phi = 88.4^o$. Therefore the scaling factor for one unit of pseudorapidity with 2π azimuthal coverage is 5.82 for one arm and 2.91 for two arms.

3.5.2 Double hit resolution correction

The Double Hit Resolution (DHR) discussed in sec. 2.7 has a significant impact on the number of reconstructed tracks. Because of the significance of this effect an exact knowledge of the DHR area is essential for the analysis. As shown in sec. 2.7 and from the data (see fig. 2.18) the estimated DHR of the PC1 is close to 4 cm. In the analysis and in the simulation hits closer than 4 cm in PC1 were merged into one hit. For PC3

the corresponding value is 8 cm. This makes the DHR value to be very well defined and also effectively removes all fake hits discussed in sec. 2.7.5.

The DHR affects the track counting in two different ways.

DHR effect on hit and track losses

The first effect is proportional to the number of measured hits N_m in both PC1 and PC3. N_m can be calculated from the original number of hits before merging N and the ratio of the merging area πr^2 (where r is the DHR radius) to the total area of the detector S:

$$f = \frac{N_m}{N} = 1 - \frac{N-1}{2} \times \frac{\pi r^2}{S} \tag{3.1}$$

Figure 3.10 shows the simulation results for PC1 and PC3 where the fraction of hits surviving merging $f = N_m/N$ is plotted against N. It is assumed that two hits closer
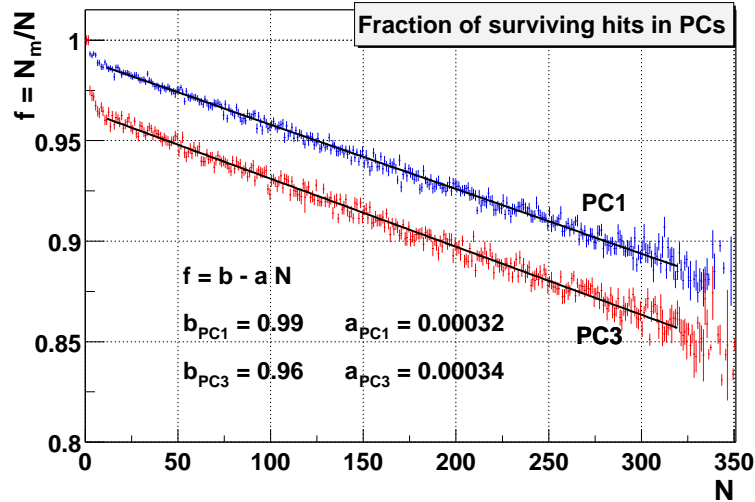
Figure 3.10: Average number of mixed tracks in the event vs. total number of tracks in the event.

than $r = 4$ cm in PC1 and $r = 8$ cm in PC3 merge together. One can see that the fraction of hits lost is proportional to the original number of hits as expected from eq. 3.1. The points can be fitted with a linear function $f = b - aN$. For $N = 0$, f is not equal to 1 due to the contribution of electron pairs from γ-conversions in the sample (bigger in PC3 than in PC1 due to the extra material in front of PC3) with a very small opening angle such that they merge into one hit independently of the overall chamber occupancy. The coefficient a is the occupancy factor and can be estimated from $r = 4$ cm and Table 2.1 to be ~ 0.00036 according to eq. 3.1. The fit gives a slightly smaller number due to edge

effects, since when a hit is close to the chamber edges the merging area is smaller than πr^2.

Using the fitted values shown in fig. 3.10 one can calculate the total number of hits N in the event from the measured N_m number of hits in the chambers and calculated fractions of f_1 and f_3 survived the merging in PC1 and PC3 respectively. The number of tracks reconstructed in the event is then scaled up by the factor $1/f_1 f_3$. The validity of this approach was corroborated by the Monte Carlo simulations. This correction depends on multiplicity and it amounts to a $\sim 15\%$ correction for the 5% most central events.

DHR effect on the background subtraction

The second effect caused by finite DHR of the chambers, results in a difference between the number of combinatorial background tracks in the direct event and the number of tracks reconstructed in the mixed event. In order to explain this effect one needs to introduce some definitions. Let us call a **"real"** hit a hit produced by a particle coming directly from the event vertex and a **"background"** hit a hit produced by any other particle (e.g. rescattered from the detector albedo). Then the combinatorial background in the detector can be divided into tree different categories. **"Background-background" (BB)** track when both hits in PC1 and PC3 are background hits, **BR** when one hit is a **background** and the other is **real** and **RR** when both are **real** hits but from different particles.

Figure 3.11 A shows a **BR** track with a **real** hit in PC1 (full circle) and a **background** hit in PC3 (open circle). It is clear that in the vicinity of the PC3 hit there is a hit from
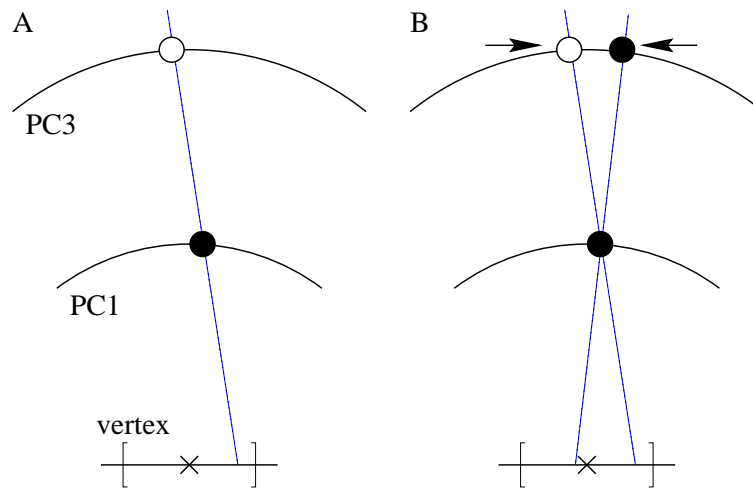
Figure 3.11: Left panel shows a combinatorial background track of a **background-real** type with a **background** hit in PC3 (hollow circle) and **real** hit in PC1 (full circle). Another **real** hit should be detected in PC3 for this type of track as shown in the right panel.

the same **real** particle, detected in PC1 (fig. 3.11 B), and those two hits may merge leading to a track loss. In the mixed event all real tracks are destroyed (by mixing) and therefore the prediction of the second hit in PC3 is not anymore valid. This effect occurs also for **RR** types of tracks and does not occur for **BB** as it is clear from its nature.

This effect was studied using a toy-model simulation as well as by extensive full scale Monte-Carlo. Figure 3.12 shows the result of the simulation. One can see a significant
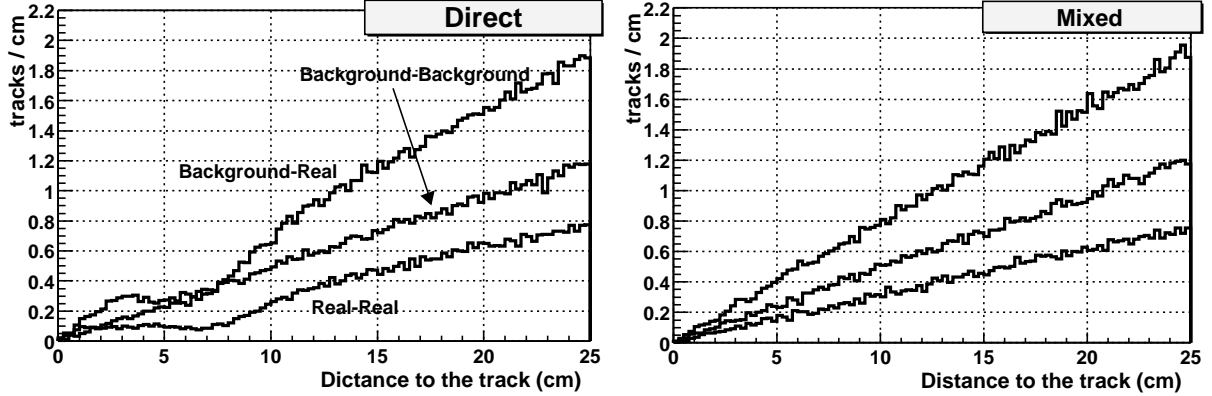
Figure 3.12: Combinatorial (left) and Mixed (right) background. A deficit area can be seen in the Direct event in **RR** and **BR** tracks around R=6 cm

deficit of tracks at radius around $R = 6$ cm for **RR** and **BR** types of combinatorial background. This is not seen in the Mixed event, as expected. To calculate the magnitude of this effect one can assume that the ratio between *Real* and *Total* number of hits in the event is independent of multiplicity. This is verified by the Mone Carlo studies and cross checked by the results obtained later. Under this assumption the ratio of combinatorial background tracks in the direct event and in the Mixed event is given by the relation:

$$\frac{Combinatorial}{Mixed} = 1 - 4 \times \frac{Real}{Total} \left(\frac{r}{R}\right)^2 \tag{3.2}$$

where r and R are the radii of the DHR and acceptance window (25 cm) respectively. This formula includes the number of *Real* hits in the event which is the ultimate target of the whole analysis. As already mentioned, the simulations show that the ratio Real/Total is constant and based on both simulation and data it was found that $Combinatorial = 0.964 \times Mixed$.

3.5.3 In-flight decay correction, year-1 approach

A large fraction of the in-flight decay of particles is detected and counted with our procedure as illustrated in fig. 3.8. However, a small fraction still remains unaccounted

for. On the other hand, there are decays of neutral particles leading to charged tracks. Those two effects have to be taken into account. Clearly the quantitative evaluation depends on the particle composition and on their momentum distribution. Lacking precise information about them during the year-1 analysis, a detailed study using Monte Carlo simulations was done, by comparing the HIJING charged particle multiplicity in the East arm acceptance to the full detector simulation (PISA[3] [45]) results, processed in exactly the same way as in the data analysis. It was found that the missed tracks due to charged particle decays in flight are to a large extent compensated by the decay of neutral particles (mainly π^o and K_S^o). The comparison is shown in Table 3.2

Table 3.2: Particle composition per minimum bias event in the acceptance of one arm for Au-Au collisions at $\sqrt{s_{NN}}$ =130 GeV.

Valid track parent particle	Detected charged tracks			Generated by HIJING
	Primary	Decay	Total	
$\pi^+\pi^-$	12.66	3.56	16.22	20.33
p^+p^-	0.69	0.12	0.80	0.92
K^+K^-	0.49	0.39	0.89	1.84
e^+e^-	0.02		0.02	0.02
Others ($\Sigma^\pm, \bar{\Sigma}^\pm, \Xi^\pm...$)		0.21	0.21	0.17
Charged	13.86	4.28	18.14	**23.28**
π^0		0.69	0.69	11.37
γ		0.06	0.06	2.26
$n, \bar{n}$		0.06	0.06	0.92
K_L^o		0.07	0.07	0.90
K_S^o		1.23	1.23	0.90
Others ($\Lambda, \Xi^o, \Sigma^o...$)		0.33	0.33	0.33
Neutral		2.44	2.44	16.67
Total	13.86	6.71	**20.57**	39.95
Corrected (*)			**22.63**	

(*) for contributions in $R > 25$ and design dead areas

The total number of charged particles given by HIJING in one arm acceptance is 23.28 per minimum bias collision. The total number of detected charged tracks according to PISA is 20.57. The latter becomes 22.63 after correcting for the tracks outside the $R = 25$ cm cut and the construction dead areas as included in the simulation, thereby resulting in a net loss of 2.8% in the simulation result wrt the HIJING input.

---

[3]PHENIX Integrated Simulation Application

In order to estimate the uncertainty associated with the correction a variation of the input momentum distribution and the particle composition was done within $\pm 20\%$ of the HIJING values. From the induced changes one can assigned a systematic error of less than 4% to the in-flight decay correction.

3.5.4 In-flight decay correction, year-2 approach

The in-flight correction as described above and published in [32] depends on three major values. The particle composition in the event, the momentum of the particles, and their rapidity distribution. The particle composition is the most important ingredient because particles of different species i have different detection efficiency ε_i. The momentum may also modify the detection effciency ε_i, but it is less important than the composition, and finally, the rapidity distribution is the least important factor. The rapidity distribution enters into the correction when the product of particle decays from other rapidities are detected in the PHENIX acceptance as a valid track. This effect is largely suppressed by the analysis procedure as can be seen in fig. 3.13. The total flow of particles from outside the PHENIX acceptance of $|\eta| < 0.35$ is estimated to be 8.5% and this flow is coming primarily from the closest rapidities as shown in the figure. Due to the fact that the rapidity distribution of the particles is flat around zero the HIJING generator reproduces the amount of flow correctly.
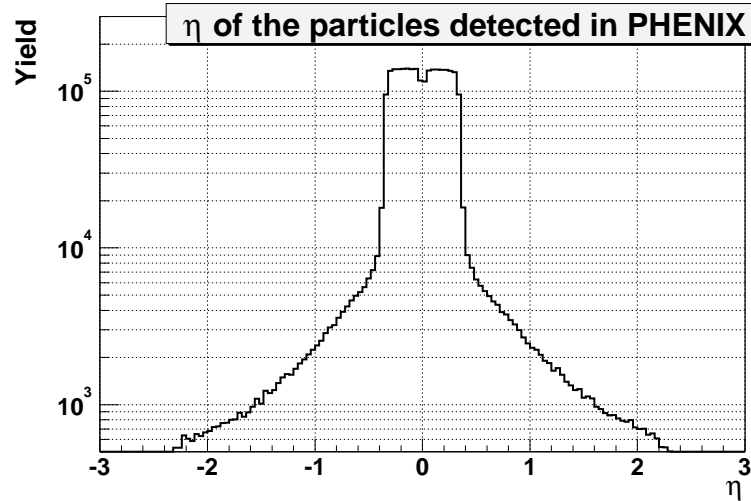
Figure 3.13: Pseudorapidity distribution of the primary particles detected in the PHENIX Central Arms using the PC1/PC3 analysis procedure, from simulation. The tails are due to primary particle decays.

Measured Data

As previousely mentiond the in-flight decay corrections for the analysis of year-1 data published in [32] was based on the HIJING particle composition. For year-2 having the advantage of information gathered in year-1 the in-flight correction was refined. It was calculated using HIJING at $\sqrt{s_{NN}} = 200$GeV, but the particle composition and the average momentum $\langle p_T \rangle$ were corrected according to the measurements done in year-1.

The information on the particle production and mean transverse momentum measured by PHENIX and STAR in year-1 is summarized in Table 3.3. The absolute yields are

Table 3.3: Particle composition and average momentum in Au-Au collisions at $\sqrt{s_{NN}}$ =130 GeV for the 5% most central events from STAR and PHENIX experiments. The first error is always statistical, the second is systematic.

Experiment	PHENIX		STAR	
References	[46]		[47, 48, 49]	
Value	dN/dy	$\langle p_T \rangle$ [GeV/c]	dN/dy	$\langle p_T \rangle$ [GeV/c]
π^+	$276 \pm 3 \pm 36$	$0.387 \pm .005 \pm .022$		
π^-	$270 \pm 3 \pm 35$	$0.381 \pm .005 \pm .022$	200	
π^-/π^+			(from K^-/π^-)	
K^+	$46.7 \pm 1.5 \pm 7$	$0.560 \pm .027 \pm .053$	$35 \pm 3 \pm 5$	
K^-	$40.5 \pm 2.3 \pm 6$	$0.575 \pm .033 \pm .053$	$30 \pm 3 \pm 4$	
K^-/K^+				
p	$28.7 \pm 0.9 \pm 4$	$0.882 \pm .03 \pm .093$		
$\bar{p}$	$20.1 \pm 1.0 \pm 3$	$0.898 \pm .044 \pm .081$	$20.53 \pm 0.5 \pm 4$	
$\bar{p}/p$			$0.65 \pm 0.01 \pm 0.07$	
Λ		$1.0 \pm .. \pm .2$	18.6 ± 0.7	
$\overline{\Lambda}$		$1.0 \pm .. \pm .2$	12.9 ± 0.5	
$\overline{\Lambda}/\Lambda$		Min.Bias data		
Ξ			3.07 ± 0.13	
$\overline{\Xi}$			2.63 ± 0.12	
$\overline{\Xi}/\Xi$				
h^-				$0.508 \pm .012$

not always consistent between the two experiments, for example, for kaons. The particle ratios (X^-/X^+) are in good agreement and are the same as measured by PHOBOS in [50]. For the correction, the PHENIX data is used first, and STAR data when PHENIX measurement is absent. The numbers published for $p\bar{p}$ by PHENIX and STAR include the contributions from weak decays. PHENIX estimates this contribution to be less than 24%. The latter number is used to calculate the net proton production. Thus, the net

yield of p and $\bar{p}$ for PHENIX is 21.8 and 15.3 respectively.

Correction using measured particle composition

The procedure to calculate the new in-flight correction is described below. All relevant numbers are shown in Table 3.4.

· The HIJING particle generator is used to generate a sample of 5% most central collisions (without jet quenching mechanism) at $\sqrt{s_{NN}} = 200$GeV. Column **"HIJING"** shows the HIJING yields dN/dy and $dN/d\eta$. The rapidity density distribution normalized to the rapidity density of negative pions is also shown.

· The simulated yields in one PHENIX central arm scaled to one unit of pseudorapidity for each type of particles and particle detection efficiency ε are shown in column (**"PISA"** in Table 3.4).

· The particle composition measured at $\sqrt{s_{NN}} =130$ GeV (taken from Table 3.3) and scaled by the yield of π^- are shown in the column **"DATA"** and are used to derive scaling factors f_i defined by:

$$f_i = \frac{(dN_i/dy^{DT})/(dN_{\pi^-}/dy^{DT})}{(dN_i/dy^{HJ})/(dN_{\pi^-}/dy^{HJ})} \tag{3.3}$$

The formula to calculate the correction for in-flight decays is:

$$Scaling = \frac{\sum_i |z_i| f_i \cdot dN_i/d\eta^{HJ}}{\sum_i f_i \cdot dN_i/d\eta^{PS}} \tag{3.4}$$

where the index i runs through all particle types, $|z_i|$ is the absolute value of the i-th particle charge and indices "DT", "HJ" and "PS" are for measured data, HIJING and PISA particle yields at midrapidity respectively.

With this procedure the correction is found to be -1.37%. This represents a relative change of 3.6% with respect to the correction of +2.28% calculated with year-1 procedure. The biggest contribution to this change comes from the strange particles like K_s and Λ's. Those neutral particles have very high detection efficiency because they decay into two charged particles which can be detected. In the year-1 analysis a systematic error of 4% was assigned to the in-flight correction calculation because of this reason, see [32].

Table 3.4: Particle yields in HIJING, PISA and Data. ε is the detection efficiency, f is a correction factor given by eq. 3.3

| Particle | | HIJING | | | PISA | | Data | | | Com- |
ID	type	$\frac{dN}{dy}$	$\frac{dN/dy}{dN_{\pi^-}/dy}$	$\frac{dN}{d\eta}$	$\frac{dN}{d\eta}$	ε	$\frac{dN}{dy}$	$\frac{dN/dy}{dN_{\pi^-}/dy}$	f	ment
1	γ	72.32	0.190	72.32	1.821	0.025	n/a	n/a	1	
2	e^+	0.379	0.001	0.379	0.335	0.882	n/a	n/a	1	
3	e^-	0.370	0.001	0.369	0.332	0.899	n/a	n/a	1	
4	ν	0.183	0.000	0.081	0.000	0.000	n/a	n/a	1	
5	μ^+	0.002	0.000	0.001	0.003	~ 1	n/a	n/a	1	
6	μ^-	0.002	0.000	0.002	0.003	~ 1	n/a	n/a	1	
7	π^0	433.8	1.137	365.6	23.45	0.064	n/a	n/a	1	
8	π^+	379.5	0.995	325.4	287.2	0.883	276	1.02	1.03	
9	π^-	381.5	1.000	326.8	287.0	0.878	270	unit	1.00	
10	K_l^0	46.67	0.122	29.40	2.582	0.088	est	0.161	1.32	$\frac{K^++K^-}{2}$
11	K^+	49.42	0.130	31.20	16.02	0.514	46.7	0.173	1.33	
12	K^-	45.76	0.120	28.59	14.62	0.511	40.5	0.150	1.25	
13	n	32.27	0.085	16.20	0.157	0.010	est	0.081	0.95	as p
14	p	31.91	0.084	16.08	13.76	0.856	21.8	0.081	0.96	
15	$\bar{p}$	27.45	0.072	13.43	17.62	1.313	15.3	0.057	0.79	
16	K_s^0	46.39	0.122	29.08	44.14	1.518	est	0.161	1.32	$\frac{K^++K^-}{2}$
17	η									
18	Λ	7.802	0.020	3.640	3.780	1.039	18.6	0.069	3.36	
19	Σ^+	2.752	0.007	1.283	1.298	1.012	n/a	n/a	1	import.
20	Σ^0	2.777	0.007	1.279	1.336	1.044	n/a	n/a	1	import.
21	Σ^-	2.760	0.007	1.230	1.493	1.213	n/a	n/a	1	import.
22	Ξ^0	0.889	0.002	0.383	0.398	1.038	est	0.01	4.9	as Ξ^-
23	Ξ^-	0.850	0.002	0.358	0.693	1.933	3.07	0.01	4.9	
24	Ω	0.017	0.000	0.005	0.015	2.656	n/a	n/a	1	
25	$\bar{n}$	27.39	0.072	13.64	1.636	0.120	est	0.057	0.79	as $\bar{p}$
26	$\overline{\Lambda}$	7.162	0.019	3.239	4.559	1.408	12.9	0.048	2.54	
27	$\overline{\Sigma}^-$	2.502	0.007	1.128	1.608	1.426	n/a	n/a	1	import.
28	$\overline{\Sigma}^0$	2.616	0.007	1.182	1.702	1.440	n/a	n/a	1	import.
29	$\overline{\Sigma}^+$	2.544	0.007	1.089	1.559	1.432	n/a	n/a	1	import.
30	$\overline{\Xi}^0$	0.909	0.002	0.391	0.580	1.486	est	0.011	4.0	as $\overline{\Xi}^+$
31	$\overline{\Xi}^+$	0.893	0.002	0.390	0.947	2.429	2.63	0.011	4.0	
32	$\overline{\Omega}^+$	0.014	0.000	0.006	0.008	1.328	n/a	n/a	1	
Correct.		748 vs.731 = +2.28%							-1.32%	

Correction using measured average particle momentum

The correction factor calculated above takes into account only the measured particle yields. However, as it was mentioned, the particle detection efficiency ε of each type of particles depends on the momentum distribution. To take this into account, a procedure, similar to that one used above is implemented:

· The particle detection efficiency $\varepsilon(p)$ was determined for each type of particles as a function of the total momentum p using simulation.

· The measured $\langle p_T \rangle$ for pions, kaons and protons was compared with the average $\langle p_T \rangle$ of HIJING to determine "boost" coefficients.

· The initial HIJING momentum distributions were boosted using these coefficients and the resulting distribution multiplied by $\varepsilon(p)$. The new average detection efficiency $\langle \varepsilon(p) \rangle$ was determined for each type. The p is used instead of p_T as a more adequate parameter for the fraction of particles coming from high rapidities (see fig. 3.13).

· The new correction is calculated using the new average detection efficiency.

Table 3.5 explains how the correction is calculated. The first three columns show the $dN/d\eta$ (corrected for the particle ratio), $\langle p_T \rangle$ of HIJING and the average detection efficiency $\langle \varepsilon(p) \rangle$ calculated using PISA. The measured $\langle p_T \rangle$ and the "boost" coefficients are shown in the two next columns. Using the coefficients one can calculate the new value of the average efficiency $\langle \varepsilon(p) \rangle$, also shown. The next columns shows the difference in the number of particles ΔN calculated assuming the new and the old values of $\langle \varepsilon(p) \rangle$.

As one can see the resulting correction is almost equal to zero. The correction due to $\langle p_T \rangle$ is not as strong as due to particle composition, as expected, and it primarily comes from the contribution of the most abundant particles (pions) which have less $\langle p_T \rangle$ than in HIJING. Since pions partially decay in flight (see Table 3.2) before they reach PC3 the smaller $\langle p_T \rangle$ results in more decays and require a stronger correction.

Table 3.5: Particle $\langle p_T \rangle$ in HIJING and Data. ε is the detection efficiency before and after the correction for the measured $\langle p_T \rangle$.

Particle		HIJING			Data			
ID	type	$dN/d\eta$	$\langle p_T \rangle$	$\langle \varepsilon(p) \rangle$	$\langle p_T \rangle$	boost	new $\langle \varepsilon(p) \rangle$	ΔN
1	γ	72.32	0.328	0.025	n/a	1	0.025	
2	e^+	0.379	0.174	0.882	n/a	1	0.882	
3	e^-	0.369	0.165	0.899	n/a	1	0.899	
4	ν	0.081	1.568		n/a	1		
5	μ^+	0.001	0.449	~ 1	n/a	1	~ 1	
6	μ^-	0.002	0.311	~ 1	n/a	1	~ 1	
7	π^0	365.6	0.393	0.064	n/a	0.93	0.063	-0.456
8	π^+	328.6	0.416	0.883	0.387	0.92	0.865	-5.683
9	π^-	326.8	0.416	0.878	0.381	0.92	0.861	-5.644
10	K_l^0	38.81	0.587	0.088	n/a	0.97	0.088	
11	K^+	41.49	0.590	0.514	0.560	0.95	0.507	-0.279
12	K^-	35.74	0.578	0.511	0.575	0.99	0.511	
13	n	15.39	0.768	0.010	n/a	1.14	0.010	
14	p	15.44	0.771	0.856	0.882	1.14	0.880	0.379
15	$\bar{p}$	10.61	0.733	1.313	0.898	1.23	1.317	0.051
16	K_s^0	38.38	0.587	1.518	n/a	0.97	1.515	0.129
17	η							
18	Λ	12.23	0.801	1.039	1.0	1.24	1.039	0.0
19	Σ^+	1.283	0.846	1.012	n/a	1	1.012	
20	Σ^0	1.279	0.852	1.044	n/a	1	1.044	
21	Σ^-	1.230	0.844	1.213	n/a	1	1.213	
22	Ξ^0	1.878	0.846	1.038	n/a	1	1.038	
23	Ξ^-	1.756	0.841	1.933	n/a	1	1.933	
24	Ω	0.005	1.015	2.656	n/a	1	2.656	
25	$\bar{n}$	10.77	0.729	0.120	n/a	1.23	0.120	0.0
26	$\bar{\Lambda}$	8.227	0.782	1.408	1.0	1.27	1.408	0.0
27	$\overline{\Sigma}^-$	1.128	0.814	1.426	n/a	1	1.426	
28	$\overline{\Sigma}^0$	1.182	0.803	1.440	n/a	1	1.440	
29	$\overline{\Sigma}^+$	1.089	0.816	1.432	n/a	1	1.432	
30	$\overline{\Xi}^0$	1.563	0.854	1.486	n/a	1	1.486	
31	$\overline{\Xi}^+$	1.559	0.854	2.429	n/a	1	2.429	
32	$\overline{\Omega}^+$	0.006	0.902	1.328	n/a	1	1.328	
Correct.				-1.32%				+0.24%

Estimation of errors

The error estimate in the in-flight correction was done by varying the particle yields within the statistical and systematic errors of the measured values by PHENIX shown in Table 3.3 using the following procedure. For a particle and its antiparticle the variation was done

Table 3.6: Results of the variation of the input values

	Particle	Parameter	Positive	Negative	Error
1	$\pi^\pm$	yield	+1.692%	-1.590%	±1.6%
2	$K^\pm$	yield	-0.353%	0.771%	±0.6%
3	$p\bar{p}$	yield	0.175%	-0.321%	±0.1%
4	$\Lambda\bar{\Lambda}$	yield	-0.375%	0.789%	±0.6%
	subtotal	yield		±1.8%	
5	$\pi^\pm$	$\langle p_T \rangle$	-0.963%	1.532%	±1.2%
6	$K^\pm$	$\langle p_T \rangle$	-0.230%	0.699%	±0.5%
7	$p\bar{p}$	$\langle p_T \rangle$	0.193%	0.327%	±0.1%
	subtotal	$\langle p_T \rangle$		±1.3%	
Total					±2.2%

simultaneously by the value equal to the direct sum of the statistical and systematic errors. For example, the yield of π^+ and π^- was increased from $276 \rightarrow 315$ and $270 \rightarrow 308$, respectively. The correction obtained under these conditions is shown in Table 3.6 in column "Positive". The result of the negative variation is shown in the next column. The column "Error" shows the absolute average of the two variations with respect to the nominal value of the correction in Table 3.5.

Assuming the particle yields as published by the STAR experiment the correction agrees to the PHENIX values within systematic errors. Assuming the average $\langle p_T \rangle$ published by STAR the deviation is larger than the systematic error, however the STAR published [51] only mean $\langle p_T \rangle$ for h^- whereas the correction is based on $\langle p_T \rangle$ measured for all species separately.

The inclusive particle production yields for $\pi^\pm$, $K^\pm$ and $p^\pm$ presented in Table 3.3 include the feed-down from other particles. PHENIX experiment estimates the feed-down from the strange baryons into proton yield to be less than 24% [46] and STAR at approximately 50% [49]. One can assume that measured yields for $\pi^\pm$ and $K^\pm$ also have contributions form other primary particles. To understand the contribution of different particles into measured inclusive yields one can use simulations.

Table 3.7 shows the primary particles and their charged decay products at the PC3 location. The bottom line in the table shows the amount of particles of a given type,

originating from other primary particles. These can be compared to the total yields (third column in Table 3.7). The amount of $K^\pm$ coming from other primary particles is negligible. For $\pi^\pm$ the amount is ~9% i.e. smaller than the systematic errors of the measurements presented in Table 3.3.

The error obtained in this procedure is 2.2% for the most central events. This correction depends on centrality, because the particle yields change with centrality. However, for the relevant range $N_p > 50$ the particle ratios and $\langle p_T \rangle$ do not change much. In order to take into account the centrality dependence the error is increased by 0.8%, which is approximately equal twice the difference between corrections obtained with the most central and minimum bias yield and $\langle p_T \rangle$ data sets. The resulting correction of 3% is taken centrality independent.

Table 3.7: Original particles and particles detected at PC3 location

Original part.			Detected particle									
ID	type	total	e^+	e^-	μ^+	μ^-	π^+	π^-	K^+	K^-	p	$\overline{p}$
1	γ	1.82	0.86	0.96								
2	e^+	0.33	0.33	0.01								
3	e^-	0.33		0.33								
4	ν											
5	μ^+											
6	μ^-											
7	π^0	23.45	10.98	12.47								
8	π^+	287.2	1.77	1.88	55.94	0.15	224.4	0.39	0.01		2.65	
9	π^-	287.0	1.05	3.32	0.12	55.83	0.37	225.3			1.06	
10	K^0_l	2.58	0.34	0.36	0.38	0.36	0.52	0.52	0.01		0.09	
11	K^+	16.02	0.46	0.21	4.71	0.08	1.66	0.30	8.48		0.13	
12	K^-	14.62	0.15	0.50	0.08	4.28	0.31	1.74		7.43	0.13	
13	n	0.16	0.01	0.01	0.01	0.02	0.02	0.03			0.06	
14	p	13.76	0.01	0.05	0.03	0.01	0.05	0.02			13.60	
15	$\overline{p}$	17.62	1.10	1.63	0.25	0.35	1.41	2.15			0.38	10.35
16	K^0_s	44.14	0.85	1.12	4.61	4.55	16.34	16.38			0.27	
17	η											
18	Λ	3.78	0.06	0.10		0.47	0.01	1.22			1.91	
19	Σ^+	1.30	0.04	0.04	0.17		0.53				0.52	
20	Σ^0	1.34	0.03	0.05		0.15		0.41			0.69	
21	Σ^-	1.49	0.01	0.02		0.36		1.10			0.01	
22	Ξ^0	0.40	0.02	0.02		0.05		0.13			0.18	
23	Ξ^-	0.69	0.01	0.02		0.14		0.36			0.17	
24	Ω	0.01						0.01				
25	$\overline{n}$	1.64	0.16	0.17	0.19	0.13	0.53	0.35			0.09	
26	$\overline{\Lambda}$	4.56	0.27	0.33	0.47	0.07	1.35	0.41			0.09	1.58
27	$\overline{\Sigma}^-$	1.61	0.09	0.14	0.02	0.19	0.10	0.59			0.02	0.46
28	$\overline{\Sigma}^0$	1.70	0.12	0.14	0.18	0.03	0.49	0.14			0.03	0.56
29	$\overline{\Sigma}^+$	1.56	0.02	0.03	0.38	0.01	1.06	0.04			0.02	
30	$\overline{\Xi}^0$	0.58	0.05	0.05	0.05	0.01	0.17	0.05			0.01	0.18
31	$\overline{\Xi}^+$	0.95	0.04	0.05	0.15	0.01	0.43	0.05			0.01	0.19
32	$\overline{\Omega}^+$	0.01										
from decays:			18.48	23.68	67.75	67.24	25.37	26.39	0.02	0.01	8.54	2.97

3.6 Cross-checks

Besides the cross checks done using full scale Monte-Carlo simulation based on HIJING and PISA at each step of this analysis, several other cross checks were performed. The most critical part, such as the DHR correction was cross checked with a toy-model simulation done independently at the Weizmann institute by the author and at Lund University by Dr. D.Silvermyr [52] giving the same results. Several other cross checks also done in the framework of the analysis are briefly described in this section.

DHR cross check

To verify the DHR correction the DHR radius r in the PCs was artificially increased by 50%. Any pair of hits closer than $r = 6$ cm in PC1 (compared to nominal $r = 4$ cm) and 12 cm in PC3 were merged increasing the dead area around any hit by a factor of 2.25 in each PC layer. For example, assuming that the total number of hits in PC1 is $N = 300$, the number of survived hits would decreased from $N_m = 268$ to $N_m = 228$ according to eq. 3.1. This dramatic change provides a powerful test of the whole analysis procedure. The DHR corrected multiplicity distributions for the two sets of DHR values are shown in fig. 3.14.
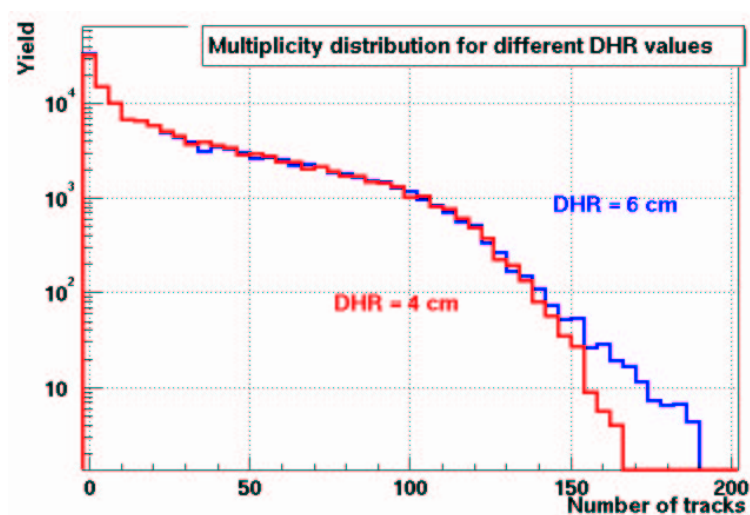
Figure 3.14: Comparison of the multiplicity distributions with different DHR parameters.

As one can see the two distribution coincide very well. The tail of the distribution with $r = 6$ cm is slightly longer, as expected, due to larger fluctuations.

Retracted position data

A limited statistics run at the beginning of year-1 was taken with the PHENIX central arms in a retracted position by 44 cm from the nominal setting and without magnetic field. Although these data were of a rather limited quality due to many "start-up" problems the PC data was analyzed and compared with the data taken in the nominal position. No difference was found between these two measurements, thus giving confidence in particular to the in-flight decay correction.

East arm vs. West arm

In year-2 the analysis was done independently for both arms. All corrections were determined based on the information from each arm independently and the results compared to each other. The charged multiplicity distribution in both arms is shown in the left panel in fig 3.15. The multiplicity distributions coincide very well and the
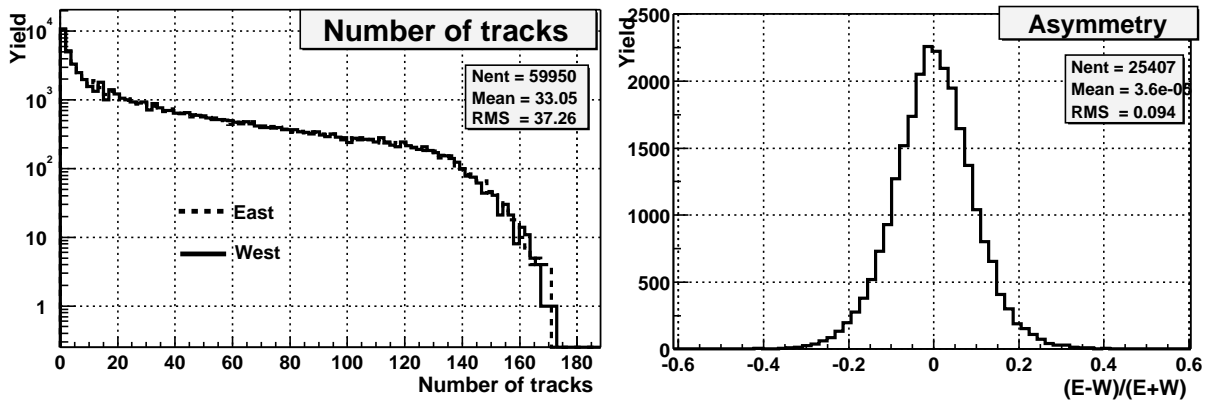
Figure 3.15: Comparison of the charged multiplicity distribution in the East and West arms in Au-Au collisions at $\sqrt{s_{NN}}$ =200 GeV (left) and the asymmetry of the two distributions $(East - West)/(East + West)$ for the events with more than 50 tracks (right).

asymmetry between the two values $(East - West)/(East + West)$ is close to zero.

3.7   Determination of centrality and number of participants

In order to study the particle density as a function of N_p, the ZDC vs BBC analog response was used to define centrality. The BBC vs ZDC response is shown in fig. 3.16.
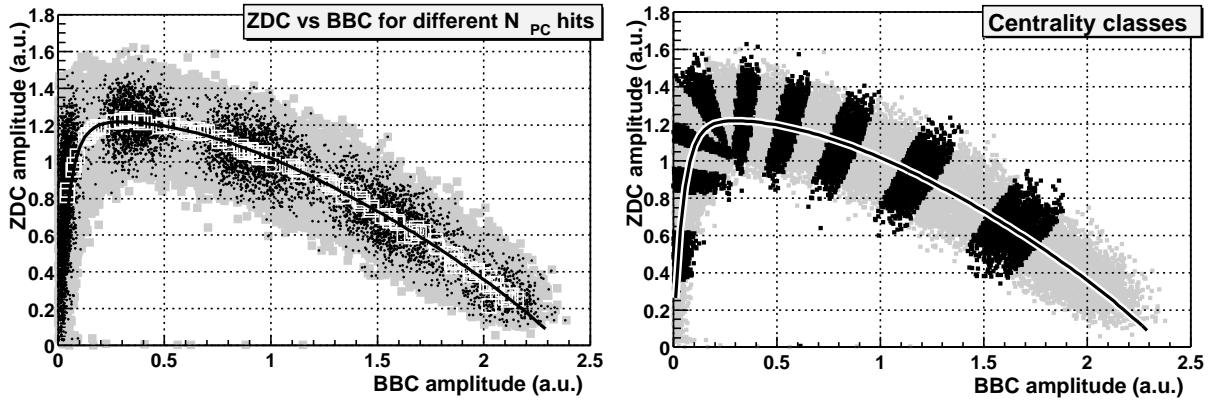
Figure 3.16: ZDC vs BBC analog response. Left: grey area shows all events, full points are events corresponding to a fixed number of hits in PC1, open squares are the mean values for fixed number of hits in PC1, and the solid line is a fit to them. Right: Centrality classes are shown in bin of 5%.

The left panel shows in grey a scatterplot of ZDC vs BBC amplitudes in some arbitrary units[4]. Several ZDC/BBC distributions each corresponding to a fixed number of hits in PC1 are superimposed on top (black points). The centroids of such distributions (open squares) are fitted by a solid line. Since the number of hits in the PCs is proportional to centrality the line represents the most probable centrality contour in the BBC/ZDC plot.

One can then integrate events along the centrality contour (each integration step is a slice between two perpendiculars to the contour) and map the centrality down peripheral collisions. Following this procedure one can define 10 centrality bins from 0-5%, 5-10%,... 45-50% of the total cross section. The distributions corresponding to 5% centrality bins are shown in the right panel of fig. 3.16 as black and grey regions.

In the year-2 analysis this method was modified to avoid the sharp bend of the contour (BBC amplitudes around 0.25 in fig. 3.16). This method was compared to two other methods of centrality determination using simple angular cuts with the origin at (1,0), and another method using BBC amplitudes only. All methods are in very good agreement with each other and the difference between them was used to estimate the systematic errors.

In order to relate centrality to the number of participants N_p and the number of binary collisions N_c one can use the Glauber model approach [53]. Each nucleon participating in the RHI collision suffers multiple inelastic interactions with the nucleons of the opposite nucleus. The assumption of the Glauber model is that the cross section, and the direction

---

[4]There is a certain freedom in choosing the normalization factors for the BBC and ZDC amplitudes. The result however does not strongly depend on that choice. Here the normalization is chosen such that the point (1,1) in fig. 3.16 corresponds to the case when $N_{participants} \approx N_{spectators}$.

of the nucleon stay constant during interactions. The inelastic cross section in pp collisions is taken equal to 40 mb from extrapolation done in [54]. The nucleus density profile $\rho(r)$ is given by the Woods-Saxon distribution:

$$\rho(r) = \frac{1}{1 + exp\left(\dfrac{r - r_n}{d}\right)} \tag{3.5}$$

where r_n is the nucleus radius and d is a diffuseness parameter.   Based on the measurements of electron scattering from Au nucleus [55] r_n was taken equal to 6.38 fm and d=0.54 fm.

Using these parameters and the simulated response of the BBC and ZDC one can calculate the number of participants N_p and N_c and relate them to measured centrality using Monte Carlo simulations [5]. The results will be presented in the next chapter.

3.8   Systematic errors

The systematic errors for individual steps of the analysis are summarized here. Statistical errors are generally omitted since they are significantly below per cent level for the highest centrality bin of 0-5% and much smaller than the systematic uncertainties.

Trigger efficiency

Based on simulation it was found that the BBC inclusive trigger represents 92% $\pm$ 2% of the total geometrical cross section at $\sqrt{s_{NN}}$ =130 GeV and 93%$\pm$2% at $\sqrt{s_{NN}}$ =200 GeV. One should add about 1% uncertainty on that value due to contamination in the BBCLL1 trigger data set. The uncertainty in the trigger efficiency imposes an uncertainty on the average particle density determined for a particular centrality bin, which is easy to calculate. The uncertainty decreases with multiplicity. It is only 0.5% for the most central 0-5% and increases to 4.5% for the 30-35% centrality bin.

Acceptance error

The acceptance error represents all multiplicity independent errors. Most of them were previously listed in Table 3.1 (the uncertainties in the number of tracks outside the R acceptance, active areas, and detector intrinsic efficiencies). To these one has to add two small errors, a 0.5% error induced by the vertex restriction and a 1% in the background

---

[5]For this work the author used results of the Glauber model calculations of N_p and N_c made available for use within the PHENIX collaboration.

subtraction derived from different methods of event mixing. All these errors are added in quadrature and result in a total uncertainty of 2.3%.

In-flight decay uncertainty

The systematic error for the in-flight decay correction is discussed in sec. 3.5.3 and 3.5.4. In year-1 the correction was derived based on the Monte Carlo simulation using the PISA code and the HIJING event generator. A systematic error of 4% was assigned to that correction based on the effect of varying the momentum distribution and the particle composition in the simulations and comparison with the results obtained with another data set measured while the east arm was retracted by 44 cm from its nominal position as discussed in sec. 3.6.

   In year-2, the in-flight correction was calculated using results of year-1 studies, which, in particular, allowed to reduce the systematic uncertainty on this correction to 3%. This is discussed in sec. 3.5.4 in great detail.

Errors induced by the double hit resolution

The systematic errors of the analysis are dominated by the uncertainties in the DHR corrections (which as discussed previously affects the track counting and also the background subtraction). This error is multiplicity dependent. The best estimate of these uncertainties comes from the comparison to the results obtained by imposing a 50% larger DHR as shown in fig. 3.14, and the Monte Carlo guidance. The systematic error on the DHR correction for year-1 was estimated to be 3.6% for the highest multiplicity bin and for year-2 it was reduced to 3.2% due to some refinement in the algorithm.

Errors in determination of N_p and N_c

The systematic errors in determination of N_p and N_c are based on the variations of the Glauber model parameters and BBC/ZDC response parameters used in the Monte Carlo simulations. For example the inelastic cross section was varied by ± 3 mb from its nominal value of 40 mb, the r_n was varied in the range of ± 0.25 fm and the diffuseness parameter d in the range of ± 1 fm. Also different assumptions were considered for the shape of the overlapping area of the two nuclei. All errors were added in quadrature and the final results were fitted with the approximations:

$$\frac{dN_p}{N_p} = 2[\%] + 300[\%]/N_p,$$
$$\frac{dN_c}{N_c} = 15[\%] + 400[\%]/N_c \tag{3.6}$$

Chapter 4

Results

This chapter presents the measured charged particle multiplicity density in Au-Au collisions at midrapidity at $\sqrt{s_{NN}}$ =130 GeV and $\sqrt{s_{NN}}$ =200 GeV. Comparison to other experimental results of $dN_{ch}/d\eta$ at AGS, SPS and RHIC energies is given. The charged particle multiplicity is compared to the transverse energy density measured at the same energies. The results are discussed in the framework of several theoretical models.

4.1 $dN_{ch}/d\eta$ at different $\sqrt{s_{NN}}$

The distributions of $dN_{ch}/d\eta$ at mid-rapidity measured at $\sqrt{s_{NN}}$ =130 and 200 GeV are shown in fig. 4.1. The rise at low values corresponds to peripheral events, the middle region
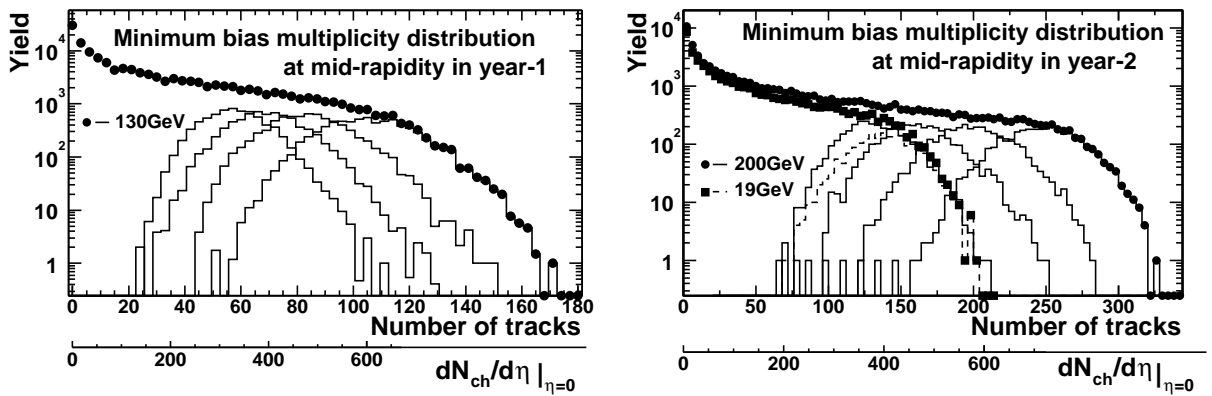
Figure 4.1: Charged particle multiplicity density in Au-Au collisions at mid-rapidity in year-1 at $\sqrt{s_{NN}}$ =130 GeV (left) and in year-2 at $\sqrt{s_{NN}}$ =200 GeV (right).

to increasing overlap between two nuclei (mid-central collisions) and the fall-off to the most central events. The shape of the fall-off is mainly determined by the limited detector acceptance rather than by real fluctuations. The lower axis in the plot corresponds to the

charged particle multiplicity distribution calculated in one unit of pseudorapidity using a geometrical scaling factor of 2.91 for 200 GeV and 5.82 for 130 GeV. The four bell-shape curves in the plot show the distribution of the 20% most central events in steps of 5%.

The energy dependence of the charged particle rapidity density per $0.5N_p$ for central collisions is shown in fig 4.2. The compiled data were measured for different centrality percentiles (the values are indicated in brackets) in the center-of-mass system for RHIC experiments (BRAHMS, PHENIX, PHOBOS and STAR) or laboratory system for all other experiments. In making this plot it was assumed that $dN_{ch}/dy \simeq dN_{ch}/d\eta$ in the lab system and a factor of $\sim$1.2 derived from the HIJING generator is used to account for the $\eta \to y$ transformation in the c.m. system.
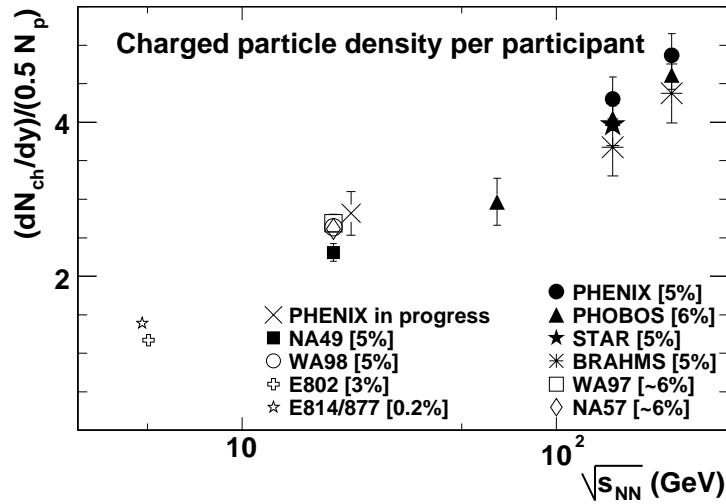
Figure 4.2: dN_{ch}/dy per pair of N_p for central collisions. Data are taken from: PHENIX [32, 2] and this work, PHOBOS [57, 58], STAR [51], BRAHMS [59, 60], NA49 [61], WA98 [10], WA97/NA57 [62], E814/E887 [9], and E802 [63]. The centrality is indicated in brackets.

As mentioned above the PHENIX results are in good agreement with other RHIC measurements. Comparing the PHENIX results to SPS measurement done by NA49 [61] shows that the particle production per participant increases by $\sim$80% at $\sqrt{s_{NN}}$ =130 GeV and by $\sim$110% at $\sqrt{s_{NN}}$ =200 GeV.

From the measured data one can see that the energy dependence of the charged particle multiplicity is not strong. An increase in the energy of the colliding particles by more than one order of magnitude from the SPS energy of $\sqrt{s_{NN}}$ =17 GeV to the full RHIC energy of $\sqrt{s_{NN}}$ =200 GeV causes an increase in the particle production by approximately a factor of 2. The data points presented in fig. 4.2 suggest that $dN_{ch}/dy/(0.5N_p) \propto ln(\sqrt{s_{NN}})$ over a broad range of energies from AGS up to RHIC energies.

4.2 Centrality dependence of $dN_{ch}/d\eta$

In order to study the particle production mechanisms and compare the results of the different experiments it is convenient to scale the charged particle multiplicity with the number of participant pairs ($0.5N_p$). The number of participants is related to the centrality of the collision via a Glauber model [53] as discussed in sec. 3.7. One expects that for the most peripheral collisions the charged particle density per pair of participants would be the same as in $p\bar{p}$ collisions [64]. On the other side, for the central collisions an increase of the reduced charged particle density may indicate new particle production mechanisms related to collective effects.

The charged particle pseudorapidity density per pair of participants is shown in fig. 4.3 vs N_p. for the two different energies $\sqrt{s_{NN}}$ =130 GeV and 200 GeV. The results with
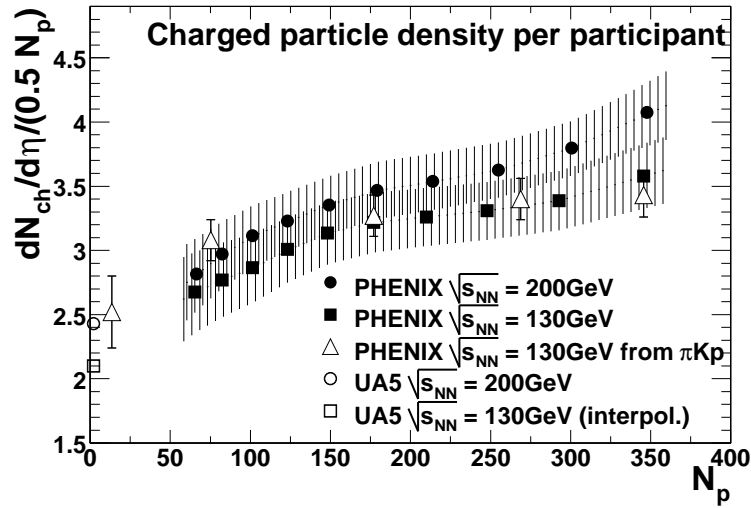
Figure 4.3: $dN_{ch}/d\eta$ per pair of N_p vs N_p measured at $\sqrt{s_{NN}}$ =130 GeV (squares) and 200 GeV (circles). UA5 data for $p\bar{p}$ ($N_p = 2$) is given for comparison. The open triangles represent $dN_{ch}/d\eta$ calculated from measured dN_{ch}/dy of identified particles [56]. The band represents the systematic errors.

systematic errors are tabulated in Table 4.1[1].

One can see that the extrapolation to $N_p = 2$ of the measured $dN_{ch}/d\eta$ points is in agreement with the UA5 results for the $p\bar{p}$ data as expected for both measured energies. The data points also agree to the $dN_{ch}/d\eta$ deduced from the dN_{ch}/dy of identified particles (triangles) measured by PHENIX [46, 56]. The scaled charged particle density $dN_{ch}/d\eta/(0.5 \times N_p)$ grows with N_p and the rise is steeper at $\sqrt{s_{NN}}$ =200 GeV than at

---

[1]The numbers for $\langle N_p \rangle$ at $\sqrt{s_{NN}}$ =130 GeV are slightly different from those published in [32] due to a change in the Glauber model parameters.

Table 4.1: Measured values for $dN_{ch}/d\eta$ and calculation of $\langle N_p \rangle$ at $\sqrt{s_{NN}}$ =200 GeV and 130 GeV together with their ratios. Only systematic errors are shown. Statistical errors for $dN_{ch}/d\eta$ are ± 2 and ± 1 respectively. Statistical errors of ratios are within 0.01

| Cent. | 200 GeV | | | 130 GeV | | | Ratio |
Class	$dN_{ch}/d\eta$	$\langle N_p \rangle$	$\langle N_c \rangle$	$dN_{ch}/d\eta$	$\langle N_p \rangle$	$\langle N_c \rangle$	$R(200/130)$
0-5	709±41	347 ± 10	1059±163	622±41	348±10	1009 ± 146	1.14±0.03
5-10	575±33	293 ± 9	830 ±129	498±31	294±9	794 ± 116	1.15±0.03
10-15	466±26	248 ± 8	656 ±101	413±25	250±8	633 ± 93	1.13±0.03
15-20	382±21	211 ± 7	522 ± 82	344±21	211±7	502 ± 75	1.11±0.03
20-25	313±18	177 ± 7	408 ± 65	287±18	179±7	399 ± 61	1.09±0.03
25-30	252±16	146 ± 6	311 ± 51	235±16	150±6	312 ± 47	1.07±0.03
30-35	201±14	122 ± 5	241 ± 40	188±14	125±5	242 ± 38	1.07±0.03
35-40	160±12	99 ± 5	179 ± 31	147±12	103±5	184 ± 30	1.09±0.03
40-45	125±11	82 ± 5	137 ± 25	115±11	83±5	137 ± 24	1.09±0.04
45-50	96±9	68 ± 4	105 ± 20	89±9	66±4	100 ± 19	1.09±0.04

$\sqrt{s_{NN}}$ =130 GeV resulting in the increase of the ratio R(200/130) vs. N_p shown in fig. 4.4.
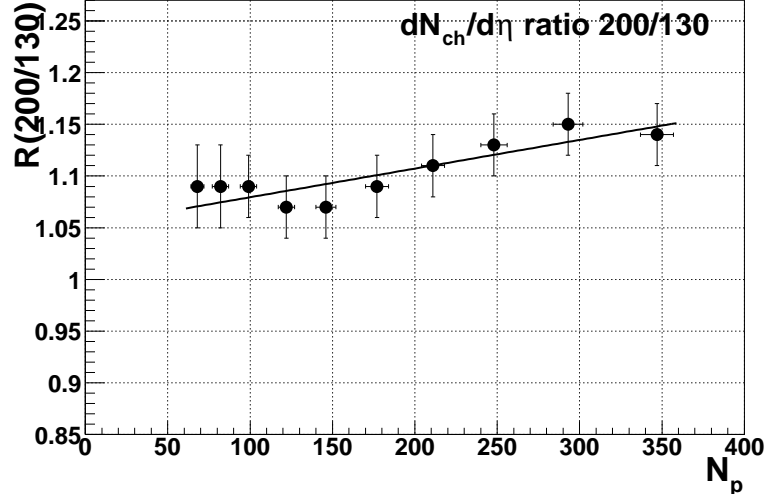
Figure 4.4: Ratio of the number of $dN_{ch}/d\eta$ (raw data) measured at 200 GeV and 130 GeV.

Figure 4.4 shows the ratio of the measured number of tracks, equivalent to $dN_{ch}/d\eta$ assuming that the in-flight correction in year-1 and year-2 are the same, and the calculated number of participants at the two RHIC energies. The abscissa corresponds to the number of participants at $\sqrt{s_{NN}}$ =200 GeV. The systematic errors assigned to the ratios are smaller than for the absolute values because many systematic errors cancel out. The errors result from the uncertainties in the assignment of the centrality classes and the uncertainty in the total geometrical cross section fraction detected by the trigger. The ratio of the

number of tracks shows an increase from the lowest presented class (45%-50%) of $9 \pm 4\%$ to the top class (0%-5%) of $14 \pm 3\%$. This increas within the systematic errors is consistent with a simple scaling of the data.

4.3 Comparison to other experiments

The comparison to the results of other RHIC experiments measuring charged particle multiplicity at $\sqrt{s_{NN}} = 130$ GeV and 200 GeV is shown in fig. 4.5. One can see a very

Figure 4.5: $dN_{ch}/d\eta$ measured by four RHIC experiments at $\sqrt{s_{NN}} = 130$ GeV (right) and 200 GeV (left). Data is taken from: [58] PHOBOS, [59, 60] BRAHMS and [51] STAR. The band represents the systematic errors of PHENIX.
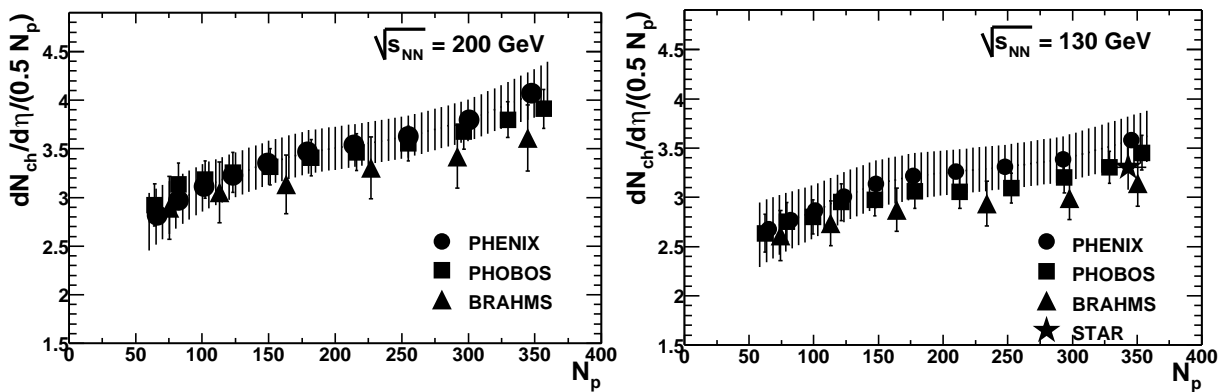
good agreement of all four measurements performed by RHIC experiments. It is important to note that the tools and methods to measure the multiplicity are very different. For example, the PHOBOS experiment uses an array of silicon detectors located very close to the event vertex, the STAR experiment performs full particle tracking in a TPC with magnetic field, and the BRAHMS experiment uses an array of silicon detectors and scintillators. Since the systematic errors of the various measurements have independent origins the weighted average of the measurements would have higher accuracy. Thus, the RHIC average for the most central 5% multiplicity[2] can be estimated to 580 ± 18 at $\sqrt{s_{NN}} = 130$ GeV using data published in [32, 58, 59, 51] and 670 ± 21 at $\sqrt{s_{NN}} = 200$ GeV using references [58, 60] and this work. Both averages are within the systematic errors of the values measured by PHENIX.

The $14 \pm 4\%$ increase of the R(200/130) ratio at the highest centrality bin is in agreement with the increase of $14 \pm 1(stat) \pm 1(syst)\%$[3] in the measurement of

---

[2]Since PHOBOS did not publish the top 5% point, the top 6% point is used. It makes the average slightly smaller than the true value.

[3]Systematic error is estimated from the plot in fig. 1 of reference [58].

PHOBOS [58] and BRAHMS [60] (13%). The PHOBOS experiment observes a flat scaling of $14 \pm 1(stat) \pm 5(syst)\%$ for all centrality classes with $N_p > 100$, whereas our analysis shows a slight increase in R(200/130) as a function of N_p in the same region. However taking into account the systematic errors of both measurements it is not possible to state that two results are in contradiction.

Figure 4.6 shows a comparison of the PHENIX data measured at $\sqrt{s_{NN}} =200$ GeV to the SPS data measured by WA98 experiment [10] at $\sqrt{s_{NN}} =17$ GeV. One can see
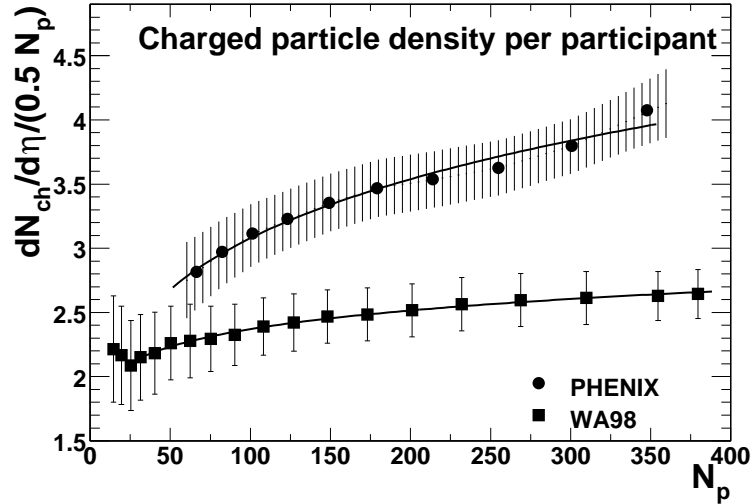
Figure 4.6: $dN_{ch}/d\eta$ measured by PHENIX (circles) at $\sqrt{s_{NN}} =200$ GeV (left) and WA98 (squares) at $\sqrt{s_{NN}} =17$ GeV. The fit is $dN_{ch}/d\eta \propto N_p^\alpha$.

that the PHENIX data shows a much steeper rise of $dN_{ch}/d\eta$ with N_p compared to WA98 measurements. At SPS, several experiments used the parameterization $dN_{ch}/d\eta \propto N_p^\alpha$ to characterize the charged particle multiplicity behavior with centrality. The value of $\alpha = 1.0$ corresponds to proportionality of the charged particle multiplicity with the number of participants. The values of α measured by different experiments are summarized in Table 4.2.

Table 4.2 shows that the parameter α grows with $\sqrt{s_{NN}}$. If at SPS energies it is close to unity within systematic errors, at RHIC, already at $\sqrt{s_{NN}} =130$ GeV it is significantly greater than unity and at full RHIC energy of $\sqrt{s_{NN}} =200$ GeV it is different form unity by more than 3 standard deviations.

4.4   Comparison to $dE_T/d\eta$

Another interesting result derives from the comparison of the multiplicity results $dN_{ch}/d\eta$ to the results of the transverse energy $dE_T/d\eta$ at midrapidity as a function of the number

Table 4.2: Values for parameter α measured in different experiments.

Experiment	Parameter	$\sqrt{s_{NN}}$	Value	Reference
WA97/NA57	$dN_{ch}/d\eta$	17 GeV	1.05 ± 0.05	[10]
WA98	$dN_{ch}/d\eta$	17 GeV	1.07 ± 0.04	[62]
WA98	$dE_T/d\eta$	17 GeV	1.08 ± 0.06	[10]
PHENIX	$dN_{ch}/d\eta$	130 GeV	1.16 ± 0.04	[32]
PHENIX	$dE_T/d\eta$	130 GeV	1.13 ± 0.05	[12]
PHOBOS	$dN_{ch}/d\eta$	130 GeV	1.13	fit to data in [58]
BRAHMS	$dN_{ch}/d\eta$	130 GeV	1.11	fit to data in [59]
PHENIX	$dN_{ch}/d\eta$	200 GeV	1.20 ± 0.05	this work
PHENIX	$dE_T/d\eta$	200 GeV	1.18 ± 0.05	[65]
PHOBOS	$dN_{ch}/d\eta$	200 GeV	1.14	fit to data in [57]
BRAHMS	$dN_{ch}/d\eta$	200 GeV	1.14	fit to data in [60]

of participants measured by PHENIX [12, 33, 65]. Figure 4.7 shows both measurements done by PHENIX at $\sqrt{s_{NN}}$ =130 GeV and 200 GeV plotted side by side.
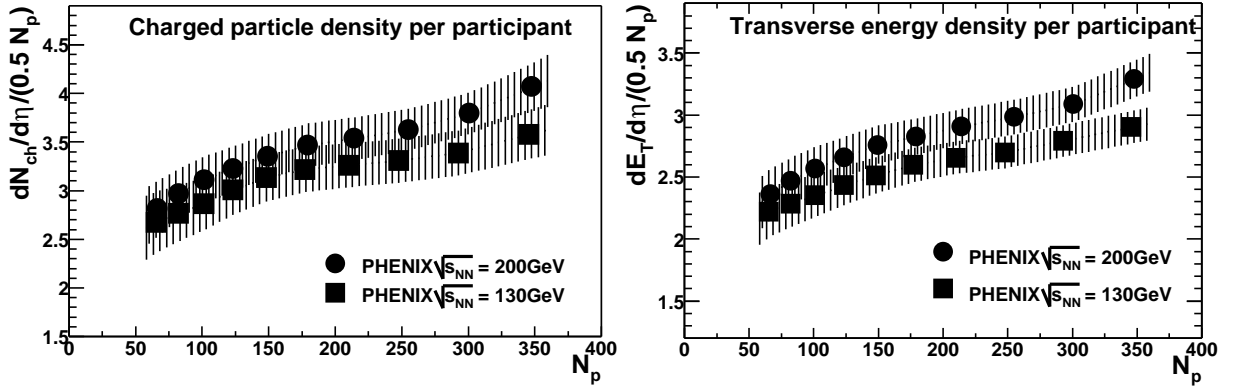
Figure 4.7: Charged particle density (left) and transverse energy (right) density measured by PHENIX at $\sqrt{s_{NN}}$ =130 GeV and 200 GeV.

The energy density ε_{Bj} was determined using the well known Bjorken's formula A.8. For the 2% most central events ε was calculated to be ε_{Bj}=5 GeV/fm^3 at $\sqrt{s_{NN}}$ =130 GeV and ε_{Bj} = 5.7 GeV/fm^3 at full RHIC energy $\sqrt{s_{NN}}$ =200 GeV. These values are significantly above the energy density required for the phase transition as discussed in sec. 1.1 and suggest that at RHIC energies the system has enough energy to form the QGP state.

The figure shows that the two measured quantities exhibit a very consistent behavior. One can also plot the ratio of $\langle E_T \rangle / \langle N_{ch} \rangle$ (and $\langle E_T / N_{ch} \rangle$ for the year-2), the average

transverse energy per charged particle as a function of N_p. This plot is shown in fig. 4.8.

Figure 4.8: $\langle E_T \rangle / \langle N_{ch} \rangle$ as a function of N_p measured by PHENIX at RHIC and WA98 at SPS. The WA98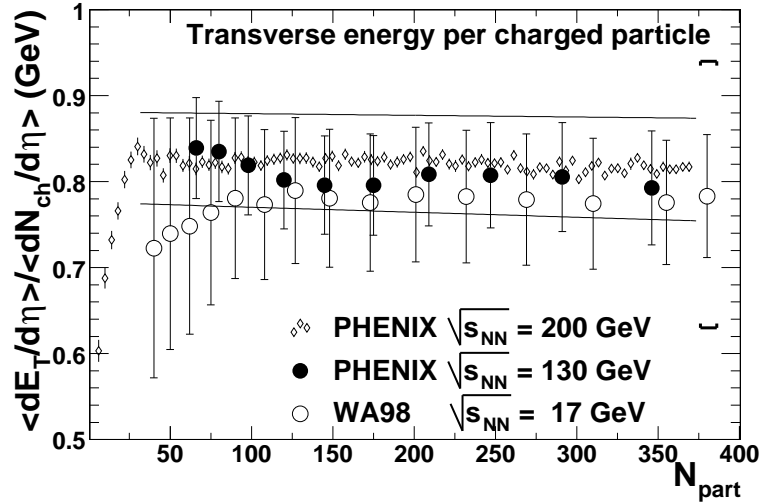 measurements shown with open circles have additional systematic error shown by two lines at the highest bin. PHENIX systematic errors in year-2 are indicated with two solid lines.

From the figure one can see that ratio of $\langle E_T \rangle / \langle N_{ch} \rangle$ measured in year-1 (closed circles) is independent of the number of participants within the systematic errors (8%-9%). For year-2 the analysis was done on an event-by-event base which allowed to measure $\langle E_T / N_{ch} \rangle$ [4] (fine bins). Within the errors of the measurements the $\langle E_T / N_{ch} \rangle$ ratio is independent of centrality, and is equal to 0.8 GeV, as it was also observed by WA98 (open circles) at SPS. For $N_p < 30$ the ratio $\langle E_T / N_{ch} \rangle$ drops, consistently with the drop of the average transverse momentum $\langle p_T \rangle$ of the particles reported in [46].

Moreover, the ratio stays also constant as a function of $\sqrt{s_{NN}}$ from AGS to SPS energies and up to full RHIC energy as can be seen from fig. 4.9. This is a surprising result, because the system obviously behaves differently both with the number of participants (from 30 to 300) and with $\sqrt{s_{NN}}$ (from 4 GeV to 200 GeV) as can be seen in figs. 4.3 and 4.2, and also the transverse momentum and particle composition change. The additional energy deposited in the system by increasing the energy or the number of participating nucleons reflects itself in an increase of the particle production rather than in an increase of the energy of produced particles.

The value of $\langle E_T / N_{ch} \rangle$, referred to as "Global Barometric Observable" in [66] is still waiting for an explanation.

---

[4] $\langle E_T / N_{ch} \rangle$ and $\langle E_T \rangle / \langle N_{ch} \rangle$ give the same results for the year-2 data
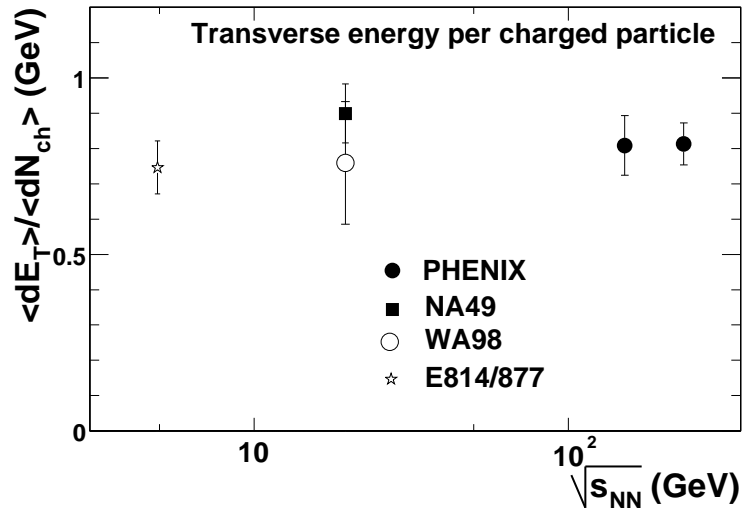
Figure 4.9: $\langle E_T \rangle / \langle N_{ch} \rangle$ as a function of $\sqrt{s_{NN}}$ N_p measured at AGS SPS and RHIC energies. Data are taken from: PHENIX [32, 12, 65] and this work, NA49 [61, 11], WA98 [10], E814/E887 [9, 8].

4.5 Comparison to model predictions

As mentioned in the introduction in sec. 1.7 the $dN_{ch}/d\eta$ is a powerful tool to constrain theoretical predictions. Figure 4.10 shows the comparison of the average RHIC result (vertical bars) with several models taken from a review of theoretical model predictions [67]. The figure shows that only several models, like HIJING, EKRT, UrQMD correctly predict the charged particle multiplicity.

In this thesis the discussion is limited to three models, HIJING [13], the EKRT [14] saturation model, and the new model worked out by Kharzeev, Levin and Nardi (KLN) [15, 16]. These three models are selected from the broad variety of models reviewed in [7] because they consider different mechanisms of particle production. The assumption made in the EKRT model is that the density of the produced gluons saturates at RHIC energy leading to an almost flat behavior of $dN_{ch}/d\eta/(0.5N_p))$ above $N_p > 50$. HIJING assumes that there is a component of particle production from "soft" interactions that scales linearly with N_p and a second component from "hard" processes (pQCD jets) that scales with the number of binary collisions N_c.

$$\frac{dN_{ch}}{d\eta} = A \times \langle N_p \rangle + B \times \langle N_c \rangle \tag{4.1}$$

According to HIJING, the increase in the particle production is due to "hard" processes.

The KLN model also assumes saturation of the gluon density above $N_p = 150$ and "soft" vs "hard" mechanisms. A similar parameterization is also used in KLN model [15]
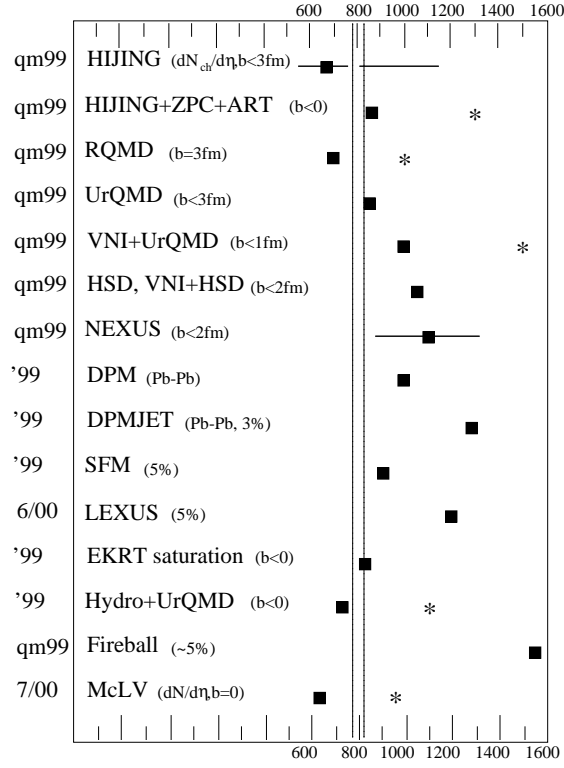
Figure 4.10: Comparison of several theoretical models to the RHIC average 5% most central dN/dy at $\sqrt{s_{NN}}$ =200GeV. Conversion factor 1.2 is used for $\eta \to y$ transformation and factor 2/3 to scale N_{tot} to N_{ch}. More details can be found in [67] where the figure is taken from.

in a slightly different form:

$$\frac{dN_{ch}}{d\eta} = (1 - X(s))n_{pp}\frac{\langle N_p \rangle}{2} + X(s)n_{pp}\langle N_c \rangle \tag{4.2}$$

where n_{pp} is the number of the proton-proton collisions and is described by the function $n_{pp} = 2.5 - 0.25 ln(s) + 0.023 ln^2(s)$. The relation between A, B, and $X(s)$ are obvious. Both models predict that the contribution of "hard" processes grows with initial energy.

Figure 4.11 compares the measured $dN_{ch}/d\eta$ with these theoretical predictions. One can see that the increase of the $dN_{ch}/d\eta$ with N_p is in contrast to the prediction of the EKRT model at both measured energies. The HIJING model, shows qualitative agreement with the data as $\sqrt{s_{NN}}$ =130 GeV and agrees even better at $\sqrt{s_{NN}}$ =200 GeV. One can fit the data points shown in fig. 4.11 with parameterizations 4.1 and 4.2. The results of the fits are shown in Table 4.3.

From the Table 4.3 one can see that all measured parameters agree within systematic errors (where they are shown). The contribution of "hard" processes as measured by PHENIX can be estimated to increase from ∼30% for (45%-50%) centrality class to
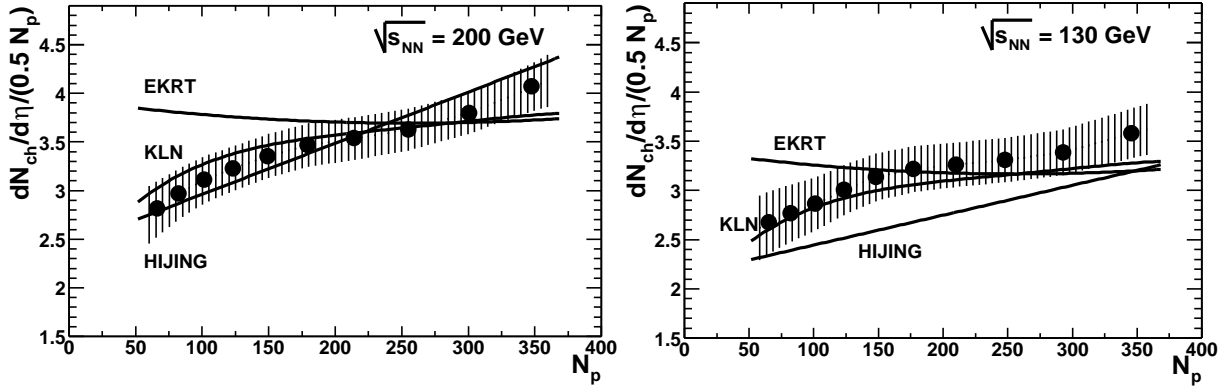
Figure 4.11: $dN_{ch}/d\eta$ vs. N_p compared to different model predictions. HIJING [13], EKRT [14] and KLN [15].

$\sim$50% for (0%-5%) centrality class at $\sqrt{s_{NN}}$ =130 GeV. For the 200 GeV data the same contribution grows from $\sim$40% to $\sim$60% for the same centrality classes.

Table 4.3: Values for parameter A, B and $X(s)$ measured in different experiments and predicted by models. Fitted values of X and recalculated values of A and B are given without systematic errors.

Experiment	$\sqrt{s_{NN}}$	Values			Reference
or Model	GeV	**A**	**B**	**X(s)**	
PHENIX	130	0.88 ± 0.28	0.34 ∓ 0.12	0.11	[32]
PHOBOS	130	1.02	0.20	0.09 ± 0.02	[58]
BRAHMS	130	0.97 ± 0.08	0.22 ∓ 0.04	0.12	[60]
HIJING	130	0.75	0.27	0.07	[13]
KLN	130	1.02	0.20	0.09 ± 0.03	[15]
PHENIX	200	0.86 ± 0.25	0.37 ∓ 0.09	0.12 ± 0.03	this work
PHOBOS	200	1.08	0.27	0.11 ± 0.02	[58]
BRAHMS	200	1.12 ± 0.09	0.24 ∓ 0.04	0.09	[60]
HIJING	200	0.67	0.46	0.12	[13]
KLN	200	1.06	0.29	0.12 ± 0.02	[15]

The particle production in the HIJING model can be increased if the jet quenching mechanism is considered. In this model a pQCD jet propagates in the dense nuclear matter and radiates secondary particles. The particle production depends on the average dE/dx losses.

As one can see from fig. 4.12 the 130 GeV point measured by PHOBOS could not distinguish between these two scenario. The new average measurement of RHIC at $\sqrt{s_{NN}}$ =200 GeV clearly shows that the jet quenching with default parameters does not
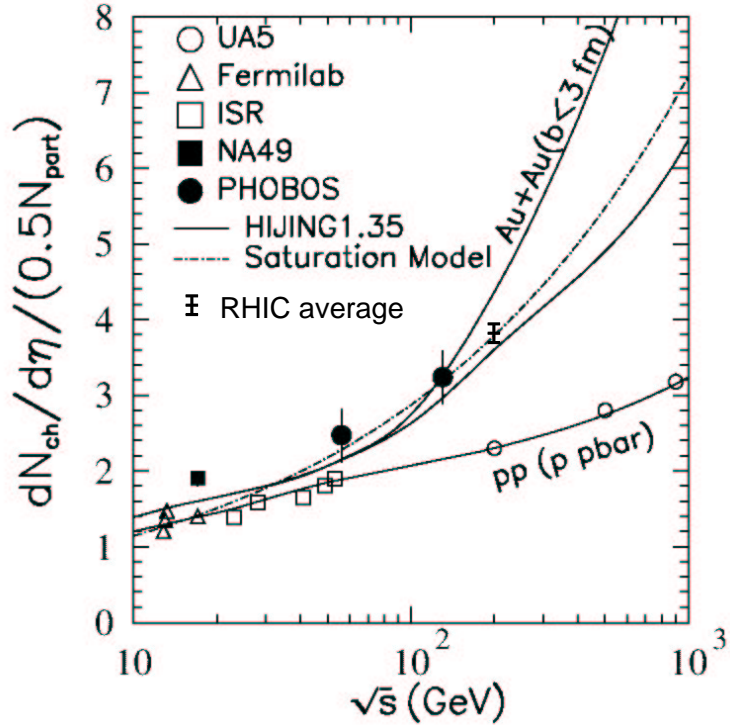
Figure 4.12: Pseudorapidity density per pair of participant calculated by HIJING model with (upper solid curve) and without (lower solid curve) jet quenching mechanism using default parameters. The figure is taken from [13].

reproduce the data. As mentioned above, without jet quenching the HIJING agrees with the measured data.

The KLN model gives an accurate prediction for the parameter $X(s)$ and describes the shape of the curves shown in fig. 4.11 very well, including the bend point at around $N_p \approx 150$. This bend seen in the data, could however, be insignificant due to the systematics of the measurements. In order to make a more accurate comparison one can derive a "RHIC average" measurement of the multiplicity dependence using data shown in fig. 4.5 and measurement of $dE_T/d\eta$ shown in fig. 4.7 scaled with a factor 1./0.8. (This is well justified since for $N_p > 30$ the shapes of the $dN_{ch}/d\eta$ and $dE_T/d\eta$ distributions are the same as demonstrated in fig. 4.8). The "RHIC average multiplicity" per participant is shown in fig 4.13.

The Y-axis labels are removed, because the calculations performed to derive the average curve do not allow to quote the absolute values. The reason is that the scaling of $\langle E_T/N_{ch}\rangle$ used to incorporate the $dE_T/d\eta$ data is not itself an independent measurement. This is not important here because the aim of this comparison is to derive the shape of the centrality dependence curve with smaller systematic errors.

One can see that the KLN model describes the shape of the "RHIC average"
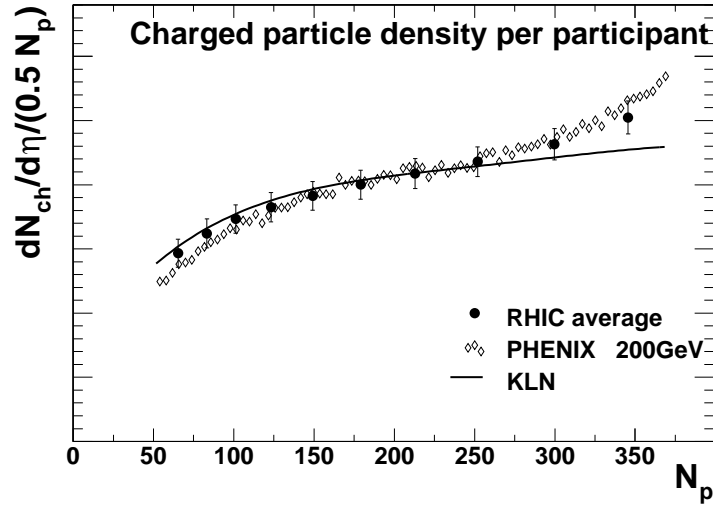
Figure 4.13: Weighted average $dN_{ch}/d\eta$ points measured by RHIC (circles) together with PHENIX data (dots), and prediction of the KLN model (line). The Y-axis labels are removed, see text. All curves are normalized at N_p=200.

multiplicity including the bend around $N_p \approx 150$ which appears more pronounced with smaller systematic errors. At the same time in the range $N_p > 250$ the KLN model starts to deviate from the data. The deviation increases with N_p and, if one follows the trend of the PHENIX points, which are everywhere consistent with the average values, this deviation may increase even more. This might be an indication that there is another mechanism of particle production at the highest multiplicities which is not considered in the framework of the KLN model.

Chapter 5

Summary

The thesis has two distinct parts corresponding to two major goals of this work. The first includes the design, construction, installation, operation and performance of the PC1 subsystem of the PHENIX detector and the second part is primarily based on the detector described in the first part. The second part is devoted to the measurement of charged particle multiplicity in Au-Au collisions at RHIC energies. The two parts are closely related because the analysis of $dN_{ch}/d\eta$ described in the second part primarily uses detector described in the first.

The PC1 detectors based on novel principle of MWPC readout were build according to all specification and requirements imposed by the PHENIX experiment. The most challenging among them were a total radiation thickness of 1.25% of a radiation length and minimum amount of inactive area in the detector (0.7%). The PC1 subsystem is a crucial part of the PHENIX detector tracking system, which provides the angular information for the track. The project was completed ahead of schedule which allowed to start the first PHENIX run with both central arms operational, while only one arm was originally planned to be used in the year 2000 physics run. After 2 years of work the PC1 showed no degradation in its performance and is considered one of the most robust subsystems of the PHENIX detector.

The charged particle multiplicity analysis accomplished using the PC detectors lead to the first PHENIX physics publication [32]. It was the first measurement of the centrality dependence of $dN_{ch}/d\eta$ in Au-Au collisions at $\sqrt{s_{NN}}$ =130 GeV. The Global variables such as $dN_{ch}/d\eta$ and $dE_T/d\eta$ provide crucial information about the mechanism of particle production. Our results helped to constrain or to adjust the assumptions of theoretical models aiming at describing Au-Au collisions at the unprecedented high energies achieved at RHIC.

Using results discussed in the last chapter of this thesis it was shown that the Bjorken

energy density $\varepsilon_{Bj} \approx 5$ GeV/fm at RHIC is above what is required for the formation of the QGP. It was shown that with increasing centrality the number of particles produced in the collisions grows faster than the number of participating nucleons, which was the first evidence of the importance of hard scattering at RHIC energies. This was later confirmed by other measurements performed at RHIC.

It was pointed out that in the RHI collisions at high energy the average transverse energy per charged particle is practically independent of centrality and initial energy of the colliding nuclei. This puzzling result is still awaiting its theoretical explanation.

Appendix A

Definitions of used variables

A.1 Collision geometry and centrality

A schematic drawing of the heavy ion collision at high energy is shown in fig. A.1. The
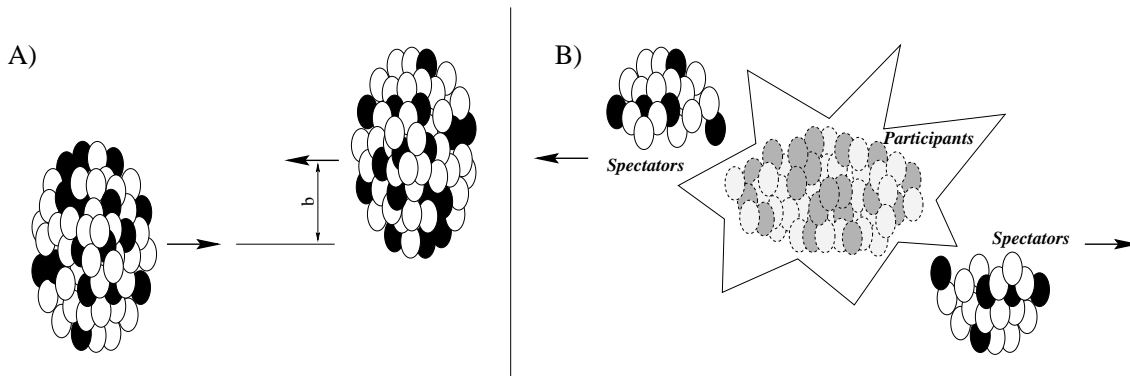

Figure A.1: Collision between two heavy nuclei before (A) and after (B) collision in the center of mass system. See text for explanation.

nucleons of both nuclei fall into two categories. Nucleons participating in the collision inside the overlapping area are called *participants* (N_p) and nucleons continuing to move after the collision relatively undisturbed along the incident direction are called *spectators*. The *Number of binary collisions* (N_c) is the number of collisions between the participants during the collision.

Both N_p and N_c depend on the *impact parameter* of the interaction b defined as the transverse distance between the centers of the two colliding nuclei (see fig. A.1). None of those quantities can be measured in the experiment, however they can be deduced using the Glauber model [53] (see sec. 3.7).

In order to relate the Glauber model calculations to the experimentally measured values one introduces a definition of *centrality*, measured in per cents. Zero per cent

centrality corresponds to the most central events with $b = 0$ (maximal number of N_p). 100% centrality corresponds to the most peripheral event, where at least one nucleon-nucleon collision ($N_p = 2$) tales place between two nuclei .

A.2   Kinematic variables

A basic quantity which characterizes is the initial energy in the c.m.s. $\sqrt{s}$ defined as:

$$\sqrt{s} = \sqrt{m_1^2 + 2E_1 E_2 - 2(\overline{p}_1 \cdot \overline{p}_2) + m_2^2} \tag{A.1}$$

where the mass m and the energy E denoted with indices 1 and 2 correspond to two colliding nuclei. Since the interaction between two nuclei does not involve all nucleons in them the relevant measure of the initial energy is $\sqrt{s_{NN}}$, i.e. the center of mass energy per pair of colliding nucleons.

The second part of this thesis (chapters 3 and 4) deals with *charged particle multiplicity* or simply *multiplicity*, the number of charged particles N_{ch} emitted during collision. Usually one measures N_{ch} in some *rapidity* interval (dN_{ch}/dy), where the rapidity y is defined as

$$y = \frac{1}{2} ln\left(\frac{E + p_z}{E - p_z}\right) \tag{A.2}$$

E is the particle energy and p_z is the longitudinal (along the beam) component of the particle momentum p. A frequently used approximation of the rapidity is the *pseudorapidity* η defined by

$$\eta = -ln\left(tan\frac{\theta}{2}\right) \tag{A.3}$$

where θ is the polar emission angle of the particle, the angle between the particle momentum p and the beam axis. Since the measurement of η does not require knowledge of the particle mass (particle identification) the quantity $dN_{ch}/d\eta$ is widely used in this thesis as an approximation to dN_{ch}/dy. With the PHENIX central arm design described in 1.5, the measurements of $dN_{ch}/d\eta$ are done in the central region i.e. at *midrapidity*, covering the pseudorapidity distribution interval $|\eta| < 0.35$. The notation of $dN_{ch}/d\eta|_{\eta=0}$ is reduced to $dN_{ch}/d\eta$ and $dN_{ch}/dy|_{y=0}$ to dN_{ch}/dy unless specifically mentioned otherwise.

The pseudorapidity η and rapidity y are equal to each other for a massless particle, or the pseudorapidity approaches the rapidity when the momentum is much larger than

the particle mass $p \gg m$. An exact relation between η and y is given by:

$$sinh(\eta) = \frac{m_T}{p_T} sinh(y) \tag{A.4}$$

where p_T and m_T are the particle *transverse momentum* and *transverse mass* respectively. The transverse momentum of a particle is the momentum component in the direction perpendicular to the beam

$$p_T^2 = p_x^2 + p_y^2 \tag{A.5}$$

and the transverse mass is defined as:

$$m_T = \sqrt{m^2 + p_T^2} \tag{A.6}$$

A.3 Transverse energy and Bjorken formula

The *transverse energy* of the event E_T is defined as:

$$E_T = \sum_{i=1}^{N} E_i \cdot sin\theta_i \tag{A.7}$$

where index i is running through all hits in the calorimeter. The transverse energy E_T can be measured using a segmented calorimeter.

The PHENIX detector can measure $dE_T/d\eta$ in the midrapidity region $|\eta| < 0.35$. The notation of $dE_T/d\eta|_{\eta=0}$ is reduced to $dE_T/d\eta$ unless specified otherwise.

The transverse energy density dE_T/dy is often related to the initial energy density ε_{Bj} using the Bjorken formula [6]:

$$\varepsilon_{Bj} = \frac{1}{\pi R^2 \tau} \frac{dE_T}{dy} \tag{A.8}$$

where $R = r_o A^{1/3}$ with $r_o = 1.18$ fm is the nuclear radius and τ is the formation time usually taken as 1 fm/c.

Acknowledgments

The years devoted in working towards the Ph.D. degree at the Weizmann Institute of Science in Israel were the most exciting time for me both professionally and privately. This became possible, first of all, because the country of Israel exists on the map of the World and that there is a very special place in it, called the Weizmann Institute, where people can work for Science. I believe that this is one of the wonders of the XX-th century, and I say thanks to G_d and to all those people who have made this wonder a reality.

Personally, first of all, my words of acknowledgment go to my supervisor Prof. Itzhak Tserruya, for his help and understanding. His advice in many critical moments of my work was a key to success. I am very thankful for the support he rendered to me in many different situations. Working in the group of Prof. I.Tserruya for me was the School for learning Science.

I thank Prof. Zeev Fraenkel whose knowledge and experience were a permanent sources of guidance through all the years of my Ph.D.

I thank Dr. Ilia Ravinovich for his significant help, advises and discussions during my work in the group.

I am very thankful to Dr. Boris Khachaturov, for his help, discussions of many different physical issues, and for really friendly relations.

I thank Alexander Cherlin and Alexander Kozlov for their help in working on the hardware and analysis parts of the project. My words of acknowledgment also go to Dr. Wei Xie for his help during the construction of the PC1 detectors.

Besides the Heavy Ion group of Prof. I.Tserruya, where I was working on my project, there are many people at the Weizmann Institute who provided me help, support, and advises to my research.

I would like to thank Prof. Moshe Kugler and Prof. Uri Karshon for their attention to my work and very useful discussions.

I am very thankful to Prof. Amos Breskin and his group for advise and help on different issues concerning particle detectors. My special thank to Prof. A.Breskin for an excellent course on "Radiation Detectors" he delivered at the Weizmann Institute.

I would like to thank Prof. Ehud Duchovny, for a short, but very pleasant time working with him.

My thanks to the designer unit of the Weizmann Institute lead by Benjamin Pasmantirer, and to the designer Lilia Goffer for their work on the Winding Machine and the PC1 projects. And following that I am saying a lot of thanks to the Physics department workshop, lead by Aharon Bar-On and to all people there, especially to Genrih Goaga, whose labor made these projects to materialize.

My thanks to the Electronics group of the Physics department lead by Dr. Lorne Levinson, to Yaron Gal, Moshe Sidi, Alexander Roich, Eitan Golan and especially to Yaffa Gil. I am also thankful to the computer unit of the Physics department, to Camelia Botez and Helen Katz. My special thank to Vladimir Notkin (z"l) for his contribution to the Winding Machine project.

I appreciate the help and permanent support of the Secretary of the Physics Department lead by Yaakov Ben-Shmuel, and to all people working there, Corinne Hasdai, Ana Weksler, Lidia Moskovich, Hazel Fisher, Sharona Levi, and especially to Dalia Kochavy.

I am very thankful to many other people of the Physics Department and the Weizmann Institute who in many different ways helped me during my work towards the Ph.D. degree. Among them, Dr. Vladimir Smakhtin, Dr. Michael Rappaport, Igal Shahar, Meir Shua, Boris Elkonin, Adina Ciobotariu and many many other people.

Outside the Weizmann Institute I wold like to thank Dr. Leonid Barabash, for his consulting in working on the PC1 project.

I would like to express my acknowledgments to all people of the PHENIX collaboration and personally to the Spokesman of the PHENIX experiment Prof. William Zajc and the members of the PHENIX Speaker Bureau who awarded me honor to present the collaboration results at the Quark Matter conference in year 2001 at Stony Brook.

Within the PHENIX collaboration my words of acknowledgments are to the group of the Lund University, Sweden, to Prof. Hans-Ake Gustaffson, Prof. Anders Oskarsson. My special thanks are to Dr. David Silvermyr for his significant contribution and the pleasure of working with him on the PC1 project and multiplicity analysis.

At the Brookhaven National Laboratory I would like to thank Dr. Michael Tannenbaum, Dr. Mike Sivertz, Dr. David Morrisson, William Liccardi and many other people who helped my during my visits to the USA working on my Ph.D. Project.

At the Vanderbilt University, USA, I would like to thank Prof. Senta-Victoria Greene, Prof. Charlie Maguire, Dr. Timothy Miller, Dr. Andrew Roose and Darryl Borland.

At the McGill University, Canada, I am thankful to Prof. S.K.Mark, Dr. Nikolai

Bibliography

[1] F.Karsch, Nucl. Phys. **A698**, (2002) 199-208.

[2] Proceedings of the Quark Matter 2001 Conference. Editors: T.Hallman, D.Kharzeev, J.Mitchell, and T.Ullrich. Elsevier 2002.

[3] J.W.Harris and B.Müller. Ann. Rev. Nucl. Part. Sci. **46** (1996) 71-107 and hep-ph/9602235

[4] I.Tserruya, Heavy Ion Collisions. CERN-PPE/95-185.

[5] P.M.Jacobs, Heavy Ion Physics in the RHIC era. PrHEP hep2001.

[6] J.D.Bjorken, Phys. Rev. **D27**, (1983) 140

[7] S.A.Bass et al., Nucl. Phys. **A661**, (1999) 205c

[8] J.Barrette, et al. Phys. Rev. Lett. **70**, 2996 (1993).

[9] J.Barrette, et al. Phys. Rev. **C51**, 3309 (1995).

[10] M.M.Aggarwal et al., Eur. Phys. J. **C18** (2001) 651

[11] T.Alber, et al. Phys. Rev. Lett. **75**, 3814 (1995).

[12] K.Adcox et al. Phys. Rev. Lett.**87** (2001) 052301

[13] X.N.Wang and M.Gyulassy, Phys. Rev. Lett. **86** 3498 (2001)

[14] K.J.Eskola et al. Nucl. Phys. **B570**, 379 (2000) and Phys Lett **B497** 39 (2001)

[15] D.Kharzeev and E.Levin, Phys. Lett. **B523**, (2001) 79-87 and nucl-th/0108006

[16] D.Kharzeev and M.Nardi, Phys. Lett. **B507** (2001) 121-128 and nucl-th/0012025

[17] P.Bordalo (NA50 Collaboration), Nucl. Phys. **A698** (2002) 127c-134c.

[18] K. Adcox et al., Phys. Rev. Lett. **88** (2002) 022301

[19] H.Appelshäuser (CERES Collaboration), Nucl. Phys. **A698** (2002) 253c-260c.

[20] I.Tserruya, Relativistic Heavy-Ion: Experimental Overview. To be published in ICPAQGP proccedings, Japur 2001.

[21] G.Q.Li, C.M.Ko and G.E.Brown, Phys. Rev. Lett. **75**, 4007 (1995), Nucl. Phys. **A606**, 568 (1996) and G.Q.Li, C.M.Ko, G.E.Brown and H.Sorge, Nucl. Phys. **A611**, 539 (1996).

[22] R.Rapp, G.Chanfray, J.Wambach, Nucl. Phys. **A617** (1997) 472

[23] K.Adcox et al., Phys. Rev. Lett. **88**, (2002), 192303 and nucl-ex/0202002

[24] Z.Fraenkel et al., Phenix technical note number 391, (2001)

[25] The BRAHMS experiment home page http://www4.rcf.bnl.gov/brahms/WWW/

[26] The PHOBOS experiment home page http://www.phobos.bnl.gov/

[27] K.Adcox at. al., The PHENIX detector. To be submitted to Nucl. Inst. & Meth. A

[28] The STAR experiment home page http://www.star.bnl.gov/

[29] The PHENIX experiment home page http://www.phenix.bnl.gov/

[30] K.Ikematsu *et al.*, Nucl. Instr. Meth. **A411** (1998) 238

[31] C.Adler *et al.*, Nucl. Instr. Meth. **A470** (2001) 488-499

[32] K.Adcox et al. Phys. Rev. Lett. **86** (2001) 3500

[33] A.Milov (PHENIX Collaboration), Nucl. Phys. **A698** (2002) 171c-176c.

[34] K.Adcox at. al., Construction and Performance of the PHENIX Pad Chambers. Submitted to **NIM A**.

[35] F.Sauli (editor) Instrumentation in high energy physics. World Scientific, 1992.

[36] G.Agakichev et. al., Nucl. Phys. **A661**, (1999) 673c-676c and CERN-SPSLC 96-50 (1996)

[37] L.Caren at. al., Nucl. Inst. & Meth. A396 (1997) pp.310-319.

[38] A video tape with a manual of the test & soldering procedures is available upon request.

[39] E.Mathieson. Nucl. Inst. & Meth. A270 (1988) p.602-603.

[40] O.Teodorescu. Test of a New Prototype of Multiwire ProportionalChamber with Pixel Pad Cathode Readout. Master degree thesis. McGill University, Canada 1998.

[41] T.Swensson, Tracking Chambers with Two-Dimensional Readout used for Extraction of Particle Production Ratios in High Multiplicity Pb+Pb Collisisons at 158 A GeV. Ph.D. thesis. Lund University, Sweden 1999.

[42] A.Milov, I.Tserruya, W.Xie. Analytic Calculation of the Phenix Pad Chamber Performance. Phenix techical note 379. 2000.

[43] Garfield simulation code http://consult.cern.ch/writeup/garfield/

[44] PHENIX Pad Chamber Group. Gas gain measurements of the PC1 and PC3. PHENIX technical Note 380.

[45] PHENIX Simulation Accessory.
http://www.phenix.bnl.gov/phenix/WWW/simulation/SimulationMirror.html

[46] K.Adcox et al. Phys. Rev. Lett.**88**, 242301 (2002) and nucl-ex/0112006

[47] H. Caines (STAR Collaboration), Nuclear Physics A698 (2002) 112c-117c.

[48] C.Roy nucl-ex/0111017.

[49] C.Adler et al. Phys. Rev. Lett. **87**, 262302 (2001).

[50] B.B.Back et al., Phys. Rev. Lett. **87**, 102301 (2001)

[51] C.Adler et al. Phys. Rev. Lett. **87**, 112303 (2001).

[52] D.Silvermyr, Aspects of Hadron Production in High-Energy Heavy-Ion Collisions. Ph.D. thesis. Lund University, Sweden 2001.

[53] In book of C.-Y.Wong. Introduction to High-Energy Heavy Ion collisions. World Scientific. (1994)

[54] G.J Alner et al., Z Phys. **C32**, 153-161 (1986).

[55] Hofstadter et al., Phys. Rev. **101**, 1131 (1956).

[56] J.M.Burward-Hoy. Transverse Momentum Distribution of Hadrons produced in Au-Au Collisions at 130GeV Measured by the PHENIX Experiment at RHIC BNL. Ph.D. thesis. State University of New York at Stony Brook. USA 2001.

[57] B.B.Back et al., Phys. Rev. Lett. **85**, (2000) 3100

[58] B.B.Back et al., nucl-ex/0201005

[59] I.G.Bearden et al., Phys. Lett. **B523** (2001) 227-233 and nucl-ex/0108016

[60] I.G.Bearden et al., Phys. Rev. Lett. **88**, 202301 (2002) and nucl-ex/0112001

[61] J.Bächler, et al Nucl. Phys. **A661**, 45c (1999).

[62] F.Antinori et al., Nucl. Phys. **A661** (1999), 357c-61c.

[63] L.Ahle, et al. Phys. Rev. **C59**, 2173 (1999).

[64] G.J Alner et al., Z Phys. **C33**, 1 (1986).

[65] A.Bazilevsky, Private communications.

[66] M.Gyulassy, nucl-th/0106072.

[67] K.Eskola, Nucl. Phys. **A698** (2002) 78c-87c.